

Giant directional dichroism in chiral Ni_3TeO_6
in
THz spectroscopy in high magnetic fields

I N A U G U R A L - D I S S E R T A T I O N

zur
Erlangung des Doktorgrades
an der Mathematisch-Naturwissenschaftlichen Fakultät
der Universität zu Köln

vorgelegt von
Malte Langenbach
aus Duisburg

Köln, 2019

Berichterstatter:

Prof. Dr. Markus Grüninger

Prof. Dr. Joachim Hemberger

Vorsitzender der
Prüfungskommission:

Prof. Dr. Simon Trebst

Tag der mündlichen Prüfung:

25.02.2019

Contents

Introduction	1
1 Broadband continuous-wave THz spectrometer	5
1.1 General setup	5
1.2 Design of the magnetic-field setup	7
1.3 THz antennae	9
2 Measuring with circularly polarized light	11
2.1 Measurement principle	11
2.2 Pseudo-transmittance	15
2.3 Discussion	16
3 Group delay	19
3.1 Contribution from optical fibers	19
3.2 Contribution of the photomixers and antennae	21
3.3 Contribution of the terahertz path	22
3.4 Combination of all contributions	23
3.5 Active region	25
3.6 Quasi-time-domain analysis	25
3.7 Group delay and uncertainty of the phase	27
4 Self-normalized phase measurement	31
4.1 Concept of measuring with three THz frequencies	32
4.2 Three lasers and drift correction	33
4.3 Drift correction under extreme conditions	35
4.3.1 Frequency sweep at low temperatures and constant magnetic field	36
4.3.2 Magnetic field sweeps	37
4.4 Discussion	38
5 Chiral matter and non-reciprocal behavior	41
5.1 Transmission through a chiral medium	42
5.1.1 Quadrochromism	43
5.1.2 Discussion	45
5.2 Transmission through chiral matter on normal incidence in presence of a magnetic field	46
5.3 Transmission through chiral matter upon normal incidence	50

6	Material properties of Ni_3TeO_6	53
6.1	Crystal structure	53
6.2	Magnetic structure	55
6.3	Sample	58
7	How to measure very small samples with irregular shape?	61
7.1	Diffraction effects	61
7.2	Discussion	64
8	Measurements on Ni_3TeO_6	67
8.1	Results at 3 K	68
8.1.1	Transmittance and ΔL	68
8.1.2	Rotation of the plane of polarization for linearly polarized light . .	71
8.1.3	Comparison of the results for ΔL and Θ	73
8.1.4	Fits of the data	74
8.1.4.1	Real and imaginary part of the refractive index at 3 K . .	77
8.1.4.2	Modeled thickness dependence of the transmittance at 1058.8 GHz	78
8.1.4.3	Fit result and Θ	79
8.2	Temperature dependence	80
8.2.1	Temperature dependence of ΔL	80
8.2.2	Temperature dependence of Θ	81
8.2.3	Temperature dependence of real and imaginary parts of the refrac- tive index	81
8.2.4	Temperature dependence of fit parameters	83
8.3	Parallel and crossed linear polarizers	84
8.4	Data in magnetic field	86
8.4.1	Single-domain sample	86
8.4.1.1	$\Delta L(\mathbf{H})$ and fit	88
8.4.1.2	Simulation of optical parameters for small magnetic fields at 3 K	90
8.4.2	Multidomain sample	92
8.4.3	Unpolarized light	95
9	Conclusion	97
	Bibliography	99
	List of Figures	107
	List of Tables	117
10	Appendix	119
10.1	Results for fits to ΔL_{LCP} and ΔL_{RCP} for different temperatures	119

11 Publications	123
12 Abstract	125
13 Kurzzusammenfassung	127

Introduction

The Chinese Chang'e 4 mission which launched on December 7, 2018 has the goal to perform the first soft-landing on the far side of the moon. The landing is scheduled for January 2019, 50 years after the Apollo 11 mission landed on the opposite side of the moon. Considering the effort such a mission takes, looking at things from the other side really seems to be worth something.

In general, an effect that is different for opposite directions is called non-reciprocal. The most prominent example is that of an electrical diode where the charge transport is a non-reciprocal effect due to symmetry breaking by an inbuilt electric field. The result is that a current may flow in one direction whereas it is prevented from passing in the other direction. In optics, the term directional anisotropy refers to an effect where such a non-reciprocity holds true for all polarization states of a light beam. Such a directional anisotropy can have different forms for emission, diffraction or, as in our case, absorption [1]. Different absorption for light traveling in opposite directions is called directional dichroism. The general reason why such an effect can be established is founded in symmetry, or more precisely the lack thereof. This is also the reason why multiferroic materials are a good place to look for such effects [2]. A list of symmetry conditions giving rise to non-reciprocal light propagation in magnetic crystals can be found in Ref. [1].

The multiferroic Ni_3TeO_6 is an exceptional compound. The structure is both chiral and polar already at room temperature [3] so the crystal structure breaks inversion symmetry. The antiferromagnetically ordered phase below $T_N = 53\text{ K}$ features collinear spins and a significantly enhanced electric polarization due to magneto-electric coupling [4]. Despite the simple magnetic structure it exhibits non-hysteretic magnetic switching and the record linear magneto-electric coupling constant in single-phase materials [4]. Those findings were made on single crystal plates of $\sim 1\text{ mm} \times 1\text{ mm} \times 0.1\text{ mm}$ [3] and $\sim 1\text{ mm} \times 1\text{ mm} \times 0.4\text{ mm}$ [4], respectively. Despite the large interest in this material in the past years, no measurements in the THz range between 100 GHz and 1000 GHz on single crystals were reported to date, simply due to the lack of single crystals large enough for measurements.

This is a general problem. New materials which are expected to exhibit exciting physical properties are often initially available as very small crystals. Crystal growth is a time consuming process that often needs various attempts to improve a procedure which results in large single crystals. Exemplary methods like resistivity or magnetization measurements, infrared spectroscopy as well as dielectric spectroscopy in the gigahertz range can be performed on samples of the size of a millimeter or less. However, diffraction plays an important role in optics. When the wavelength is of the order of the sample size, the light used for the investigation will be diffracted. In terahertz spectroscopy the wavelengths are comparably large (1 mm at 300 GHz). Single crystals of the size of several millimeters are usually needed. Additionally the shape of the crystal plays an important role since preferably circular apertures are used what reduces the investigated area of a bar-like sample drastically. The investigation of a certain material in the THz

range starts relatively late compared to investigations in other frequency ranges where smaller samples can be measured. In our continuous wave (cw) terahertz spectrometer, we measure amplitude and phase information simultaneous. The strong influence by diffraction on the measured terahertz amplitude for small samples makes a detailed analysis impossible, whereas the phase data is almost unaffected. This gives the possibility for a quantitative analysis based on the phase data, which can be supported by investigating relative changes in the transmittance. In this thesis, measurements on a Ni_3TeO_6 sample with a surface area less than 1 mm^2 with a rather inconvenient shape due to the arrangement of domains in the crystal will be presented. We use circularly polarized light to investigate natural circular dichroism, i.e. a difference in the refractive index for the two opposite polarizations in zero magnetic field. Additionally, we will present non-reciprocal effects such as directional dichroism in an external magnetic field.

In the first part of this thesis, our setup is introduced, see Ch. 1. More details are presented on the magnetic field setup which provides an unconventional but relatively simple way of performing magnetic field dependent measurements. Furthermore, the photomixers are described due to their importance in relation to the absolute intensity, the frequency dependence of the measured phase, and the polarization of the terahertz radiation. The latter is the topic of, Ch. 2. Here, the circular polarization of the terahertz radiation, as well as the polarization sensitivity of the receiver to a specific circular polarization, is investigated. A method based on the polarization dependence of the receiver enables to differentiate between the two opposite polarizations.

In Ch. 3, an overview of important parameters affecting the measured THz phase is given. The influence on those parameters to the uncertainty of the phase is investigated, the main sources of errors are named, and the size of their contribution to the total error is estimated. The main contribution is caused by thermal drifts. The size of those drifts is investigated in Ch. 4, including the presentation of a method using a stable terahertz phase of a fixed terahertz frequency as reference to correct for the induced errors. The efficiency of this method is demonstrated under close-to-ideal measurement conditions as well as under extreme conditions for example for measurements in the magnetic field setup directly at low temperature and in high magnetic fields.

In Ch. 5, a discussion on chiral matter and non-reciprocal behavior is given. A general description of dichroism and quadrochroism in chiral matter based on symmetry arguments is followed by a mathematical description of the phenomena in the case of Ni_3TeO_6 .

Chapter 6 gives an overview on the material properties of Ni_3TeO_6 based on literature. First, the crystal structure is presented, followed by the magnetic structure. The results of recent optic spectroscopy measurements are discussed and measurements on polycrystalline sample in the terahertz range are shown to mark the state of the research in this range. A short overview concerning the sample used for measurements during this thesis is followed by a description about dealing with problems when measuring small samples in the terahertz range, see Ch. 7.

In the last part, Ch. 8, the results for different measurements are presented. Investigations with circularly polarized light in the antiferromagnetic phase show low temperature modes with a significant difference in the refractive index measured with the two helic-

ities. This difference in the refractive indice leads to a significant rotation of the plane of polarization for incoming linear polarization upon passing through the sample, what can be investigated looking at relative changes in the transmittance. Magnetic field dependent measurements are presented for different fields up to 8 T.

1 Broadband continuous-wave THz spectrometer

In the terahertz (THz) regime, there are two different spectroscopic methods, addressing the linear response namely THz time-domain spectroscopy and THz frequency-domain spectroscopy. A variety of sources and detectors in this range as for example backward-wave oscillators, quantum-cascade lasers or free-electron lasers, black-body radiation for creating THz radiation and bolometers, Golay cells or pyroelectric detectors can be used. In THz time-domain spectroscopy, the time-dependent amplitude variation is recorded and converted into a spectrum via Fourier transformation. In THz frequency-domain spectroscopy, the amplitude and phase information is obtained for each frequency point. In our case, frequency domain spectroscopy based on the photo mixing of NIR lasers, offers a higher resolution which is only limited by the stability and width of the lasers and can reach 1 MHz [5]. For time-domain spectroscopy, the achievable spectral resolution depends on the dynamic range and is for a typical spectroscopy system ≈ 0.8 GHz at 500 GHz [6]. On the other hand the time-domain measurement offers a relatively high bandwidth up to 14.5 THz [7] whereas a laser based frequency domain spectra is limited by the mode-free tuning-range of the lasers which is 2.75 THz [8] up to date.

1.1 General setup

The continuous-wave (cw) THz spectrometer employed in this thesis is a setup with components of the company Toptica. A sketch including the main components of the cw THz spectrometer is shown in Fig. 1.1. It is an all fiber based setup with only a small THz path in air. Responsible for creating the THz frequency are the two distributed feedback (DFB) lasers [9]. The DFB lasers have a central wavelength of 780 nm. The difference frequency, which determines the THz frequency, is tunable from 0 THz to 1.8 THz. The frequency stability of the DFB lasers, which is essential for the stability of the THz frequency, lies in the MHz regime [5]. The signal of the two lasers is superimposed in a fiber array and amplified by a tapered amplifier [10]. This amplification can be adjusted to meet

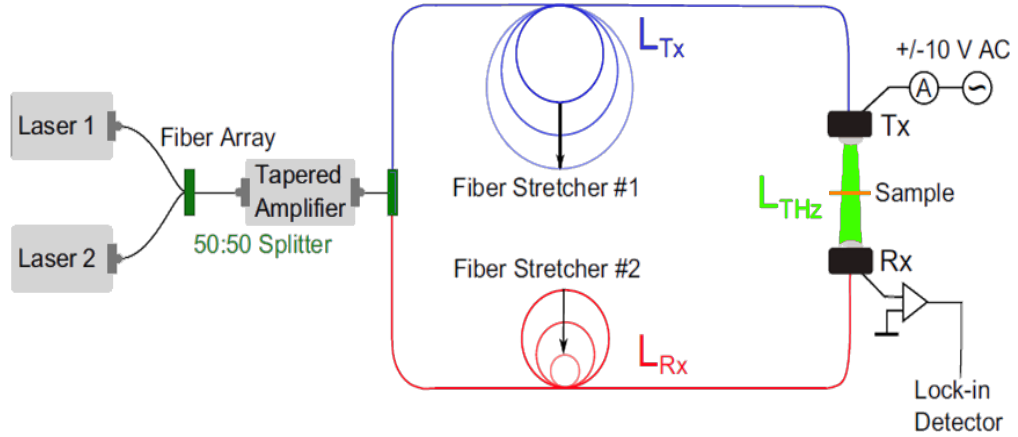


Figure 1.1: Main components of the cw THz spectrometer. The superimposed signal of two DFB lasers is amplified and split into two equal parts and guided to the two photomixers used as transmitter and receiver. Two fiber stretcher modulate the path-length to the transmitter (L_{Tx}) and the receiver (L_{Rx}). Sample is placed in the optical path with length (L_{THz}) between the two photomixers.

the power specifications of different sources and detectors. Additionally it can be adapted for example when external cooling allows for an increased laser power on the photomixers, see Sec. 1.2. The combined signal is split up into two equal parts which are guided via optical fibers to the two photomixers used as transmitter and receiver. The photomixers are described in more detail in Sec. 1.3. They determine not only the intensity of the THz radiation due to their efficiency [11], but also the polarization properties of the THz radiation, see Sec. 2, and contribute to the measured phase, see Sec. 3. The two fibers on the way to both photomixers have a length of over 60m each due to the embedded fiber stretchers. Changing the length of the optical fibers modulates the phase which enables the extraction of the amplitude and the phase of the measured signal at each frequency [12], compare also Sec. 3.

The last part concerning the photomixers, the optical path (L_{THz}), and the position of the sample within can be varied to meet special requirements for each experiment in particular. Optical lenses can be embedded to focus the light onto the sample and/or linear polarizers can be used if necessary. An optical cryostat in the beam path can change the sample temperature from room temperature down to 3 K [13], that allows for a detailed investigation of low temperature phases. A further option is a magnetic-field setup, where the whole part including photomixers and sample is placed directly inside a magneto-cryostat. This is explained in more detail in Sec. 1.2. The whole electronics of the setup is placed on a mobile rack and can easily be moved to different labs, giving access to a variety of cryostats.

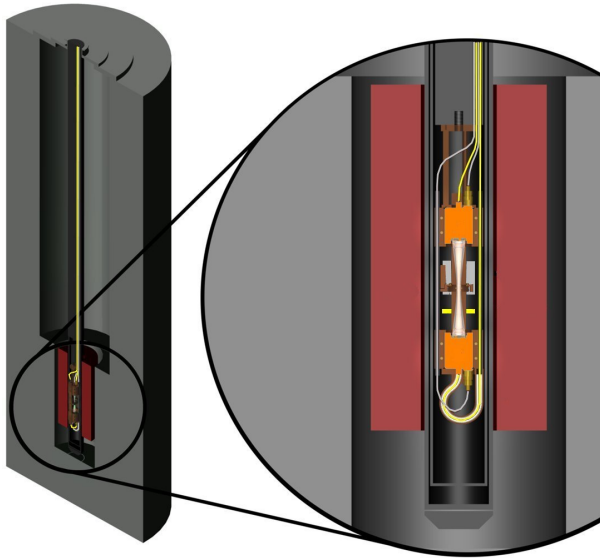


Figure 1.2: *Magnetic-field setup inside the magneto-cryostat. Optical fibers guide the laser light to the photomixers used as transmitter and receiver inside the cryostat, directly at low temperature and in high magnetic field. Sample and reference aperture can be interchanged at any temperature or field using a piezo-rotator. For details of the compact face-to-face assembly, see Fig. 1.3.*

1.2 Design of the magnetic-field setup

In this setup, the antennae for creating and detecting the THz radiation are placed directly in the magneto-cryostat, at low temperatures and in high magnetic field, see Fig. 1.2. The advantage of the setup is that it overcomes the need for optical windows or focusing optics which are usually associated to the usage of an optical cryostat. Additionally, the inevitable cooling of the photomixers in this design improves the signal-to-noise ratio by providing the ability to increase the laser power incident on the photomixers to further increase the signal strength, and by reducing the noise in the photomixers. Furthermore, the mobile spectrometer in combination with the magnetic-field setup gives access to several magneto-cryostats with different maximum magnetic-field strength and different magnetic-field configuration allocated at the University of Cologne. The only requirement is that the diameter of the magnet bore is large enough for the variable temperature insert (VTI) which contains the photomixers [14, 15].

To overcome the need for optical windows in the cryostat, optical fibers are transferred through vacuum-tight feed-troughs. About two meters of fiber lead to the two photomixers at positions P_A and P_B , see Fig. 1.3. The stability of the thermal gradient in the fibers plays an important role for the polarization stability of the laser light in the fibers and also for the stability of the optical path-length difference, which will be discussed in Sec. 4.3.

The size is limited by the dimensions of the bore in the magnet and the space requirements for vacuum shield and radiation shield of the VTI. The maximum diameter of the face-to-face assembly is 34 mm; the length is 16 cm, whereas the distance between the photomixers is around 6 cm. The antennae are equipped

with silicon lenses emitting a predominately parallel beam with a small, frequency dependent opening angle of the THz beam [16]. Therefore no additional focusing components are required. Two optional tungsten wire-grid polarizers with titanium frames¹ can be embedded in the optical path when linear polarization is required, see Fig. 1.3.

An aperture mounted on a piezo-rotator allows to change sample and reference directly at any temperature or field while a temperature sensor placed on the aperture provides accurate information of the sample temperature. Since both photomixers are illuminated with nearly 30 mW laser power, the temperature directly at the photomixers rises when switching on the lasers. The laser power can be increased to 100 mW using the tapered amplifier, what limits the possibility of reaching the base temperature of 3 K but drastically increases the intensity of the THz radiation. To provide a good heat transfer to the cooling head of the VTI, almost all parts of assembly are made out of copper. The radiation shield prevents heating of the vacuum shield, and thereby the helium bath, by leading the radiated heat to the helium gas phase at the top of the cryostat. For a proper temperature regulation at the sample position, despite of the low thermal conductivity of the piezo-rotator, additional copper wires from the aperture were connected to the copper-made holder of the piezo-rotator. This allows a heat transport directly to the cooling-head of the VTI.

The room temperature stability of the setup was investigated previously. Details on the stability of the frequency and the phase can be found in Refs. [16, 17]. The length drift of the system was found to be up to a few tens μm for a path-length difference of roughly 3.3 cm. This deviation is attributed to thermal drifts. With this magnetic-field setup, thermal drifts are expected to play a superior role since the temperature of the fibers drops from close to 300 K over 1.3 m of fiber to 3 K. On the way to the magnetic-field setup, both fibers of the transmitter and receiver arm are placed in close proximity to ensure a minimal temperature difference between them. Close

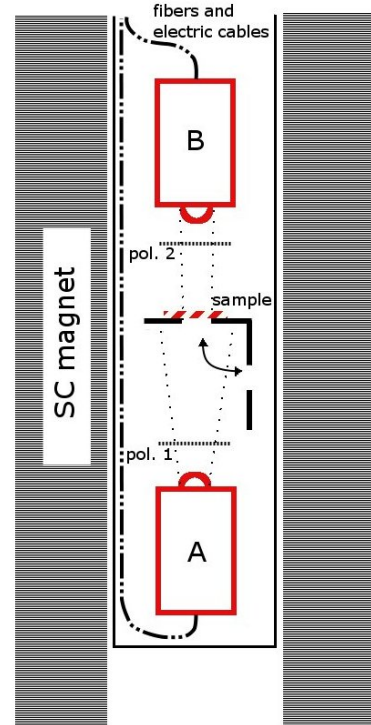


Figure 1.3: Compact face-to-face assembly in cryo-magnet. Sample is placed at the center on a piezo-rotator that allows interchanging sample and empty reference aperture. The THz signal, created and detected by transmitter (P_A) and receiver (P_B) directly at low T and high B . Two wire grid polarizers (pol.1 and pol.2) can be inserted if necessary.

¹Build in cooperation of the mechanical workshop of the II. Institute of Physics in Cologne and the Max Planck Institute for Radioastronomy in Bonn

to the photomixers, those fibers have to split up, leaving approximately 20 cm to 25 cm of length ² especially vulnerable to temperature change. This may be caused actively by changing the temperature at the sample, changing the magnetic field leads to boiling off of some helium and a reduction of the temperature in the VTI, or simply over time by a reduction of the helium level in the surrounding cryostat. A further discussion is given in Sec. 4.3, where also the successful reduction of this drift, using a three laser based phase correction, is presented.

1.3 THz antennae

The antennae were provided by the Max-Planck-Institute in Bonn concerning the low temperature versions. They were designed by I. Mayorga, detailed information on the principles discussed in this paragraph can be found in [11]. The log-spiral antenna structure consists of a 10/200 nm thick Ti/Au layer and was processed on the GaAs substrate using standard electron beam lithography [18]. The photomixing area in the center is covered by an interdigitated finger structure of about $9 \times 9 \mu\text{m}^2$. In the area covered by this structure, the illumination of the photoactive substrate with laser light leads to electron-hole excitations. The charge carriers at the photomixer used as transmitter are accelerated by an applied bias voltage and travel through the substrate to the fingers and along the spiral arms. The antennae radiate mainly from the so-called active region, see simulations in Ref. [19]. When the current travels along the spirals, there are regions where the current in two neighboring arms are out of phase and regions where they are in phase. The latter are the regions where radiation takes place. Detection is the inverse process to creation of THz radiation. The charge carriers in the illuminated substrate are accelerated by the THz electric field instead of an applied bias voltage, leading to a sensitivity to amplitude and phase of the measured field. Since the measured phase depends on the exact optical path which the signal has traveled, the assumption of the frequency-dependent active region has to be taken into account as well. A further discussion is given in Sec. 3.2 and in Sec. 7. Due to the log-spiral design, the created THz radiation can be circular over a broad range, while also the detection process at an identical photomixer is almost only sensitive to the same circular polarization. A further discussion and some spectra proving the circular character of this particular setup are presented in Sec. 2.

²Consisting of both fibers and THz path, see Eq. 3.

2 Measuring with circularly polarized light

Several recent studies show the interest of the THz community in generating and detecting broadband, circularly polarized radiation. Especially in the time domain, huge efforts have been made recently by actively modulating the polarization using four-contact photoconductive antenna [20], spiral metamaterials [21], laser-induced plasma [22], or a Fresnel rhomb [23] to create circularly polarized beams over a broad frequency range. The properties of spiral photoconductive antennae as transmitter were also investigated using both time-domain and cw THz spectrometers by Gregory *et al.* [24]. The circular polarization detection property of a spiral antenna was shown by Tsuzuki *et al.* [25].

2.1 Measurement principle

Historically there are two different conventions in the literature concerning the notation for right-handed circularly polarized (RCP) and left-handed circularly polarized (LCP) waves. Polarization can be defined from the point of view from the source or from the point of view at the detector. The two different conventions will result in the opposite descriptions for the same wave. We will use the first definition where RCP (LCP) corresponds to a counterclockwise (clockwise) rotation of the electric field vector when looking along the direction of energy transfer. This means positive helicity refers to a wave described by $(\mathbf{p}-i\mathbf{s})/\sqrt{2}$ (negative : $(\mathbf{p}+i\mathbf{s})/\sqrt{2}$) defined by a triplet of vectors, $(\mathbf{p},\mathbf{s},\mathbf{k})$ which form a right-handed system.¹ Throughout the thesis we will stick to this. Polarization states of light can be described using the Jones formalism. The electric field is

$$\mathbf{E}(t) = E_0 \begin{pmatrix} e^{i\phi_x} \\ e^{i\phi_y} \end{pmatrix}$$

¹ \mathbf{p} and \mathbf{s} stay for “parallel” and “senkrecht” as typical in optics.

where E_0 is the amplitude of the field and ϕ_x (ϕ_y) is the phase of the x (y) component. LCP and RCP light can be described as

$$\mathbf{E}_{RCP} = \frac{E_0}{\sqrt{2}} \begin{pmatrix} 1 \\ -i \end{pmatrix}, \quad \mathbf{E}_{LCP} = \frac{E_0}{\sqrt{2}} \begin{pmatrix} 1 \\ i \end{pmatrix}$$

A linear polarizer P_{lin} converts circularly polarized light of one handedness into equal parts of circularly polarized light with opposite handedness and half the initial amplitude:

$$\begin{aligned} P_{lin,x} \mathbf{E}_{LCP} &= \begin{bmatrix} 1 & 0 \\ 0 & 0 \end{bmatrix} \frac{E_0}{\sqrt{2}} \begin{pmatrix} 1 \\ i \end{pmatrix} = \frac{E_0}{\sqrt{2}} \begin{pmatrix} 1 \\ 0 \end{pmatrix} \\ &= \frac{1}{2} \frac{E_0}{\sqrt{2}} \begin{pmatrix} 1 \\ -i \end{pmatrix} + \frac{1}{2} \frac{E_0}{\sqrt{2}} \begin{pmatrix} 1 \\ i \end{pmatrix} \\ &= \frac{1}{2} \mathbf{E}_{RCP} + \frac{1}{2} \mathbf{E}_{LCP} \end{aligned}$$

Measuring samples which show, for example, significant natural optical activity needs an easy solution for measuring both circular polarizations independently. Even knowing photomixers to favor left-handedness does not immediately help when the response to LCP and RCP light is expected to be different. The polarization dependence of this setup was previously determined using linear polarizers and/or waveplates [16, 26] but with older versions of the photomixers. A new method is described in Fig. 2.1. Photomixer 1, acting as source, creates light with left handedness (green). Lens 1 converts the slightly diverging beam into a collinear beam which can be transformed into linearly polarized light (grey) using a linear polarizer. A second lens (2) focuses the light onto the sample². Afterwards, lens 3 again creates a collinear beam. Without mirror, lens 4 focuses the light on the detector 2. Now, the fact that the detector is selectively sensitive to only one chirality comes in handy, since it only detects the left circular part of the light which passed through the sample.

To access the information contained in the right handed part, a removable mir-

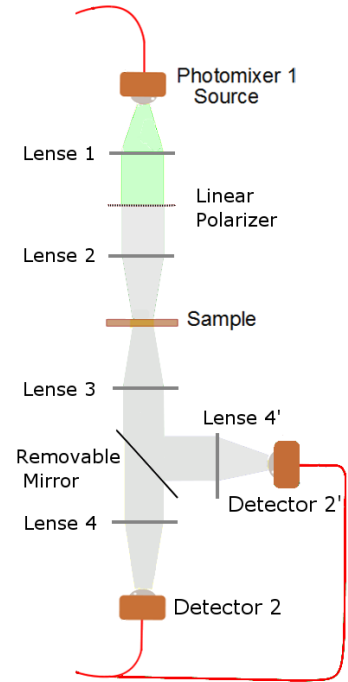


Figure 2.1: Left circular polarized light (green) from the source is converted to light with equal amounts of left- and right-handedness (grey) by a linear polarizer. The detector 2 is only sensitive to the left-handed part. Inserting a mirror directs the beam to detector 2'. Upon reflection, light changes chirality. Detector 2' measures again only the LCP light, which interacted with the sample as RCP light

²The focused beam can be guided through the windows of an optical cryostat. This is not relevant for the discussed principle, therefore it is not shown in Fig. 2.1

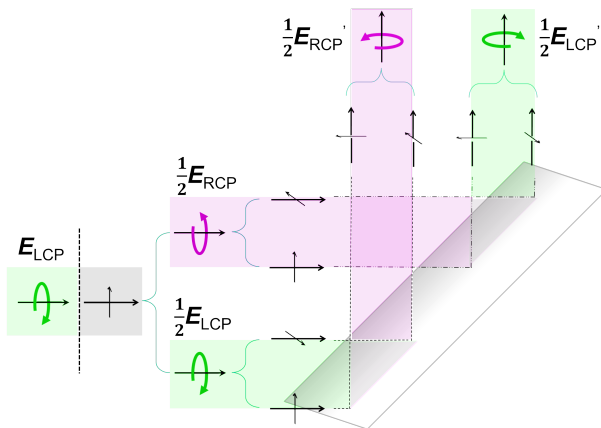


Figure 2.2: Conversion of left-handed circularly polarized light, split by a linear polarizer into E_{LCP} (green) and E_{RCP} (magenta) light, into E_{RCP}' light and E_{LCP}' light upon reflection from a metal plate.

ror is placed in the parallel beam behind the sample. Upon reflection, a LCP (RCP) wave transform into a wave with opposite handedness (see Fig. 2.2). This means that light which passes the sample as RCP (magenta) becomes LCP (green). Moving the focusing lens 4 and the photomixer 2 in Fig. 2.1 to positions 4' and 2' enables to detect amplitude and phase of this part.

A stainless steel plate as helicity converter works rather well, a rough calculation will give an idea of the conversion efficiency. The Drude contribution [27] can be used to estimate the refractive index at THz frequencies to be $n \approx 100$ at 1 THz and $n \approx 200$ at 300 GHz. The Brewster angle $\theta_B = \arctan(n_{air}/n_{steel})$ is $\approx 89.42^\circ$ at 1 THz (and higher for lower frequencies). The calculated reflection coefficients are $r_s = 0.986$ and $r_p = 0.972$ at 1 THz. Therefore the ratio for incident circular light after reflection is 0.986, leading to a slight ellipticity. The phase of r_s remains unchanged, whereas the phase of r_p is changed by exactly 180° so that the information contained in the left- and right-handed phase respectively remains unchanged³ as shown in Fig. 2.2. The THz amplitude of E_{LCP} (green in Fig. 2.3) measured at position 2 (see Fig. 2.1) with a linear polarizer between lens 1 and lens 2 reaches roughly 50 nA at 200 GHz and decreases towards 5 nA at ≈ 700 GHz. At 1 THz, the signal is still 2 nA. Due to the long THz path in air (≈ 80 cm), water vapor absorption lines at 560 GHz, 750 GHz, and 988 GHz are clearly visible. The rest of the spectrum is dominated by oscillations with a period of ≈ 24 GHz caused by the booster, and a superposition of faster oscillation caused by standing waves between the different optical components. For comparison, the measured E_{RCP} is depicted as magenta line. Water absorption lines as well as the setup specific modulation of the spectrum are well reproduced. The overall amplitudes of the two polarizations are comparable at low frequencies but RCP is slightly lower between 300 GHz and 550 GHz and above 650 GHz [28]. The large difference in the standing waves causes the ratio LCP/RCP to cover a broad range of 40 % (red; Fig.2.3 lower panel). This is not surprising since by changing components in the

³This is only true for angles smaller than the Brewster angle.

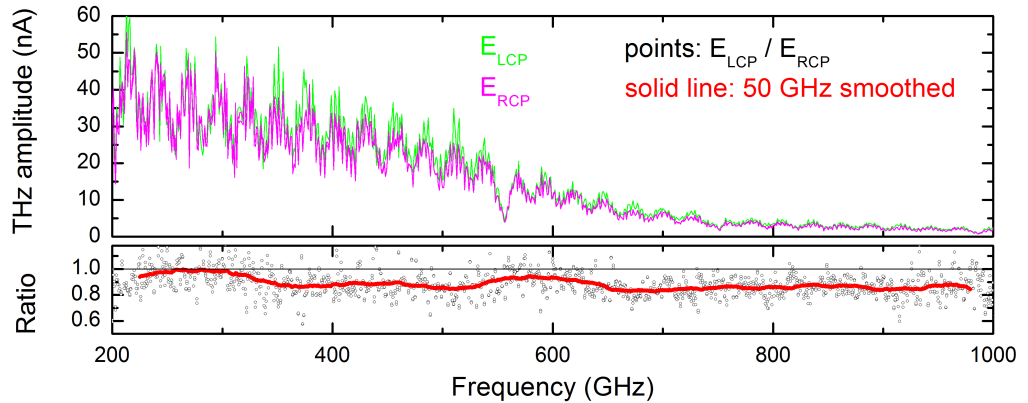


Figure 2.3: *Top: THz amplitude of the LCP (green) and RCP (magenta) part of linear polarized light measured using the geometry described in Fig. 2.1. Bottom: Ratio of LCP to RCP THz amplitude (black, points) averaged over 50 GHz (red, solid) to overcome contributions caused by standing waves in two different THz paths.*

THz path, the conditions for standing waves change completely. Smoothing the data over 50 GHz (red, solid line) diminishes the influence of the standing wave⁴. The signal strength for LCP and RCP is comparable over the whole frequency range and therefore an equal sensitivity for both helicities of light gives the possibility to explore also small differences between them.

Figure 2.4 shows the path-length difference ΔL for both measurements (upper panel). Again, we see the water vapor absorption lines at 560 GHz, 750 GHz, and 988 GHz. The frequency dependence of ΔL is explained in Sec. 3. Measuring ΔL of RCP light (magenta) leads to a small offset due to a change in L_{THz} . In both cases, the receiver arm is slightly longer than the transmitter arm, leading to the negative sign⁵. The contributions from $\Delta\phi_{an}(\nu)$ and $\Delta\phi_{RC}(\nu)$ (Sec. 3.2) have to be the same for both measurements, so subtracting ΔL_{RCP} from ΔL_{LCP} (lower panel, red line) should, in first approximation, lead to a frequency independent offset. The difference between the green and the magenta data is $175 \mu\text{m}$ above 600 GHz. Between 300 GHz and 600 GHz, L_{THz} seems to be slightly larger (up to $15 \mu\text{m}$) for measuring with the mirror. Below 300 GHz the deviations rise to $70 \mu\text{m}$. The most probable reason is the different radius of the parallel beam for different frequencies. At 200 GHz, the full-width at half maximum (FWHM) behind the collimating lens is 3.5 cm. Between 200 GHz and 400 GHz this reduces drastically to 1.6 cm, whereas for higher frequencies, especially above 700 GHz, the

⁴Note that the exact shape of this ratio is, especially for higher frequencies, very sensitive to the overall alignment!

⁵This is desirable, since introducing a sample in the THz path will prolong ΔL . The phase error strongly depends on $|\Delta L|$, see Sec. 3.7.

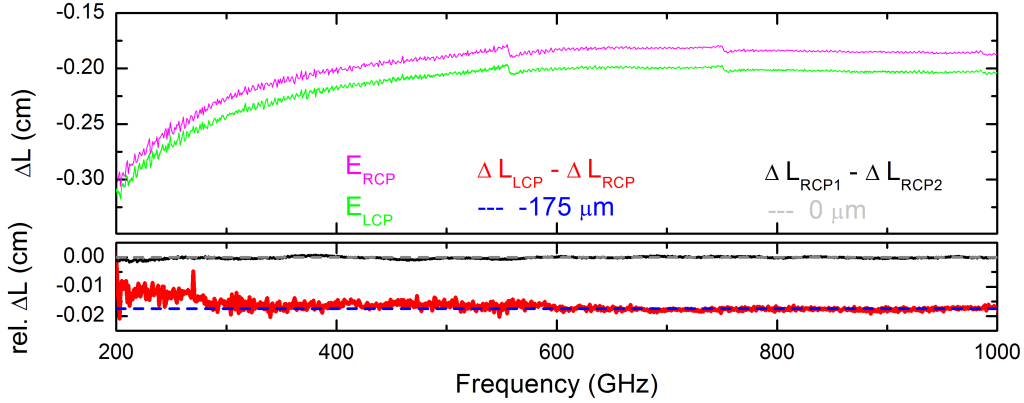


Figure 2.4: Top: ΔL of the left-handed (green) and right-handed (magenta) part of linear polarized light measured using the geometry described in Fig. 2.1. Bottom: Difference between left- and right-handed ΔL (red, solid) and difference between two successive measurements of ΔL with right-handed light (black, circle).

FWHM stays nearly constant with a diameter of 0.8 cm [16]. A small deviation from perfect alignment of the mirror will affect the traveled path for lower frequencies more. Most importantly, after everything is installed, measuring ΔL_{RCP} several times leads to the same result. The difference $\Delta L_{RCP1} - \Delta L_{RCP2}$ is less than $5 \mu\text{m}$ (black, lower panel).

2.2 Pseudo-transmittance

To prove how pure the polarization state over the measured frequency range is, a rather simple experiment can be performed. Expecting the transmitter to exclusively radiate left-handed circularly polarized light, the light wave will, upon reflection on the mirror, be transformed into an electromagnetic wave with right handedness. Since the detector ideally should be insensitive to this, no signal can be measured. Whatever signal is still recorded is coming from one of the following scenarios:

- The transmitter emits elliptically polarized light, leading to a small right-handed part which is transformed to a left-handed wave upon reflection. This can be detected by the detector.
- The polished metal plate does not perfectly transform the left handedness into right handedness, leading again to a finite signal at the detector.

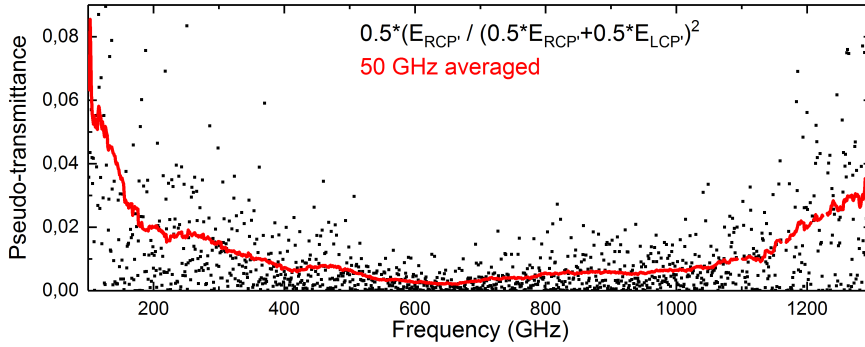


Figure 2.5: Intensity of the non-prioritized polarization direction compared to the total intensity hitting the detector (black, dots) averaged over 50 GHz (red, solid). Spectrum shown from 100 GHz to 1300 GHz.

- The receiver is not exclusively sensitive to left-handed light. It partially records right-handed light. Thus is the same as point 1.

Comparing the recorded amplitude with and without linear polarizer directly gives a ratio which can be understood as a pseudo-transmittance of the non-prioritized polarization. The result can be seen in Fig. 2.5. The intensity E_0^2 without polarizer after reflection is reduced to $0.5 \cdot E_0^2$ with the linear polarizer, accounting for the factor of 0.5 when calculating the pseudo-transmittance. At first, the pseudo-transmittance is dominated by the shift of the standing waves induced by inserting the linear polarizer in the THz beam. It shows a spread over several percent (black dots) at low frequencies. Smoothed data increases to a maximum of $\approx 5\%$ at 110 GHz and $\approx 2\%$ at 200 GHz. Above 1.1 THz it shows a slight increase to 3% over the next 200 GHz. Above 1.1 THz, the increase of the pseudo-transmittance is caused by the expected increasing ellipticity (see below) of the photomixers [24, 26]. Between 300 GHz and 1100 GHz, captured intensity from right handed light is less than 1% of the intensity measured with a linear polarizer.

2.3 Discussion

The antenna geometry favors one handedness of circularly polarized light, namely LCP light. Reflecting the light from a metal plate changes the handedness of the radiation to RCP. The pseudo-transmittance shown in Fig. 2.5 gives an idea of the purity of the circular polarization because any ellipticity in the emitted THz radiation or in the sensitivity of the receiver would lead to an increased signal. To measure the response of a sample to RCP light, a linear polarizer directly behind the transmitter provides equally left- and right-handed polarized light which can be guided through a sample. Now, in the reflected light, the originally RCP

light transforms to LCP. The polarization selective receiver measures this part independently. The results show that this comparably simple approach provides an excellent sensitivity to both circular polarizations. For higher frequencies, the area of the photomixers responsible for creating and detecting the THz radiation becomes smaller. This increases the influence of the finger structure, which is expected to develop a purely linear behavior, leading to an increasing ellipticity (compare p. 16.). The proportion of light with the other polarization state is less than 2% from 200 GHz to 1200 GHz.

A further improvement could be made either using a gold mirror where the conductivity and therefore the refractive index is larger, leading to a higher reflectivity. Additionally, changing the setup around the cryostat enables measuring at steeper angles of $\approx 30^\circ$. The rather large size of the collinear THz beam and therefore the need for large lenses 3 and 4' will prevent a further decrease of this angle. Those two improvements might lead to a ratio from r_p to r_s of 0.997% after reflection. Nevertheless, the difference to the already archived ratio of 0.986% is negligible in the current investigation, the signal is large enough for both helicities to measure a circular response over a broad frequency range. Important is that, if an absorption suppresses the transmittance in RCP light to less than 1% of the transmittance in LCP light, the absolute strength can not be determined from the transmittance alone, except that it might be possible to decrease the thickness of the sample.

3 Group Delay

The ability of measuring the phase directly for each frequency is one of the great advantages of cw THz spectroscopy. In chapter 8.1 we will show an example where the phase data allows the determination of sample properties even though the amplitude is strongly influenced by diffraction. It is mandatory to investigate limitations of the accuracy of these measurements by experimental and environmental conditions, e.g. design of the lenses, precision or stability of the lasers, or the surroundings of the measurement setup. If all contributions are precisely determined, influences of deviations from ideal measurement conditions can be discussed according to their impact on the precision of a measurement. The results discussed in this part have already been published [29].

In our setup, we extract the information of both amplitude and phase information using two fiber stretchers [12]. They are positioned in the optical path where both laser frequencies are superimposed but before the two photomixers, see Sec. 1.1. They change the optical path-length difference

$$\Delta L = L_{Tx} + L_{THz} - L_{Rx} \quad (3.1)$$

where L_{Tx} is the optical length of the fiber in the transmitter arm, L_{Rx} the optical length of the fiber in the receiver arm, and L_{THz} is the length of the THz path in free space. Phase data for different values of ΔL obtained in reference runs without any sample are shown in Fig. 3.1. At high frequencies, the dominant behavior is linear, whereas at lower frequencies a strong deviation from this linearity can be seen. In the following we will discuss all different contributions to the phase difference $\Delta\varphi(\nu)$ stemming from the optical fibers in both fiberarms, the transmitter and receiver photomixer, and the THz path L_{THz} , including everything between the two photomixers. A combination of all these contributions will result in a model used for fitting the data accurately in the linear and non-linear regime.

3.1 Contribution from optical fibers

The center wavelength of the lasers is around 780 nm. Depending on the desired THz frequency, both lasers (1,2) are symmetrically detuned from the center frequency $\nu_{1,2} = \nu_0 \pm \Delta\nu/2$ where $\Delta\nu$ is the terahertz frequency $\nu_2 - \nu_1$. To cover

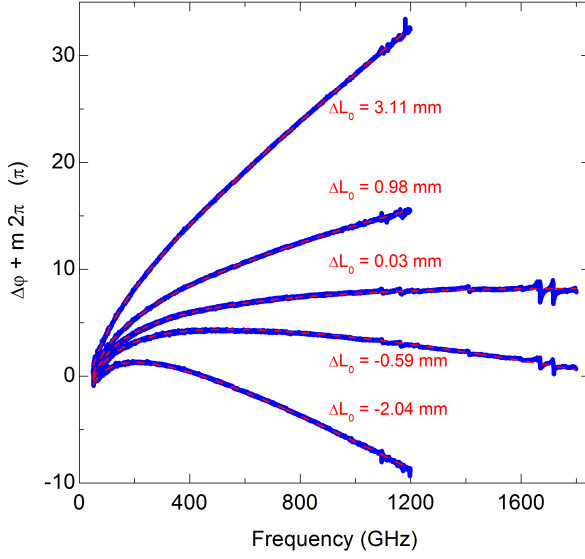


Figure 3.1: Different data sets of $\Delta\varphi(\nu)$ (blue) measured in face-to-face configuration. L_{THz} (≈ 22 cm) was changed to obtain different values of ΔL . Frequency step width was 1 GHz except for $\Delta L \approx -0.06$ mm where 100 MHz was chosen. Calculated values of $\Delta\varphi_{mod}(\nu)$ (red) fitted using Eq. 3.6 with parameters $\Delta\phi_{an}(\nu_{max}) = 0.27\pi$ and ΔL as can be seen in the plot. The comparison between data and model yields $m \cdot 2\pi = 8\pi$.

the range from 0 to 1.8 THz, the lasers wavelength has to be tuned over a range of about 2 nm each. The fibers in our setup have a light conducting core of fused silica (SiO_2), which has a linear dispersion of about $\delta n/\delta\nu = 4 \cdot 10^{-5}/\text{THz}$ [30]. For the refractive index $n_f(\nu_{1,2})$ of the fiber follows

$$\begin{aligned} n_f(\nu_{1,2}) &= n_f(\nu_0) + \left. \frac{\delta n_f}{\delta\nu} \right|_{\nu_0} \cdot (\nu_{1,2} - \nu_0) \\ &= n_f(\nu_0) \pm \left. \frac{\delta n_f}{\delta\nu} \right|_{\nu_0} \cdot \frac{\Delta\nu}{2} \end{aligned}$$

For the length L_f of a fiber, the phase φ_f of the optical beat is given by

$$\varphi_f = L_f [n_f(\nu_2) \cdot \nu_2 - n_f(\nu_1) \cdot \nu_1] \cdot \frac{2\pi}{c} \quad (3.2)$$

With this, we find

$$\varphi_f = L_f \left(n_f(\nu_0) + \left. \frac{\delta n_f}{\delta\nu} \right|_{\nu_0} \cdot \nu_0 \right) \cdot \frac{2\pi\nu}{c} = L_f \cdot n_{f,eff} \cdot \frac{2\pi\nu}{c}.$$

The frequency-independent part in parentheses gives rise to a slight increase $n_{f,eff}/n_f \approx 1.01$, mainly because the two lasers are scanning in opposite direction from the

center frequency ν_0 . Thus, only $n_{f,eff} \cdot L_f$ is relevant for the optical beat and the contribution of the optical fiber is

$$\Delta\varphi_f = (L_{Tx} - L_{Rx}) \cdot \frac{2\pi\nu}{c}$$

Here, L_{Tx} and L_{Rx} include the effectively frequency-independent refractive index $n_{f,eff}$ of the fibers.

3.2 Contribution of the photomixers and antennae

The photomixers, each consisting of antenna, substrate, and silicon lens, deliver several contributions to the measured phase. The use of two (nearly) identical photomixers has the advantage that contributions which similarly apply to L_{Rx} and L_{Tx} cancel out. The coupling of the optical beat into the photoactive area is identical on both sides, hence it does not contribute to $\Delta\varphi$.

The photoconductance G depends on the terahertz frequency due to the finite carrier lifetime τ [11]. In both photomixers, this gives rise to a phase shift of $\varphi_G = \arctan(2\pi\nu\tau)$ [24, 30]. This phase shift delays the terahertz wave in the transmitter with respect to the optical beat, which effectively increases L_{Tx} . The phase shift in the receiver on the other hand effectively increases L_{Rx} . Therefore both contributions cancel out and do not contribute to $\Delta\varphi$.

The total impedance of the photomixer and antenna is described by a characteristic time constant $\tau_{RC} = R_A C$. R_A describes the antenna resistivity of the log-spiral antenna on the GaAs substrate [11, 31]. The contribution is nearly frequency independent, therefore $R_A \approx 73 \Omega$ is assumed to be constant, as the capacitance $C \approx 1.5 fF$ of the interdigitated electrode structure [11]. The time constant $\tau_{RC} \approx 0.1 ps$ results in a phase shift of $\varphi_{RC} = \arctan(2\pi\nu\tau_{RC})$ in both, transmitter and receiver photomixer. In case of the transmitter and receiver, it contributes to L_{Tx} . An ultra-wideband log-spiral antenna exhibits a strong dispersion and thus distorts short pulses [19, 32, 33, 34, 35]. The antenna effectively radiates and receives THz from the so called active region, see Sec. 1.3. A center-fed log-spiral antenna radiates where the current contributions of the two neighboring spiral arms, depending on the wavelength λ , interfere constructively. The radius of this active region is $r_{ar} = \frac{\lambda}{2\pi}$. A wave with higher wavelength has to travel a longer way $l(\nu)$ to the active region than one with lower wavelength, leading to an additional delay [35]. In time, the signal has to travel for

$$t_{gr,an(\nu)} = l(\nu) \cdot \frac{n_{eff}}{c} \tag{3.3}$$

where $t_{gr,an(\nu)}$ denotes the group delay of the antenna and n_{eff} is the effective refractive index, which can be calculated to be $n_{eff} = \sqrt{(12.8 + 1)/2} \approx 2.6$ using

the dielectric constant $\epsilon_{GaAs} = 12.8$. The path of the spiral can be calculated to

$$l(\alpha(\nu)) = \int_0^\alpha \sqrt{r(\alpha')^2 + \left(\frac{dr}{d\alpha'}\right)^2} d\alpha' = \frac{\sqrt{1+\alpha^2}}{\alpha} (r_{ar}(\nu) - r_{min}).$$

The minimum and maximum wavelength are defined by the inner and outer truncations respectively. With the radii $r_{min} = 10 \mu$ and $r_{max} = 430 \mu\text{m}$ and $\nu_{min,max} = c/2\pi r_{min,max} n_{eff}$, they are found to be $\nu_{max} \approx 1.8 \text{ THz}$ and $\nu_{min} \approx 40 \text{ GHz}$, while

$$l(\nu) = \frac{c}{2\pi n_{eff}} \frac{\sqrt{1+\alpha^2}}{\alpha} \left(\frac{1}{\nu} - \frac{1}{\nu_{max}} \right).$$

The frequency dependence of the group delay can be described as

$$t_{gr} = \frac{1}{2\pi} \frac{\partial \varphi_{an}}{\partial \nu}$$

which we now integrate from ν_{max} to ν using Equ. (3.3):

$$\int_{\nu_{max}}^\nu t_{gr} d\nu = \int_{\nu_{max}}^\nu \frac{\sqrt{1+\alpha^2}}{2\pi\alpha} \cdot \left(\frac{1}{\nu} - \frac{1}{\nu_{max}} \right) d\nu = \frac{1}{2\pi} [\varphi_{an}(\nu) - \varphi_{an}(\nu_{max})]. \quad (3.4)$$

At each frequency, for the nearly identical photomixers as transmitter and receiver, this contribution should be identical in both photomixers. Since this delay effectively prolongs the transmitter arm in both cases, the two contributions add up. This yields the final expression of the antenna characteristics for the phase difference $\Delta\varphi_{an}(\nu)$ between the two arms,

$$\Delta\varphi_{an}(\nu) = \frac{2\sqrt{1+\alpha^2}}{\alpha} \left[\ln \left(\frac{\nu}{\nu_{max}} \right) - \frac{\nu}{\nu_{max}} + 1 \right] + \Delta\varphi_{an}(\nu_{max}), \quad (3.5)$$

where $\Delta\varphi_{an}(\nu_{max})$ describes an offset and is treated as a fit parameter. Within the Si lenses, standing waves can cause periodic modulations of $\Delta\varphi(\nu)$ [36, 37]. This effect is not important for the overall behavior of $\Delta\varphi(\nu)$, so it can be neglected for the discussion here. Nevertheless, if one considers the uncertainty of the phase as the derivative $\partial\Delta\varphi/\partial\nu$, this effect plays an important role, see Sec. 3.7.

3.3 Contribution of the terahertz path

The optical path length difference ΔL 3 contributes a term $\Delta L \frac{2\pi\nu}{c}$ to $\Delta\varphi(\nu)$. This is in principle depending on the frequency ν due to water vapor in the terahertz path and standing waves between both photomixers, or photomixers and sample, but for the discussion of the overall behavior of $\Delta\varphi(\nu)$ these effects deliver small contributions compared to the one of $\Delta\varphi_{an}(\nu)$. Here, it is sufficient to consider a constant value of L_{THz} . The frequency-dependent contributions nevertheless will be discussed later, see Sec. 3.7.

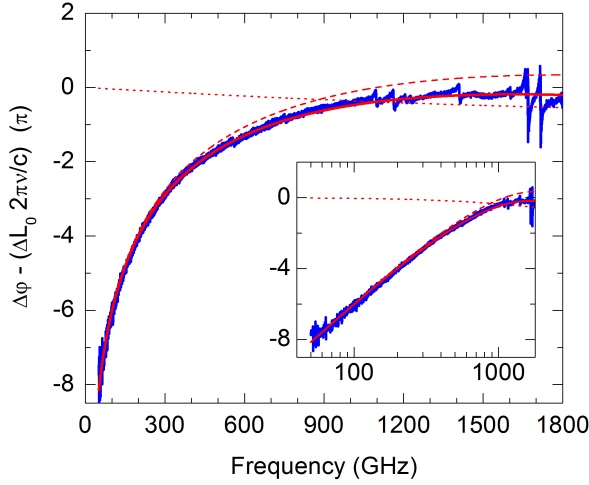


Figure 3.2: Nonlinear contributions of measured phase data and model. $\Delta\varphi(\nu) - \Delta L_0 \cdot 2\pi\nu/c$ for the data set with $\Delta L \approx -0.06$ mm (blue) and the modeled $\Delta\varphi_{an}$ (red dashed) and $\Delta\varphi_{RC}$ (red dotted). Both modeled contributions add up to $\Delta\varphi_{mod} - \Delta L_0 \cdot 2\pi\nu/c$ (red solid). Same data on a logarithmic frequency scale is shown in the inset

3.4 Combination of all contributions

Having determined the main contributions for $\Delta\varphi(\nu)$, we derive a model for the overall behavior taking into account the photomixer impedance (Sec. 3.2), antenna contribution (Sec. 3.2) and a constant optical path-length difference ΔL_0 (Sec. 3.3),

$$\Delta\varphi_{mod}(\nu) = \Delta\varphi_{an}(\nu) + \Delta\varphi_{RC}(\nu) + \Delta L_0 \cdot \frac{2\pi\nu}{c}. \quad (3.6)$$

Using the values of the lifetime $\tau_{RC} = R_{AC} = 0.1$ ps, the spiral growth rate $a = 0.2$ and $\nu_{max} = 1.8$ THz, there remain two free parameters ΔL_0 and the constant offset denoted by $\Delta\varphi_{an}(\nu_{max})$, see Eq. 3.5. This simple model delivers a very accurate description of the experimental data of $\Delta\varphi_{an}(\nu_{max})$, see Fig. 3.2. Considering an additional fit parameter $\gamma = \lambda/2\pi r_{ar}$, one finds $\gamma = 0.997$, indicating that the previous assumption for $\lambda = 2\pi r_{ar}$ is quite accurate. $\Delta\varphi_{an}(\nu_{max})$ is then found to be 0.26π .

The non-linear terms $\Delta\varphi_{an}$ and $\Delta\varphi_{RC}$ can be compared directly to the measured $\Delta\varphi(\nu) - \Delta L_0 \cdot 2\pi\nu/c$ (see Fig. 3.2). The antenna contribution clearly dominates the behavior since it changes by more than 6π between 100 GHz and 1 THz. In the end we can define an effective, frequency-dependent optical path-length difference $\Delta L_{eff}(\nu)$ which is correlated to a corrected phase difference $\Delta\varphi_{corr}(\nu)$ through $\Delta L_{eff}(\nu) = \frac{c}{2\pi\nu} \cdot \Delta\varphi_{corr}(\nu)$. The corrected phase difference is described as the measured phase difference $\Delta\varphi(\nu)$ minus the two dominant non-linear terms $\Delta\varphi_{an}$

and $\Delta\varphi_{RC}$:

$$\Delta L_{eff}(\nu) = \frac{c}{2\pi\nu} \cdot \Delta\varphi_{corr}(\nu) = \frac{c}{2\pi\nu} \cdot (\Delta\varphi(\nu) - \Delta\varphi_{an} - \Delta\varphi_{RC}) \quad (3.7)$$

The result is shown in Fig. 3.3. The frequency-independent offset ΔL_0 equals the averaged effective optical path-length difference $\Delta L_{eff}(\nu)$, whereas all frequency dependence of $\Delta L_{eff}(\nu)$ and accordingly of $\Delta\varphi(\nu)$ contains all deviations between $\Delta\varphi_{mod}(\nu)$ and the measured data of $\Delta\varphi(\nu)$. Without the large contributions of $\Delta\varphi_{an}$ and $\Delta\varphi_{RC}$, the frequency dependence of $\Delta L_{eff}(\nu)$ highlights the smaller contributions, i.e., the effective frequency dependence of ΔL_{THz} . Three main contributions can be identified.

- Standing waves within the Si lenses give rise to a modulation period of about 4.1 GHz, see inset Fig.3.3.
- Standing waves between the Si lenses separated by $\Delta L_{THz} \approx 22$ cm cause a modulation of 0.7 GHz.
- Resonant absorption features of water vapor.

Whereas the first two are setup specific, the resonant absorption features of water vapor, which can be seen in the main plot of Fig. 3.3, can be compared to literature [38, 39]. The absorption lines are well resolved regardless of the relatively short path in air. As a first estimate, the absorption line at 557 GHz is expected to cause a peak change of about $2 \cdot 10^{-4}$ of the refractive index of air [39]. For $L_{THz} \approx 22$ cm, this corresponds to a change of about $40 \mu\text{m}$, in good agreement with our data. The two other contributions are periodic features, therefore they are better resolved in the Fourier-transformed data, see Section 3.6.

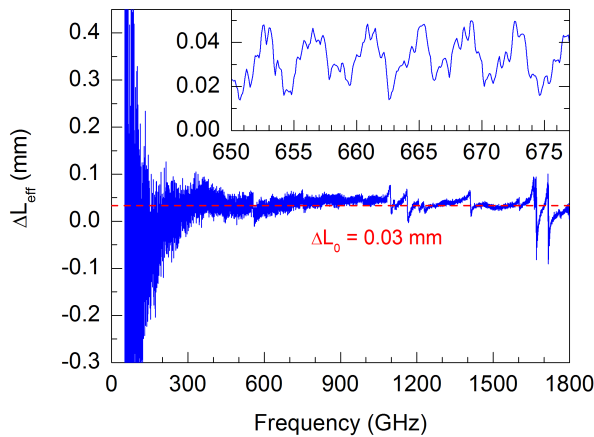


Figure 3.3: Effective optical path-length difference ΔL_{eff} for the data set with $\Delta L_0 \approx 0.03$ mm, cf. Eq. 3.7. Inset shows 4.07 GHz and 0.7 GHz modulation on the same data in the range of 650 GHz to 677 GHz. Modulations stem from Si lenses of the photomixers as well as standing waves in the optical path L_{THz} between the two lenses. Data measured with 0.1 MHz step size.

3.5 Active region

The design of the antennae was discussed in section 1.3. The center-fed antenna radiates mainly from the so called active region, where the currents flowing in the two spiral arms are in phase, giving rise to a constructive interference of the radiated waves [19, 40]. Following the two spiral arms r_+ and $r_- = r_+ \cdot e^{a\pi}$, where a is the growth rate of the spiral, we consider the radius of the active region r_{ar} to be a spot with $r_{ar} = (r_+ + r_-)/2$ which is located between the two neighboring arms. The path lengths of the two arms differ by $l(r_+) - l(r_-) = l(\alpha + \pi) - l(\alpha)$. Since the antenna is fed in a balanced way, the currents at the minimum radius $\pm r_{min}$ are out of phase ($\alpha = 0$). Constructive interference occurs when the path length difference between the two arms compensates for the initial phase shift of π . The spiral radius is described as

$$r(\alpha) = r_{min}e^{\alpha a} \quad (3.8)$$

with r_{min} equal to the minimum radius ($\approx 10 \mu\text{m}$) and $a = 0.2$ as the spiral growth rate. Using Eq. 3.4, one can find

$$\frac{\lambda}{2} = l(\alpha + \pi) - l(\alpha) = \frac{\sqrt{1 + a^2}}{\alpha} (r_{ar}(\nu) - r_{min})(e^{a\pi} - 1). \quad (3.9)$$

The minimum radius r_{min} is very small compared to the wavelength, therefore can be neglected for further evaluation. With this, the radius of the active region amounts to

$$r_{ar} = \frac{r_+ + r_-}{2} = \frac{a}{4\sqrt{1 + a^2}} \frac{e^{a\pi} + 1}{e^{a\pi} - 1} \cdot \lambda \quad (3.10)$$

using the same expression as before, $\gamma = \lambda/2\pi r_{ar}$, we find $\gamma = 1.01$, in excellent agreement with our experimental results of 0.997. Theoretical studies of the radiated power density as a function of $1/\gamma$ have been reported for different spiral antenna with different growth rates [41]. Here, for log-spiral antennae with a growth rate of $a \approx 0.18 \approx 1/\tan(80^\circ)$, the power density shows a rather broad asymmetric peak at $2\pi r = \lambda/2$. It decreases only slowly towards higher values of r . In order to get a first moment, integrating from $2\pi r = 0.2\lambda$ to 2λ leads to about 0.9λ .

3.6 Quasi-time-domain analysis

With the amplitude E_{THz} and the phase difference $\Delta\varphi(\nu)$ for a discrete set of frequency points of a certain measurement, the Fourier series as a function of the

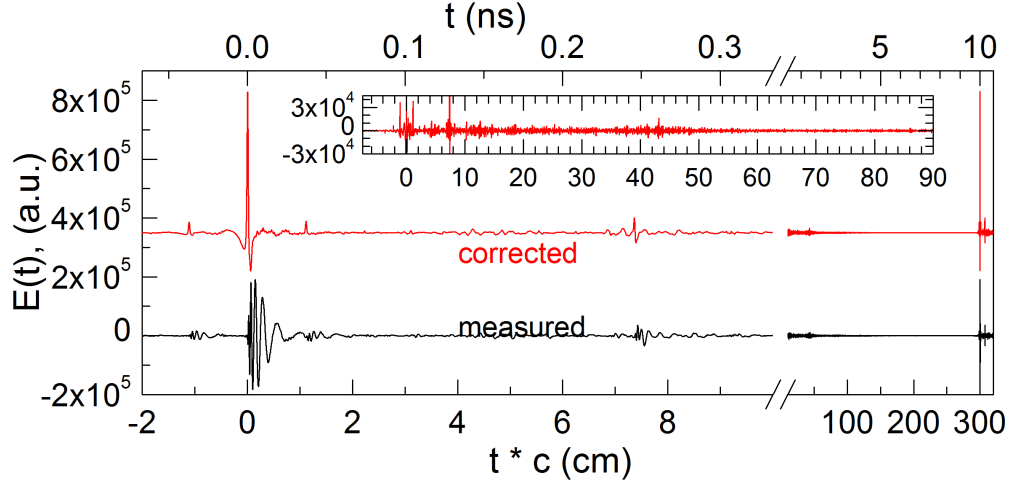


Figure 3.4: Fourier series $E(t)$ of the data (black) measured up to 1.8 THz for $\Delta L \cong -0.06$ mm (data from Fig. (3.3)) and after correction (red). Data are offset for clarity. Scale changes at 10 cm. Measurement with frequency step width of 100 MHz yields a period of $T \cong 300$ cm. Inset shows corrected data on a different scale. Feature shifted by 7.36 cm with respect to the main peak is caused by standing waves in the Si lenses, the peak at 43.1 cm corresponds to $2 \cdot L_{THz}$ and results from standing waves between the two photomixers.

time

$$E(t) = \sum_{\nu} E_{THz}(\nu) \cos(2\pi\nu t - \Delta\varphi(\nu)) \quad (3.11)$$

can be calculated. This approach is known as quasi-time-domain analysis [42]. The Fourier series is equivalent to an interferogram or to the waveform in a time-domain terahertz experiment, where all frequencies are measured simultaneously. The main peak in the Fourier series is expected at the time $t = \Delta L/c$. The measured data of $E(t)$ (black line in Fig. 3.4) show a strong asymmetry around any peak. In contrast to well-defined peak positions, this is the typical shape of a strongly down-chirped signal, in which the higher frequencies arrive first. This is another visualization of the frequency dependence of the group delay introduced by the antennae. Therefore, as expected, using the corrected phase difference $\Delta\varphi_{corr}(\nu)$, see Eq. (3.7), in the Fourier series

$$E_{corr}(t) = \sum_{\nu} E_{THz}(\nu) \cos(2\pi\nu t - \Delta\varphi_{corr}(\nu)) \quad (3.12)$$

removes the down-chirp and yields a pronounced "pulse" at the expected position (red line in 3.4).

The remaining peak width is caused by the limited bandwidth of the experiment and in particular the strongly decreasing amplitude with increasing frequency, see Fig. 3.4. The corrected data shows in total 5 peaks. Next to the main peak, at ± 1.1 cm (corresponding to a ≈ 27.25 GHz modulation period), a peak occurs due to standing waves in the tapered amplifier. The amplifier is positioned before the fiber splitter, so the same modulation is later present in both fibers to the transmitter and the receiver and thus does not appear in $\Delta\varphi(\nu)$, i.e., are only observed in the amplitude. Additionally, a feature shifted by 7.36 cm (≈ 4.07 GHz modulation period) is visible. This reflects the periodic modulations shown in the inset of Fig. 3.3, which are caused from standing waves within the Si lenses. The feature at 43.1 cm (≈ 0.7 GHz modulation period) reflects the standing waves between the two photomixers with $2 \cdot L_{THz} \approx 2 \cdot 22$ cm, Fig. 3.4. The feature at 86 cm is attributed to the first overtone. Using the corrected data clearly facilitates the precise determination of such features in the Fourier series.

3.7 Group delay and uncertainty of the phase

The quantitative understanding of $\Delta\varphi(\nu)$ allows to further discuss the influences of experimental uncertainties determining the remaining errors of the measured phase difference. In our setup, the two experimental uncertainties contributing to the uncertainty $\delta\varphi$ of the measured phase difference $\Delta\varphi(\nu)$ are the uncertainties of the optical path-length difference ΔL and the THz frequency ν

$$\delta\varphi = \frac{\partial\Delta\varphi(\nu)}{\partial\nu} \cdot \delta\nu + \frac{2\pi\nu}{c} \cdot \delta L. \quad (3.13)$$

The stability of the optical path-length difference is typically within $\delta L = \pm 5 \mu\text{m}$, see Ch. 4. The line width of the two tunable lasers determines the line width of the beat signal, which amounts to about 5 MHz. The long term frequency stability was observed to be better than 20 MHz [5]. On the typical timescale of one sample and reference measurement which takes less than 1 h, the frequency stability is better than $\delta\nu = 5$ MHz. The first term of Eq. 3.13 is proportional to the group delay difference $\Delta t_{gr} \propto \partial\Delta\varphi/\partial\nu$. Starting from Eq. 3.7, we will determine the size of the errors for the different contributions.

$$\frac{\partial\Delta\varphi(\nu)}{\partial\nu} = \frac{\partial\Delta\varphi_{an}}{\partial\nu} + \frac{\partial\Delta\varphi_{RC}}{\partial\nu} + \frac{\partial\Delta L_{eff}}{\partial\nu} \cdot \frac{2\pi\nu}{c} + \Delta L_{eff} \cdot \frac{2\pi}{c} \quad (3.14)$$

The last term, $\Delta L_{eff} \cdot 2\pi/c$, dominates for large values of ΔL but can be suppressed by choosing a small ΔL . For a larger value of $\Delta L = 1$ cm it amounts to 0.2/GHz.

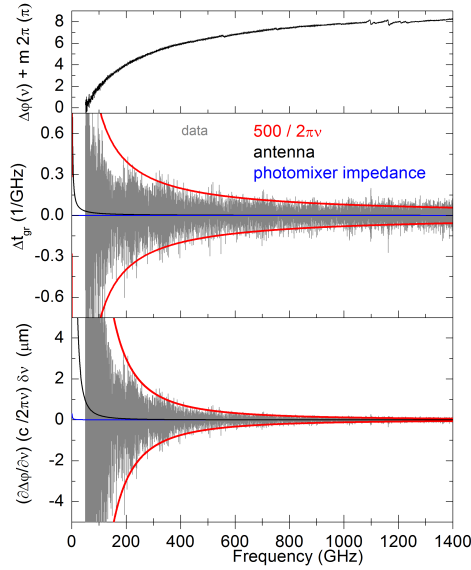


Figure 3.5: Top panel: Phase difference $\delta\varphi(\nu)$ for $\Delta L \approx -0.06$ mm as shown in Fig. 3.1 measured with 100 MHz as frequency step size. Middle panel: Group delay difference Δt_{gr} compared to the contributions of the photomixer impedance (green) and the antenna (black). The blue curve gives a rough estimate of the envelope. Bottom panel: same data but multiplied by $(c/\nu)\partial\nu$ with $\partial\nu = 5$ MHz for comparison with a change ∂L of the length.

For the data shown in Fig. 3.5 with a $\Delta L \approx -60 \mu\text{m}$, this term can be neglected, leaving three relevant contributions.

For the first two terms we find

$$\frac{\partial\Delta\varphi_{an}}{\partial\nu} = \frac{2\sqrt{1+a^2}}{a} \cdot \left(\frac{1}{\nu} - \frac{1}{\nu_{max}}\right), \quad \frac{\partial\Delta\varphi_{RC}}{\partial\nu} = \frac{4\pi\tau_{RC}}{1 + (2\pi\nu\tau_{RC})^2} \quad (3.15)$$

The comparison with the experimental data in Fig. 3.5 shows that these terms can equally be neglected. The contributions $\Delta\varphi_{an}$ and $\Delta\varphi_{RC}$ dominate the overall behavior of $\Delta\varphi(\nu)$ but the derivative can be neglected when looking at $\frac{\partial\Delta\varphi}{\partial\nu}$. This leaves the third term $\frac{\partial\Delta L_{eff}}{\partial\nu} \cdot \frac{2\pi\nu}{c}$, which dominates the behavior of $\partial\varphi/\partial\nu$. This is caused in particular by the contributions of the standing waves within the Si lenses and between the two photomixers. To estimate the uncertainty of the length, we roughly describe the envelope of $\partial\varphi/\partial\nu$ by $f(\nu) = \pm 500/\nu$ for $\Delta L \approx -0.06$ mm and $L_{THz} \approx 22$ cm, see bottom panel of Fig. 3.5. In order to compare the effects of frequency uncertainty versus length drift, we consider

$$\partial\varphi \cdot \frac{c}{2\pi\nu} = \frac{\partial\Delta\varphi}{\partial\nu} \cdot \frac{c}{2\pi\nu} \cdot \partial\nu + \partial L \quad (3.16)$$

We use the experimental result for the envelope of $\pm 500/\nu$ and $\partial\nu = 5$ MHz to evaluate the first term to $0.12 \mu\text{m} \cdot (\text{THz}/\nu)^2$, which amounts to $3 \mu\text{m}$ at 200 GHz or $0.75 \mu\text{m}$ at 400 GHz, see middle panel of Fig. 3.5. As stated earlier, the typical length-drift observed in our setup is approximately $\pm 5 \mu\text{m}$. So for a $\partial L = \pm 5 \mu\text{m}$, and a path-length difference ΔL smaller than 1 cm, the uncertainty of the

phase for frequencies above 200 GHz is dominated by drifts of the optical path-length difference, in agreement with experimental results discussed in Ref. [5]. Knowing this, monitoring the drifts of the optical path-length difference provides a possibility for increasing the accuracy of the phase data. A method for correcting the drift induced changes will be described in the next chapter.

4 Self-normalized phase measurement

The simultaneous determination of amplitude and phase of an electromagnetic wave is highly advantageous. It means obtaining both real and imaginary part of the dielectric function $\epsilon(\omega) = \epsilon_1 + i\epsilon_2$ independently. The measured transmittance $\tilde{T}(\omega)$ depends on the apertures used for sample and reference measurement which have to be identical and have to be placed at the exact same spot in the THz beam. The intensity that goes through the reference has to be the same as the intensity incident on the sample. The measured phase depends on the change in the THz beam path. Placing the sample in the beam path will always prolong the THz beam path based on the optical thickness of the sample. All external parameters (temperature, field etc.) should be the same for measuring both quantities.

When working with focusing optics such as lenses or mirrors, an adjusted focus on the empty reference aperture will be brought forward as soon as a medium with $n > n_{air}$ is placed in the beam path. Optimizing the setup on the sample or reference will lead to an offset solely due to this fact. This effect increases for an increasing optical thickness of the material ($n \cdot d$). Measuring in a parallel beam will minimize this effect. For the phase, the accuracy does not depend on the intensity¹ of the detected light, but more on the frequency stability of the lasers and therefore directly the THz frequency, and the constancy of the length for the signals traveling to detection. A difference in the traveled path of the THz radiation between sample and reference causes only an additional phase offset.

Measuring the relative change of amplitude or phase as a function of varying external parameters (frequency, temperature, field etc.) is quite accurate. Two remaining sources for errors are either time-related changes in the amplitude or time-related drifts of the length causing changes in the phase¹. In the first case, the photo-current correction can partially compensate for a difference in the emitted THz intensity [43]. In the second case, a third laser can be implemented to measure the drift of optical path-length difference and accordingly correct the phase [16, 17]. Results and discussions in Ref. [44] are based on data measured within this thesis. The method and the basic results will be discussed and extended towards applications for measuring in magneto-cryostats under variation of external parameters.

¹Obviously, a very low THz amplitude would limit the accurate determination of the THz phase. This statement refers to small changes in the amplitude, leading to a slight inaccuracy in the measured transmission

¹Additionally there can also be frequency-related problems which will be discussed further in Sec. 7

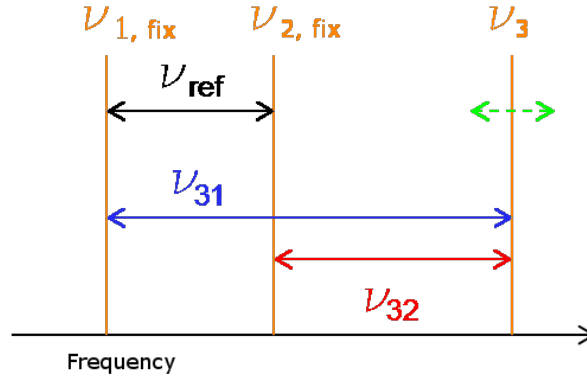


Figure 4.1: Three different laser frequencies ν_1 , ν_2 (both fixed), and ν_3 (fixed or tunable) result in three difference frequencies ν_{ref} , ν_{31} , and ν_{32} in the THz range.

4.1 Concept of measuring with three THz frequencies

The dominating factor for an error in the phase in our setup is the uncertainty ∂L , as already discussed in Sec. 3.7. The third laser can be used to obtain information on the drift ∂L by measuring a constant reference phase of two fixed lasers (Fig. 4.1). Any drift of this phase corresponding to a time dependent change of ΔL can be used as a reference to the two simultaneously measured phases. A description of the concept is also given in [16] and [44].

One laser is kept fixed at a frequency ν_1 by locking it to a Rb absorption line. This ensures a frequency stability of 1 MHz. The frequency of the second laser (ν_2) is tuned to achieve a desired reference frequency $\nu_{ref} = \nu_1 - \nu_2$. The difference frequency ν_{ref} can be adjusted to fit to the circumstances of each sample and measurement individually, e.g. it should be in a transparent region of the sample, which can change if certain external parameters as temperature or magnetic field are changed.

Once this frequency ν_{ref} is chosen, tuning the third laser to the frequency ν_3 generates two further difference frequencies $\nu_{31} = \nu_3 - \nu_1$ and $\nu_{32} = \nu_3 - \nu_2$. ν_3 can either be fixed to measure three fixed THz frequencies simultaneously, e.g. while varying other parameters like the sample temperature or external field. ν_3 can be tuned to simultaneously record two sweeping difference frequencies ν_{32} , ν_{12} and a fixed reference ν_{ref} . The frequency stability of ν_2 and ν_3 is ≈ 5 MHz [5].

Before looking at the drifts in detail, some estimates can be made. The expected size of the drift in ΔL depends on the difference in length between $L_{Tx} + L_{THz}$ and L_{Rx} (see Eq. 3). If all sections are made of the same material, e.g. in air, and $\Delta L = 0$, a simultaneous change in the temperature in both arms does not induce a drift $\partial\varphi$. Still, a change in the temperature between the two arms will induce a drift $\partial\varphi$, depending on the thermal expansion coefficient α and the temperature

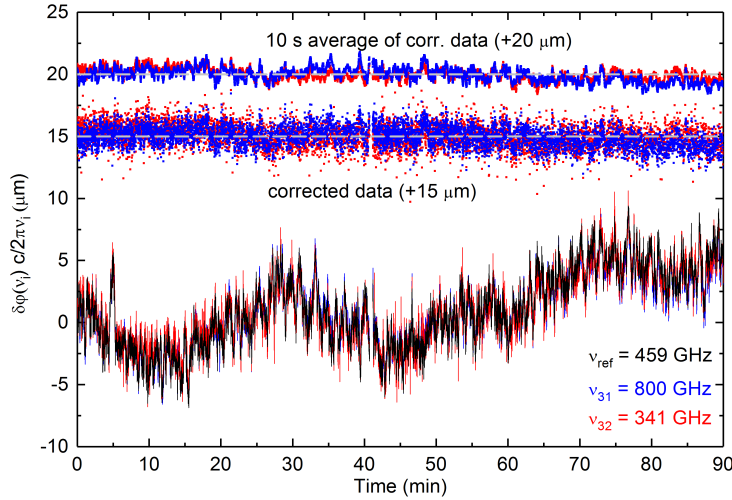


Figure 4.2: Solid lines: Three constant THz frequencies ν_i record the temporal drift $\partial L(t)$ of the optical path-length difference. Symbols: corrected values for $\partial L_{31}(t) - \partial L_{\text{ref}}(t)$ (red) and $\partial L_{32}(t) - \partial L_{\text{ref}}(t)$ (blue), shifted for better visibility.

difference ΔT .

If there are more sections of different materials, e.g. fibers for L_{Rx} and L_{Tx} and air for L_{THz} , the situation becomes more complicated, especially if temperature differences are involved. Even if ΔL at $T_0(t = 0)$ is 0, and in both arms the temperature change is equal, a deviation in the thermal expansion and/or thermo-optical coefficient of different parts will lead to a finite ΔL for $T \neq T_0$.

Lastly, sometimes it is already at room-temperature not possible to tune ΔL close to zero. For a setup without variable focusing objects and without the possibility to continuously adjust L_{THz} , see Sec. 1.2, a ΔL of about 1 cm is already close to the limit that can be achieved by cutting and splicing fibers. A finite ΔL makes the setup more vulnerable against drifts ∂L .

4.2 Three lasers and drift correction

For an optimized setup with small $\Delta L \approx 60 \mu\text{m}$, small ΔL_{THz} (≈ 20 cm), and small temperature variation $\Delta T = T - T_0$, the effect of drift and normalization method can be seen in Fig. 4.2. Due to the finite L_{THz} and the spatial separation of the receiver and transmitter arm (including L_{THz}), there is a finite drift of approximately $\pm 5 \mu\text{m}$ over 80 min. Plotting $(\partial\phi(\nu_i) - \partial\phi(\nu_{\text{ref}})) \cdot c/(2\pi\nu_i)$ shows that ΔL is determined to $\pm 1 \mu\text{m}$.

The effect of this normalization for a larger temperature difference between the two arms of the spectrometer can be seen in Fig. 4.3. The thermal contact of the two fiberstretcher was intentionally made worse, allowing 120 m of fibers in both fiberstretcher to take slightly different temperatures over time.

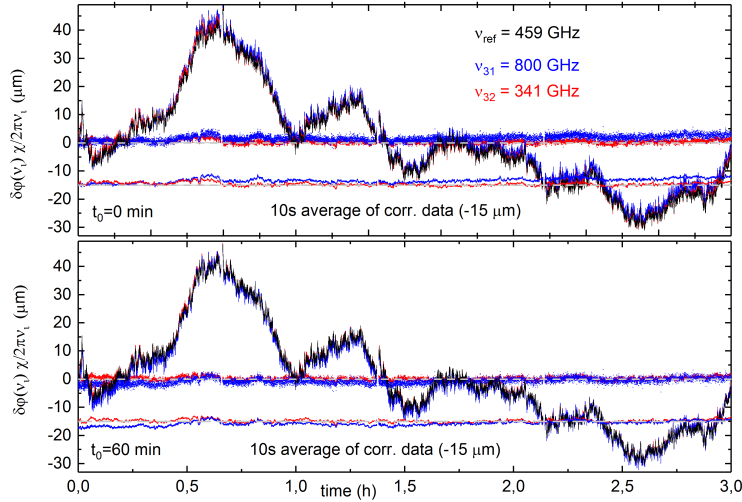


Figure 4.3: Phase drift $\partial\varphi(t)$ recorded for three constant THz frequencies ν_i over three hours. Data taken with bad thermal contact between the two fiberstretchers. Upper panel: corrected values $\nu_i - \nu_{ref}$ $t_0 = 0$ min (symbols). Lower panel: corrected values $t_0 = 60$ min (symbols), shows an offset induced by the correction.

Recording $\partial\varphi_i$ reveals an observed drift of $\pm 40 \mu\text{m}$. At room temperature, the thermo-optic coefficient $\frac{\partial n}{\partial T}$ in a GeO_2 -doped SiO_2 fibers is of the order of $1.5 \cdot 10^{-5}$ per K [45]. 120 m of fiber in both fiberstretchers with a maximal temperature difference of 1 K lead to a maximal drift of $1800 \mu\text{m}$. This would indicate a temperature difference of about 0.04 K between the two fiberstretchers, which is conceivable. Plotting the normalization $\nu_i - \nu_{ref}$ (red and blue symbols) on the first glance leads to a drastic reduction of the deviations to $\pm 2\text{-}3 \mu\text{m}$. Nevertheless after a certain time, or a different normalization $\partial\varphi(t = 10\text{s}) = 0$ or $\partial\varphi(t = 60\text{min}) = 0$, there is a slight difference in the drift for all three THz frequencies. The difference in the drift of the phase between the two frequencies 458 GHz and 341 GHz seems to be less than compared to 800 GHz. So there is a small frequency dependent difference $\partial L(\nu)$. For a ΔL close to zero ($\approx 60 \mu\text{m}$), the effect of the uncertainty of the frequency on phase error was already discussed to be roughly $3 \mu\text{m}$ at 200 GHz and $0.75 \mu\text{m}$ 400 GHz, see Sec. 3.7. Temporary more than doubling ΔL to ($\approx 140 \mu\text{m}$) induced by the thermal drift will allow the three frequencies to drift $\approx 0.43 \mu\text{m}$ at 800 GHz, $1.32 \mu\text{m}$ at 459 GHz, and $2.27 \mu\text{m}$ at 351 GHz. The maximum deviation for the three hour measurement between the two length-drift corrected dotted lines in Fig. 4.3 is $\approx 3 \mu\text{m}$, which is in very good agreement with this assumption. Drift corrections are usually more important for frequency sweeps. Measuring 10 frequency sweeps with a frequency resolution of 100 MHz takes 15 h, Fig. 4.4. The phase data recorded at $\nu_{ref} = 327$ GHz reveals a slow drift $\partial L(t)$ over time of about $60 \mu\text{m}$. The top panel shows the averaged ΔL_{eff} of all runs. The middle panel shows the standard deviation between the 10 runs for the corrected (red) and not corrected (black) data. The drift correction reduces the standard deviation from $15 \mu\text{m}$ to roughly $2 \mu\text{m}$. A detailed discussion can also be found in [44].

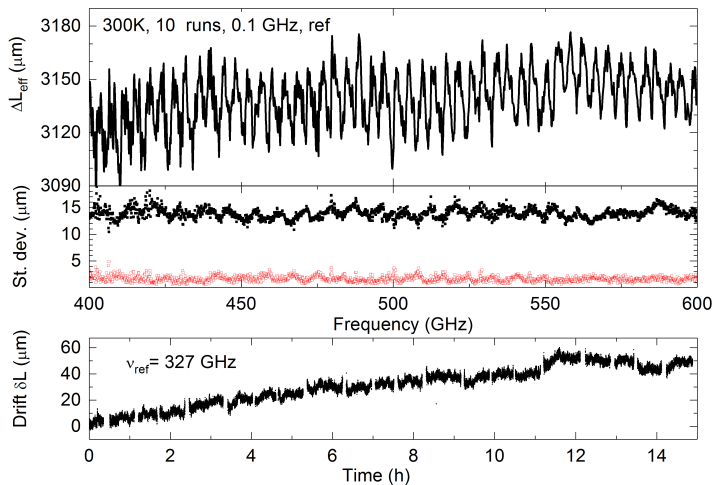


Figure 4.4: Corrected ΔL_{eff} in μm , averaged over 10 runs from 400 GHz to 600 GHz (top panel). Standard deviation in μm before (black solid points) and after (red open circles) correction (middle panel). Drift ∂L in μm for fixed reference frequency $\nu_{ref} = 327 \text{ GHz}$ over 15 hours (bottom panel).

4.3 Drift correction under extreme conditions

The opportunity which this method provides is improving the data quality in non-ideal circumstances or long-term measurements. Therefore it is a good method to be used in the magneto-cryostat, Sec. 1.2, to correct for most of the induced problems.

First, as already mentioned, this setup so far provides no easy solution to adjust the optical path length difference close to zero without cutting and splicing a fiber. This limits ΔL in most cases to around $\pm 1 \text{ cm}$. Secondly, there will be a temperature dependence of ΔL besides a drift. In the VTI, there are roughly 2 m of fibers of each fiber arm. The first roughly 70 cm are stored in a box close to room temperature, to provide spare fiber when new splicings in the VTI have to be done. The rest bridges the distance of 1 m from room temperature to the position of the photomixers which can be close to 3 K in the extreme case. Both fibers are lead in a way that they are mostly touching each other, but close to the upper photomixer, this is no longer possible. The last 20 cm of fiber leading to the lower photomixer have no counter part in the other fiber arm, they are compensated by fiber at higher temperature and the THz path in vacuum². The thermo-optic coefficient of the fibers in the VTI will induce a change in n while varying the temperature. Komma [46] investigated the thermo-optic coefficient of pure silica at 1550 nm for 300 K to 5 K. Our wavelength is 780 nm, but the study of Douglas [47] shows that the thermo-optic coefficient of fused silica does not show huge variances for a range from 400 nm to 2500 nm and between 300 K and 30 K. A conservative assumption for $\frac{\partial n}{\partial T} \approx 5 \cdot 10^{-6} / \text{K}$ from 50 K to 300 K indicates that 20 cm additional fiber in the receiver arm change ΔL by roughly $0.2 \text{ m} \cdot 250 \text{ K} \cdot 5 \cdot 10^{-6} / \text{K} = 250 \mu\text{m}$. This

²The lower photomixer in this setup in the current configuration is more efficient as receiver

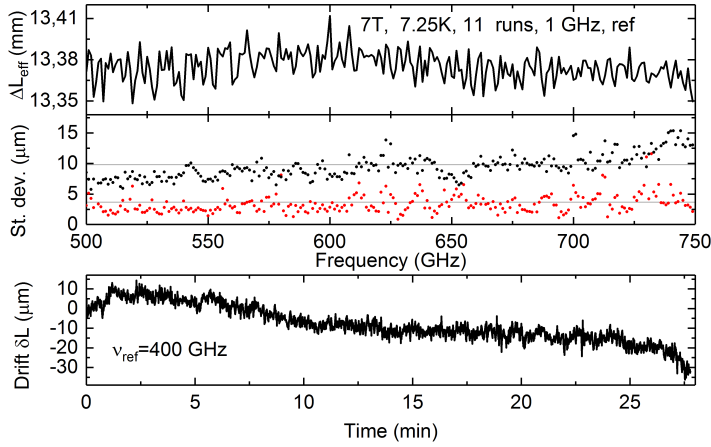


Figure 4.5: Corrected ΔL_{eff} in μm , averaged over 11 runs from 500 GHz to 750 GHz (top panel). Standard deviation in μm before (black circles) and after (red circles) correction (middle panel). Drift ∂L in μm for fixed reference frequency $\nu_{ref} = 400$ GHz over 30 minutes (bottom panel).

also indicates that, for a precise measurement, not only the temperature at the sample has to be as stable as possible. Any temperature change at any position in the VTI might induce a drift $\partial L(t)$.

4.3.1 Frequency sweep at low temperatures and constant magnetic field

Correcting a drift for a frequency sweep at low temperatures and in magnetic field is (comparably) easy. External parameters as temperature and field can be set in advance, and after some time the temperature gradient in the VTI will adjust. The time for this adjustment typically depends on the difference to the last stable temperature, ΔT , and the change in the magnetic field strength ΔB . It can be several minutes for small temperature changes at low temperatures but up to twelve hours for varying ΔT by 300 K, whereas changes in ΔB of 8 T require waiting times of 10 min to 15 min. The history of the cryostat also plays an important role there (e.g. helium level, last filling of the helium tank, etc.). In Fig. 4.5, an exemplary frequency sweep with a step size of 1 GHz from 500 GHz to 750 GHz at 7.25 K and 7 T can be seen. $\Delta L_0 = 1.334$ cm was obtained by fitting Eq. 3.6 to the phase data. The phase data recorded for ν_{ref} reveals a comparably large drift of $\partial L(t)$ of about $40 \mu\text{m}$ in 30 min. The data in the top panel was obtained by averaging over 11 frequency sweeps after drift correction, yielding a standard deviation σ of 3-4 μm (red symbols in the middle panel). ΔL_{eff} displays again the 4.1 GHz modulation originating from standing waves within the photomixers Si lenses³. σ

³Compared to Fig. 4.4, the modulation does not look so significant due to the different frequency step size of 1 GHz compared to 0.1 GHz, nevertheless, counting several maxima, the period is rather clear.

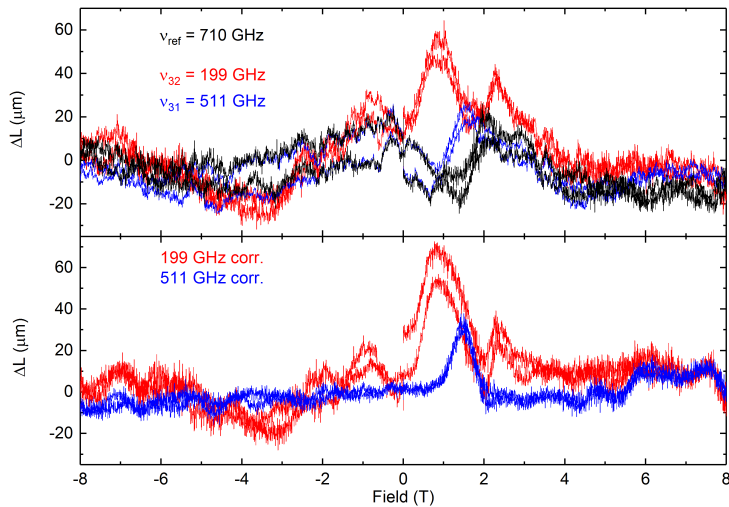


Figure 4.6: ΔL_{eff} in μm recorded at three fixed THz frequencies $\nu_{12} = 710$ GHz (black), $\nu_{31} = 511$ GHz (blue) and $\nu_{32} = 199$ GHz (red) for a magnetic field up and down sweep from 8 T and -8 T (top panel). Drift corrected ΔL_{eff} for 199 GHz and 511 GHz (bottom panel).

for the uncorrected data is $\approx 10 \mu\text{m}$.

4.3.2 Magnetic field sweeps

The situation for a magnetic field sweep or a temperature sweep for three constant THz frequencies is more complicated. Since the variation of the temperature at the sample position implicates a change in the temperature gradient along the fiber, large changes of n along the fiber will be unavoidable. Partially this will be compensated since the two fibers are kept in close proximity. One effect when changing magnetic field is helium boiling off at the magnet, which also disturbs the thermal gradient along the VTI. This leads to the same problems as for a temperature sweep. Additionally, a change in the magnetic field will result in a Lorentz force on the charge carriers in the antennae [48]. Since the measured photocurrent depends on the THz frequency [11], it is also plausible that different frequencies respond differently to the magnetic field. This will be a response depending on the photomixer temperature at that time, the measured photo current and the applied magnetic field as well as the field sweep rate.

An exemplary field-sweep measurement at $T=7.1$ K from 0 T to 8 T, -8 T, and back to 0 T is shown in Fig. 4.6. The top panel shows the drift of ΔL_{eff} for three different THz frequencies $\nu_{12} = 710$ GHz, $\nu_{31} = 511$ GHz, and $\nu_{32} = 199$ GHz. The drift-corrected data in the lower panel show a significant reduction in the deviation of the field up-sweep and field down-sweep. For small positive fields from 0 T to roughly 2 T, first there seems to be a frequency-dependent increase in the measured phase which makes it difficult to correct the drift ∂L by the drift recorded at another frequency. Secondly, the laser ν_3 seems to be the least stable,

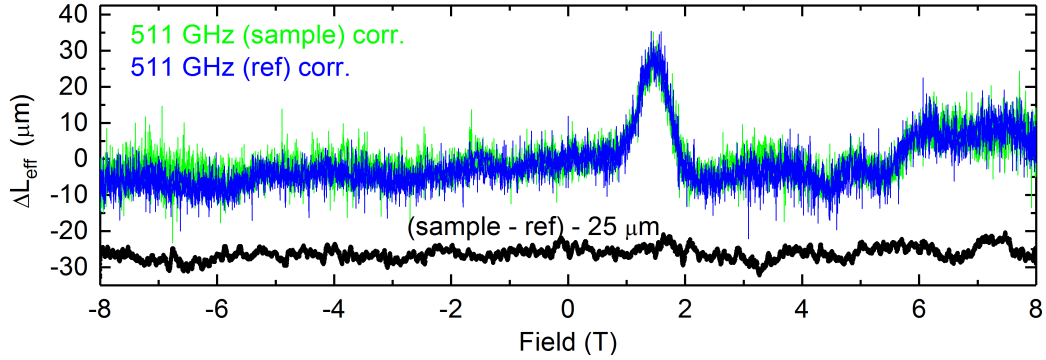


Figure 4.7: Corrected ΔL_{eff} in μm recorded for sample (green) and reference (blue) measurement at 511 GHz for a magnetic field up and down sweep from 0 T to 8 T, -8 T, and back to 0 T. 60 mT averaged deviation between corrected sample and reference measurement shifted by $-25 \mu\text{m}$ (black)

the drift recorded in ν_{31} and ν_{32} is larger than the drift in ν_{12} ⁴. The frequency-dependent shape of the field sweeps should be the same for different measurements, presuming the same conditions. Therefore a second measurement with a sample was performed. The sample in this case was a piece of Si with a thin film of a topological insulator on top. Pure Si is not expected to show any field dependence in this region, the measurement was performed to check whether a response of the surface state of the topological insulators can be captured. In this context, this measurement is used to demonstrate the maximal possible accuracy with this method and not to discuss the physics of this sample in particular.

The corrected data for 511 GHz of both sample and reference measurement is shown in Fig. 4.7. The field-dependent response of the photomixers at 1.75 T is well reproduced in the second measurement. Subtracting $\Delta L_{sample} - \Delta L_{ref}$ (open symbols, shifted by $-25 \mu\text{m}$, averaged over 60 mT) removes all features. A remaining uncertainty of $\pm 5 \mu\text{m}$ provides a great possibility to explore even small changes in magnetic fields.

4.4 Discussion

Measuring the phase accurately places other demands on the spectrometer than solely measuring the amplitude. It is shown that, for an optimized setup ($\Delta L \approx 0$, L_{THz} small, ΔT small), an accuracy of $\pm 1 \mu\text{m}$ for ΔL can be achieved, providing an excellent basis for monitoring small changes in the refractive index directly.

⁴The drift can be seen in the difference of the field up and the field down sweep, rather than the pure shape of the field sweeps themselves.

For non-ideal conditions, where large drifts make such observations usually impossible, this method is perfectly suited to monitor and correct environmentally induced changes, increasing the achievable accuracy to a point where the limitations given by the frequency stability of the lasers become important. Also for longterm measurements, where other things such as the day-night cycle in a lab building might become a problem, the method successfully provides a possibility for correction of those external influences to achieve a stability of about $\pm 2 \mu\text{m}$.

The high utility of a reference phase to correct for length-change-induced drifts is established when measuring with part of the setup under extreme conditions, for example inside a magneto-cryostat directly at low temperature and with varying external parameters (B, T). A frequency sweep at 7 T and 7.25 K exemplary shows that a drift ∂L is much larger ($\approx 40 \mu\text{m}$ over 0.5 h) compared to room temperature ($60 \mu\text{m}$ over 15 h). This is caused by the slightly larger ΔL due to missing possibility of manually adjusting L_{THz} freely, especially once inside the cryostat. Together with the large temperature gradient inside the VTI, this makes the setup vulnerable against temperature-induced drifts ∂L . The correction reduces the standard deviation σ of 11 measurements from $\approx 10 \mu\text{m}$ to $\approx 3.5 \mu\text{m}$.

A magnetic field sweep reveals the unique frequency-dependent response of the photomixers to temperature and field. Despite the mentioned problems for measuring in a magneto-cryostat, the reproducibility of those features in addition with the measured reference phase provides a stability of $\pm 5 \mu\text{m}$ for a relatively long measurement (80 min for each sample and reference measurement with a magnetic field sweep rate of 0.4 T/min). In order to maximize the effectiveness of the correction, the frequencies used should be as close together as possible.

Over all, measuring the optical phase length difference with an accuracy of less than $\pm 5 \mu\text{m}$ over a long time inside the cryostat is only possible with this method.

5 Chiral matter and non-reciprocal behavior

Chirality can be observed in everyday life. Everyone knows the example of a left human hand which looks like a right hand when looked upon through a mirror. In general, there are many other examples for chiral objects like a sea snail shell or a screw. In biology and chemistry there are such prominent examples as the DNA double helix or many different chiral molecules. Also in physics, following a long history starting with Lord Kelvin, who first used the term 'chiral' as a definition for an object which cannot be brought to coincidence with its mirror image in 1894, chirality is the driving force for many different phenomena. In optics, optical activity and circular dichroism are characteristic properties of chiral media. Optical activity denotes the polarization rotation of linearly polarized light due to a difference in the real part of the refractive index for negative helicity (n_-) and positive helicity (n_+). This results in an actual phase difference $\Delta\varphi \propto n_+ - n_-$ after passing through the sample, corresponding to a rotation of the polarization with respect to the plane of the incoming linear polarization. Circular dichroism describes the difference in absorption for left or right handed circularly polarized light. In 2003-2005, Pendry [49], Tretyakov [50], and Monzon [51] independently predicted that chiral media provide a novel route to a negative refractive index even without an external magnetic field. Considerable progress has been made in the fields of metamaterials and nanoplasmonics [52], however it took until 2009 to first demonstrate this effect in a chiral metamaterial [53]. The general assumption that a negative refractive index is not realized in natural materials was proven wrong when Pimenov and coworkers found the effect already 2005 in superlattices of $(\text{La}:\text{Sr})\text{MnO}_3$ and $\text{YBa}_2\text{Cu}_3\text{O}_7$ [54] and afterwards in the metallic ferromagnet $\text{La}_{2/3}\text{Ca}_{1/3}\text{MnO}_3$ [55]. But those two examples are not chiral materials.

In the most simple case, the different refractive indices for a chiral medium can be written as

$$n_{\pm} = \sqrt{\epsilon\mu} \pm \gamma \quad (5.1)$$

where γ denotes the chirality parameter. Obviously, if γ is larger than $\sqrt{\epsilon\mu}$, n becomes negative for one helicity. This is more easy to achieve if $\sqrt{\epsilon}$ is small. However, we will focus on a different phenomenon, non-reciprocal behavior in form of directional dichroism or quadrochroism. The discussion on non-reciprocity is

comprehensively unfold in two recent reviews, see Refs. [2] and [56]. The term non-reciprocity describes a process or a motion that differs for two opposite directions. For the optical properties, the symmetry requirements were discussed in detail by Szaller, Bordacs, and Kezsmarki [57]. One has to distinguish between i) non-reciprocal effects that show different responses for counterpropagating light beams irrespective of the light polarization, i.e. also for unpolarized light, and ii) non-reciprocal effects that hold only for certain polarizations such as the Faraday effect for circularly or linearly polarized light. The aim of this thesis is to discuss a representative of the former category i). This requires that the material shows no symmetry operation that can transform a given light beam of arbitrary polarization into a counterpropagating one with the same polarization. Accordingly, this requires the absence of spatial inversion symmetry and time-reversal symmetry. For more details, see Ref. [57]. An intuitive and straightforward possibility to achieve directional dichroism (or quadrochroism) is to consider a chiral medium in a finite magnetic field, see Sec. 5.1. Chirality breaks spatial inversion symmetry and the magnetic field breaks time-reversal symmetry. A chiral material shows natural optical activity, while the magnetic field gives rise to e.g. the Faraday effect and magneto-optical activity. It has been speculated for a long time that the combination of the 2 effects may give rise to magneto-chiral activity [58], see also Sec. 5.1.2. In the following, we will consider an even simpler possibility. We consider a chiral medium with a simple magnetic excitation. If the optical properties of this excitation depend on the light helicity in zero field, the Zeeman effect in finite field is sufficient to cause quadrochroism. Ni_3TO_6 is a chiral, polar and multiferroic material, what makes it an ideal candidate for the search of non-reciprocal effects because the crystal lattice already breaks inversion symmetry while the magnetic field breaks time reversal symmetry. In the following, a phenomenological discussion based on symmetry arguments is given on how quadrochroism can arise based on chirality. Details about the Ni_3TO_6 material can be found in Sec. 6.

5.1 Transmission through a chiral medium

The above mentioned case of chiral media can be discussed in presence of a magnetic field. In Faraday geometry, the propagation direction is either parallel or anti-parallel to the direction of the applied field, giving rise to eight possible solutions $n_{\pm}(\pm\mathbf{H}, \pm\mathbf{q})$ where the index \pm of n refers to the helicity of light¹. Taking into account that a chiral slab can be right-handed or left-handed gives two sets $n_{\pm,R}(\pm\mathbf{H}, \pm\mathbf{q})$ and $n_{\pm,L}(\pm\mathbf{H}, \pm\mathbf{q})$. Symmetry arguments [57] can be used to establish relations between groups of 4 of the 16 solutions. The discussion is based on [59].

¹Note, while n_{\pm} denotes the refractive index for the two helicities, $\pm\mathbf{H}$ is the applied magnetic field and $\pm\mathbf{q}$ denotes opposite traveling directions according to a fixed coordinate system.

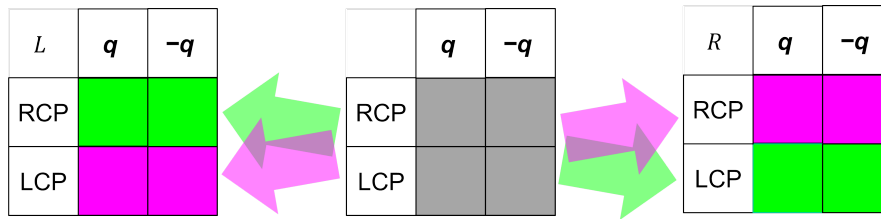


Figure 5.1: Switching on chirality. A non-chiral sample has the same response (grey) independent of direction and polarization. Decomposed into the two chiral enantiomers L and R , a difference in the refractive index for LCP and RCP light can be seen.

5.1.1 Quadrochromism

A way of explaining how quadrochromism is manifested is illustrating two different types of dichroism which are brought together. A dichroic material shows two different responses (colors) depending on polarization, field direction or propagation direction. Figure 5.1 shows a non dichroic material which looks grey from all sides and with all polarizations. Imagine the decomposition of this material into two chiral enantiomers would create a right-handed (R) and a left-handed (L) chiral slab. A wave propagating along \mathbf{q} probing the R sample sees a different refractive index whether it is RCP (magenta) or LCP (green). Inverting the direction of propagation to $-\mathbf{q}$ leaves this unchanged.

The enantiomer of a right-handed slab (R), a left-handed slab (L), can be created by inversion. Since RCP and LCP are as well connected via inversion, probing with LCP (RCP) on L leads to the same result as probing R with RCP (LCP), colored magenta (green).

For a non-chiral material in an external field \mathbf{H} , a difference of the refractive index n_{\pm} for a RCP wave and a LCP wave is equivalent to a magneto-optical response such as for instance the Faraday effect. The magnetic field breaks time reversal symmetry, so changing the propagation direction of an RCP (LCP) wave from \mathbf{q} to $-\mathbf{q}$, while leaving the field unchanged, reverses the response, see Fig. 5.2, 2).

Inverting the initially applied direction of the magnetic field to $-\mathbf{H}$ inverts the response for a RCP (LCP) wave propagating along \mathbf{q} . Now $-\mathbf{q}$ is parallel to $-\mathbf{H}$, what makes it indistinguishable from \mathbf{H} parallel to \mathbf{q} .²

Bringing a chiral material into a magnetic field leads to the possibility of combine the four times four responses depicted in Fig. 5.2, 1) and Fig. 5.2, 2) , giving rise to total 16 combinations , see Fig. 5.2, 3). Instead of separately explaining them, we focus on the discussion of symmetry that connects different combinations in Fig. 5.2, 3).

²Note that the two colors magenta and green in the case 1a) and 1b) are in general not the same as for the case 2a) and 2b), so far they just represent similarities in the response to either a RCP or LCP wave in two different media.

		1)					
		R			L		
		\mathbf{q}	$-\mathbf{q}$	\mathbf{q}	$-\mathbf{q}$		
		RCP			RCP		
		LCP			LCP		
2)		3)					
\mathbf{H}		\mathbf{H}, R			\mathbf{H}, L		
\mathbf{q}		\mathbf{q}	$-\mathbf{q}$	\mathbf{q}	$-\mathbf{q}$		
$-\mathbf{q}$		$-\mathbf{q}$	\mathbf{q}	$-\mathbf{q}$	\mathbf{q}		
		RCP			RCP		
		LCP			LCP		
$-\mathbf{H}$		$-\mathbf{H}, R$			$-\mathbf{H}, L$		
\mathbf{q}		\mathbf{q}	$-\mathbf{q}$	\mathbf{q}	$-\mathbf{q}$		
$-\mathbf{q}$		$-\mathbf{q}$	\mathbf{q}	$-\mathbf{q}$	\mathbf{q}		
		RCP			RCP		
		LCP			LCP		

Figure 5.2: Schematic overview on configurations for measuring with RCP and LCP waves traveling along positive (\mathbf{q}) and negative ($-\mathbf{q}$) x direction. A chiral medium (R , L) without external field, see 1). Magneto-optical response such as for instance the Faraday effect for magnetic field \mathbf{H} applied in positive and negative x direction, see 2). Chiral medium in external field, see 3).

Therefore we depict a slab with chirality R in an external field \mathbf{H} which is parallel to the direction of propagation \mathbf{q} of a RCP wave, see Fig. 5.3 a). We see that the response of the material to the light can be denoted as $n_{+,R}(\mathbf{H},\mathbf{q})$. Now, we invert the time in the universe, see Fig. 5.3 c). The chirality R is unchanged whereas the magnetic field direction inverts. The electric field vector now moves backwards on the same curve, which on the first glance could result in a negative helicity. But it also inverts the propagation direction, keeping the helicity intact due to the definition given in Sec. 2. This leads to the following combination $n_{+,R}(-\mathbf{H},-\mathbf{q})$ which is connected to $n_{+,R}(\mathbf{H},\mathbf{q})$ via time-reversal symmetry.

Now, for inverting the universe, see Fig. 5.3 b), the magnetic field direction remains unchanged. The chirality R transforms into its enantiomer L , the helicity changes to LCP, and the propagation direction is inverted. The corresponding refractive index is $n_{-,L}(\mathbf{H},-\mathbf{q})$. Applying time-reversal after inversion leads to the same result as inverting after reversing the time, $n_{-,L}(-\mathbf{H},\mathbf{q})$, see Fig. 5.3 d).

These conversion laws, explaining the connection between the magenta colored cases in Fig. 5.2, 3) can similarly be applied to the three differently colored cases green, yellow, and blue.

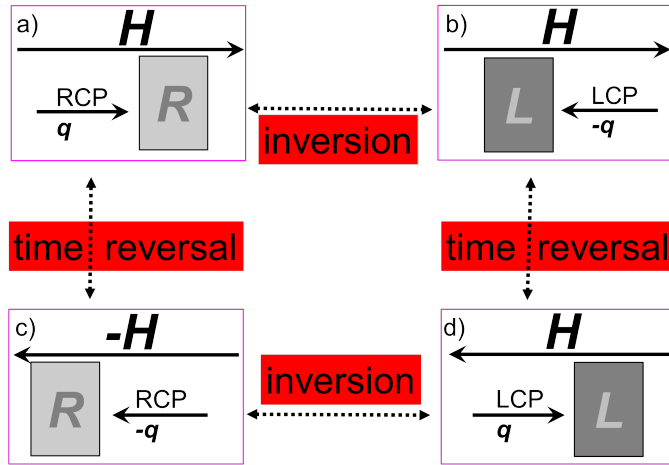


Figure 5.3: Connection between different configurations of helicity of light (RCP or LCP) and propagation direction ($\pm\mathbf{q}$), positive and negative magnetic field direction ($\pm\mathbf{H}$), and both enantiomers R and L via inversion and time-reversal symmetry.

5.1.2 Discussion

It is possible to extract all four distinguishable responses for either measuring with only one helicity of light (RCP or LCP) on both enantiomers, or measuring on only one single domain (R or L) with both helicities of light.

Table 5.1: Probing configurations for a chiral material in magnetic field

RCP	LCP	R	L
$n_{+,R}(\mathbf{H},\mathbf{q})$	$n_{-,L}(\mathbf{H},-\mathbf{q})$	$n_{+,R}(-\mathbf{H},-\mathbf{q})$	$n_{-,L}(-\mathbf{H},\mathbf{q})$
$n_{+,R}(\mathbf{H},-\mathbf{q})$	$n_{-,L}(\mathbf{H},\mathbf{q})$	$n_{+,R}(-\mathbf{H},\mathbf{q})$	$n_{-,L}(-\mathbf{H},-\mathbf{q})$
$n_{+,L}(\mathbf{H},\mathbf{q})$	$n_{-,R}(\mathbf{H},-\mathbf{q})$	$n_{-,R}(-\mathbf{H},\mathbf{q})$	$n_{+,L}(-\mathbf{H},-\mathbf{q})$
$n_{+,L}(\mathbf{H},-\mathbf{q})$	$n_{-,R}(\mathbf{H},\mathbf{q})$	$n_{-,R}(-\mathbf{H},-\mathbf{q})$	$n_{+,L}(-\mathbf{H},\mathbf{q})$

All possible refractive indices are sorted in table 5.1. In a row, the four entries are indistinguishable according to Fig. 5.3. The four rows correspond to the colors magenta, yellow, green and blue (Fig. 5.2, 3)) from 1 to 4 in that order, whereas the columns are sorted by the different probing configurations. This gives an overview on how to measure a sample with the most easily accessible parameters. It is not possible to measure all responses with only one helicity of the material and only one helicity of light. The correlation for the absorption of a simple excitation can also be displayed in the following way (see Fig. 5.4). Consider an excitation at frequency ω_0 in zero field which shows absorption of different strength for left- and right-handed light (green, magenta), respectively, in either an R or L sample. In finite field, those excitations split up, giving rise to different absorption strengths for circularly polarized light depending on the direction, as already discussed. In this picture, a finite effect also in unpolarized light depending on the direction

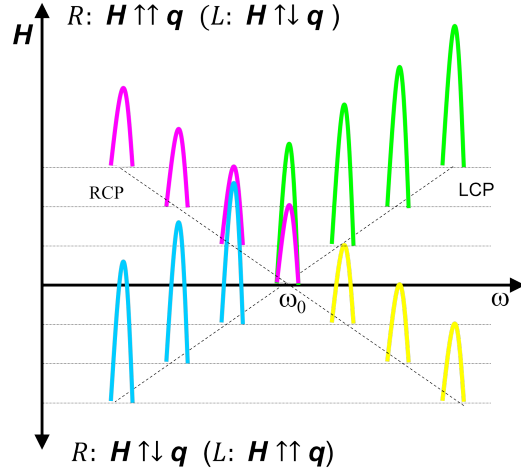


Figure 5.4: Sketch of the chiral medium in finite magnetic field with two different absorption strengths for RCP and LCP light already at zero magnetic field for L and R enantiomer.

can easily be understood. Unpolarized light is usually described as light with all possible linear polarization directions at once. Each of these linear components can be decomposed into a RCP and LCP wave with a certain phase difference, so that an equivalent description can be that of equal amounts of RC and LC polarized waves with all possible phases. Upon passing through the R (L) sample with $\mathbf{H} \uparrow \uparrow \mathbf{q}$ ($\mathbf{H} \uparrow \downarrow \mathbf{q}$), for example the right-handed (left-handed) part at lower frequencies experiences a lower absorption than the left-handed (right-handed) part at the same frequency upon inverting the propagation direction, leading to a different absorption for unpolarized light.

5.2 Transmission through chiral matter on normal incidence in presence of a magnetic field

Chirality may arise in the optical properties due to off-diagonal elements of the $\hat{\epsilon}$ tensor or due to the dynamical magneto electric coupling described by $\hat{\chi}^{me}$ and $\hat{\chi}^{em}$. Therefore we start from the most general version of the linear constitutive relations,

$$\mathbf{D}(\omega) = \epsilon_0 \hat{\epsilon} \mathbf{E} + \sqrt{\epsilon_0 \mu_0} \hat{\chi}^{em} \mathbf{H} \quad (5.2)$$

$$\mathbf{B}(\omega) = \mu_0 \hat{\mu} \mathbf{H} + \sqrt{\epsilon_0 \mu_0} \hat{\chi}^{me} \mathbf{E} \quad . \quad (5.3)$$

Using $\mathbf{B} = \mu_0(\mathbf{H} + \mathbf{M})$ and $\mathbf{E} = 1/\epsilon_0(\mathbf{D} - \mathbf{P})$ we find the polarization \mathbf{P} and magnetization \mathbf{M}

$$\mathbf{P}(\omega) = \epsilon_0(\hat{\epsilon} - 1)\mathbf{E} + \sqrt{\epsilon_0 \mu_0} \hat{\chi}^{em} \mathbf{H} \quad (5.4)$$

$$\mathbf{M}(\omega) = \mu_0(\hat{\mu} - 1)\mathbf{H} + \sqrt{\epsilon_0/\mu_0} \hat{\chi}^{me} \mathbf{E} \quad . \quad (5.5)$$

The oscillating electric and magnetic fields induce consequently oscillating magnetization \mathbf{M} and polarization \mathbf{P} . The components of the tensors can be expressed by the Kubo formula [60]:

$$\epsilon_{ij} = \epsilon_i^\infty \delta_{ij} + \frac{2}{V\hbar\epsilon_0} \sum_n \frac{\omega_{0,n} \Re(D_{j,n}^{e*} D_{i,n}^e) + i\omega \Im(D_{j,n}^{e*} D_{i,n}^e)}{\omega_{0,n}^2 - \omega^2 - i\gamma_n\omega} \quad (5.6)$$

$$\mu_{ij} = \mu_i^\infty \delta_{ij} + \frac{2\mu_0}{V\hbar} \sum_n \frac{\omega_{0,n} \Re(D_{j,n}^{m*} D_{i,n}^m) + i\omega \Im(D_{j,n}^{m*} D_{i,n}^m)}{\omega_{0,n}^2 - \omega^2 - i\gamma_n\omega} \quad (5.7)$$

where V is the volume of system³, the index n counts over all excited states with energy $\omega_{0,n}$ and damping γ_n , $D_{i,n}^m$ and $D_{i,n}^e$ denote the i -th components of the electric and magnetic dipole matrix elements for an excitation from ground state $|0\rangle$ to an excited state $|n\rangle$ at the energy $\omega_{0,n}$

$$D_{i,n}^e = \langle n | p_i | 0 \rangle, \quad D_{i,n}^m = \langle n | m_i | 0 \rangle, \quad (5.8)$$

where p_i and m_i denote the electric and magnetic dipole operators, respectively. It is important to point out that the term for the magneto-electric coupling is only non-zero when $D_{i,n}^m$ and $D_{i,n}^e$ are simultaneously non zero for a given excitation [60],

$$\chi_{ij}^{me} = \frac{2}{V\hbar} \sqrt{\frac{\mu_0}{\epsilon_0}} \sum_n \frac{\omega_{0,n} \Re(D_{j,n}^{m*} D_{i,n}^e) + i\omega \Im(D_{j,n}^{m*} D_{i,n}^e)}{\omega_{0,n}^2 - \omega^2 - i\gamma_n\omega} \quad (5.9)$$

$$\chi_{ij}^{em} = \frac{2}{V\hbar} \sqrt{\frac{\mu_0}{\epsilon_0}} \sum_n \frac{\omega_{0,n} \Re(D_{j,n}^{e*} D_{i,n}^m) + i\omega \Im(D_{j,n}^{e*} D_{i,n}^m)}{\omega_{0,n}^2 - \omega^2 - i\gamma_n\omega}. \quad (5.10)$$

Considering the symmetry properties under time reversal and for ease of notation, we use

$$\epsilon_{ij} = \epsilon_{ij}^\infty + \epsilon'_{ij} + \epsilon''_{ij} \quad (5.11)$$

$$\mu_{ij} = \mu_{ij}^\infty + \mu'_{ij} - \mu''_{ij} \quad (5.12)$$

$$\chi_{ij}^{me} = \chi'_{ij} + \chi''_{ij} \quad (5.13)$$

$$\chi_{ij}^{em} = \chi'_{ji} - \chi''_{ji} \quad (5.14)$$

where the primed (double primed) quantities refer to the terms arising from the real (imaginary) parts of the numerators in Eq. 5.6, 5.7, 5.9 and 5.10. It is very important to point out that these are not the real or imaginary parts of the response function itself. In terms of symmetry, χ'_{ij} is time reversal odd, whereas χ''_{ij} is time

³In case when \mathbf{P} and \mathbf{M} describe polarization and magnetization of a unit cell, V is the volume of the unit cell. When \mathbf{P} or \mathbf{M} describe the total polarization and magnetization of the sample, V is the volume of the sample.

reversal even.

Now we have to focus on the appearance of ϵ , μ and χ in our case of Ni_3TeO_6 . A chiral response can result from ϵ_{xy} or χ^{me} . We first consider $\hat{\epsilon} - 1$ which can be expanded in a power series [61]. For plane waves we write $\nabla \mathbf{E} = i\mathbf{q}\mathbf{E}$. We consider the terms which describe the conventional dielectric response, chirality (in ϵ_{xy} via spatial dispersion), the Faraday effect and magneto-spatial dispersion which is a higher order term of Faraday effect and spatial dispersion [61].

$$P_i(\omega) = \epsilon_0 \left[\chi_{ij} E_j(\omega) + \chi_{ijl} \nabla_l E_j(\omega) + \chi'_{ijl} E_j(\omega) H_l^{DC} + \chi_{ijkl} \nabla_l E_j(\omega) H_k^{DC} \right] + \sqrt{\epsilon_0 \mu_0} \hat{\chi}^{me} H . \quad (5.15)$$

We thus find

$$\epsilon_{ij}(\omega, \mathbf{q}, \mathbf{H}^{DC}) = \epsilon_{ij}^0(\omega) + i\hat{\epsilon}_{ijm}(f_{ml} H_l^{DC} + g_{ml} q_l) + h_{ijlm} H_l^{DC} q_m \quad (5.16)$$

where⁴ $\chi_{ij} = \epsilon_{ij}^0 - 1\delta_{ij}$, $\hat{\epsilon}_{ijm}$ describes the antisymmetric Levi Civitas tensor, \hat{f} is a symmetric tensor of rank 2, \hat{g} is an axial (pseudo-)tensor of rank 2, and \hat{h} is a pseudotensor of rank 4 where $h_{ijlm} = h_{jilm}$ [61]. Considering time reversal symmetry we have

$$\epsilon_{ij}(\omega, \mathbf{q}, \mathbf{H}^{DC}) = \epsilon_{ij}(\omega, -\mathbf{q}, -\mathbf{H}^{DC}) . \quad (5.17)$$

Due to time reversal symmetry we can explicitly write the tensors as

$$\hat{\epsilon}^0 = \begin{bmatrix} \epsilon_{xx}^0 & 0 & 0 \\ 0 & \epsilon_{xx}^0 & 0 \\ 0 & 0 & \epsilon_{zz}^0 \end{bmatrix}, \quad \hat{f} = \begin{bmatrix} f_{xx} & 0 & 0 \\ 0 & f_{xx} & 0 \\ 0 & 0 & f_{zz} \end{bmatrix}, \quad \text{and} \quad \hat{g} = \begin{bmatrix} g_{xx} & 0 & 0 \\ 0 & g_{xx} & 0 \\ 0 & 0 & g_{zz} \end{bmatrix} . \quad (5.18)$$

In Faraday configuration for $\mathbf{H}^{DC} \parallel \mathbf{q}$, only the coefficients $h_{1133} = h_{2233} = h$ and $h_{3333} = h_3$ are non zero for uniaxial crystals having pure rotation axis only [61]. For propagation direction $\mathbf{q} = (0, 0, q)$ and static external field $\mathbf{H}^{DC} = (0, 0, H)$ we get

$$\hat{\epsilon} = \begin{bmatrix} \epsilon_{xx}^0 + hH^{DC}q & +i(f_{zz}H^{DC} + g_{zz}q) & 0 \\ -i(f_{zz}H^{DC} + g_{zz}q) & \epsilon_{xx}^0 + hH^{DC}q & 0 \\ 0 & 0 & \epsilon_{zz}^0 + h_3H^{DC}q \end{bmatrix} . \quad (5.19)$$

The two off-diagonal terms proportional to H^{DC} or q refer to the Faraday effect and spatial dispersion. The combination of the two gives rise to a higher-order term proportional to $H^{DC} q$ in the diagonal elements. This is one possibility

⁴Here, χ refers to the dielectric susceptibility which has to be distinguished from the magneto-optical response χ^{em} .

to realize magneto-chiral dichroism. In the present case of Ni_3TeO_6 , the space group in the paramagnetic phase is $R3$ [62], the material is chiral and polar [3]. In the antiferromagnetic state, ordered moments are collinear [4]. Due to the collinearity, we may stick to the ordinary magnetic space groups (combining the crystallographic space group with the time reversal operator). For $R3$, there are three different possibilities: $R3$ (white), $R31$ (grey) and R_R3 in Litvin notation. The first one, $R3$, requires ferromagnetic order (white), while the second refers to a paramagnetic state (grey). Accordingly, R_R3 (No. 1242 or 146.3.1242) is the correct magnetic space group. It refers to a black-white centered cell. The corresponding point group is $31'$. Therefore, Eq. 5.19 describes the allowed form of $\hat{\epsilon}$ in Ni_3TeO_6 .

Spatial dispersion is often considered in the visible range, even though $\lambda \gg c$ applies also there. But compared to the visible, λ is about 3 orders of magnitude larger in the THz range. Therefore we neglect terms linear in q in Eq. 5.19

$$\hat{\epsilon} = \begin{bmatrix} \epsilon_{xx}^0 & +if_{zz}hH^{DC} & 0 \\ -if_{zz}hH^{DC} & \epsilon_{xx}^0 & 0 \\ 0 & 0 & \epsilon_{zz}^0 \end{bmatrix}. \quad (5.20)$$

Additionally, in Ni_3TeO_6 , the magnetization is very small for $\mathbf{H}^{DC} \parallel c$ for fields up to 7 T, [63]. This suggests that the Faraday effect is small. Indeed our data show only a negligible effect of H^{DC} for frequencies not too close to the magnon resonances. We therefore neglect also the Faraday effect. The ϵ_{xy} and ϵ_{yx} components are 0 and $\hat{\epsilon}$ is diagonal. Following the same argumentation, $\hat{\mu}$ is diagonal, too. χ_{ij}^{me} and χ_{ij}^{em} are related by the Kubo formula [64] according to

$$\chi_{ij}^{me} = \chi'_{ij} + \chi''_{ij} \quad (5.21)$$

$$\chi_{ij}^{em} = \chi'_{ji} - \chi''_{ji}. \quad (5.22)$$

In zero magnetic field, only the time reversal even terms are allowed, leaving us with the following tensors:

$$\hat{\epsilon} = \begin{bmatrix} \epsilon'_{xx} & 0 & 0 \\ 0 & \epsilon'_{xx} & 0 \\ 0 & 0 & \epsilon'_{zz} \end{bmatrix}, \quad \hat{\mu} = \begin{bmatrix} \mu'_{xx} & 0 & 0 \\ 0 & \mu'_{xx} & 0 \\ 0 & 0 & \mu'_{zz} \end{bmatrix} \quad (5.23)$$

$$\hat{\chi}^{me} = \begin{bmatrix} \chi''_{xx} & \chi''_{xy} & 0 \\ -\chi''_{xy} & \chi''_{xx} & 0 \\ 0 & 0 & \chi''_{zz} \end{bmatrix}, \quad \text{and} \quad \hat{\chi}^{em} = \begin{bmatrix} -\chi''_{xx} & \chi''_{xy} & 0 \\ -\chi''_{xy} & -\chi''_{xx} & 0 \\ 0 & 0 & -\chi''_{zz} \end{bmatrix}. \quad (5.24)$$

With a plane wave propagating along z , the Maxwell equations are in the form

$$\begin{pmatrix} D_x \\ D_y \end{pmatrix} = \epsilon_0 \epsilon'_{xx} \begin{pmatrix} E_x \\ E_y \end{pmatrix} + \sqrt{\epsilon_0 \mu_0} \begin{pmatrix} \chi''_{xx} & \chi''_{xy} \\ -\chi''_{xy} & \chi''_{xx} \end{pmatrix} \begin{pmatrix} H_x \\ H_y \end{pmatrix}, \quad (5.25)$$

$$\begin{pmatrix} B_x \\ B_y \end{pmatrix} = \sqrt{\epsilon_0 \mu_0} \begin{pmatrix} -\chi''_{xx} & \chi''_{xy} \\ -\chi''_{xy} & -\chi''_{xx} \end{pmatrix} \begin{pmatrix} E_x \\ E_y \end{pmatrix} + \mu_0 \mu'_{xx} \begin{pmatrix} H_x \\ H_y \end{pmatrix} \quad (5.26)$$

Solving these, one gets the two refractive indices which correspond to the two circularly polarized states

$$N_{\pm} = \sqrt{\epsilon'_{xx} \mu'_{xx} + \chi''_{xy}{}^2} \mp i \chi''_{xx} \quad (5.27)$$

With Eq. 5.6, 5.7 and Eq. 5.10, 5.9 we get

$$\begin{aligned} \epsilon'_{xx} &= \epsilon_{xx}^{\infty} + \frac{\omega_p^2}{\omega_0^2 - \omega^2 - i\gamma\omega} \\ \mu'_{xx} &= \mu_{xx}^{\infty} + \frac{\omega_m^2}{\omega_0^2 - \omega^2 - i\gamma\omega} \end{aligned} \quad (5.28)$$

$$\chi''_{xx} = i \frac{\omega \omega_{xx}}{\omega_0^2 - \omega^2 - i\gamma\omega} \quad (5.29)$$

$$\chi''_{xy} = i \frac{\omega \omega_{xy}}{\omega_0^2 - \omega^2 - i\gamma\omega} \quad (5.30)$$

Here, ω_0 is the frequency position of the excitation, γ the damping, ω_p and ω_m the strength in ϵ and μ respectively, and ω_{xx} and ω_{xy} the strength of χ_{xx} , and χ_{xy} respectively. Circular birefringence in the THz range is possible if a chiral excitation at high energy causes a difference between n_+ and n_- at low energy as well. In zero magnetic field and for THz frequencies, circular dichroism in this system can only arise from χ^{me} . In the most simple picture, adding a field dependent Zeeman splitting of the mode is already enough to create quadrochromism in finite magnetic field. In private communication, Achim Rosch gave the constraint that $D_x^m = c_0 \rightarrow D_y^m = ic_0$ with c_0 real. From this follows finally

$$\omega_{xx}^2 + \omega_{xy}^2 = \omega_m^2 \omega_p^2 / \omega_0^2. \quad (5.31)$$

We will use this correlation for the analysis of our data in Chap. 8

5.3 Transmission through chiral matter upon normal incidence

This part is based on the description from J. Lekner [65]. The transmittance T corresponds to the intensity that comes out behind the sample, while t corresponds

to the amplitude of the rays including those which were multiply reflected within the sample. The index $+/-$ of t_+ and t_- refers to incoming light with positive (negative) helicity, the second index describes the helicity of light that is observed behind the sample. This leaves in total 4 possible combinations t_{++} , t_{--} , t_{-+} , and t_{+-} . For normal incidence on a chiral slab, mixing of the two chiral polarization states while transmitting is forbidden. The transmission coefficient for converting light of negative helicity to positive helicity, and vice versa, are $t_{-+} = t_{+-} = 0$. The transmission coefficients for both helicities are given by

$$t_{++} = \frac{(1+r) \cdot (1+r')Q_+}{1 - rr'Q_+Q_-} \quad (5.32)$$

$$t_{--} = \frac{(1+r) \cdot (1+r')Q_-}{1 - rr'Q_+Q_-} \quad (5.33)$$

where Q_{\pm} are the phase factors for positive and negative helicities

$$Q_{\pm} = e^{iN_{\pm}d\omega/c} \quad (5.34)$$

where $N_{\pm} = n_{\pm} + ik_{\pm}$ are the complex refractive indices for the two helicities. In the case of Ni_3TeO_6 , they were derived in Sec. 5.2. The coefficients r and r' are the normal-incidence reflection amplitudes at the two interfaces of the chiral slab, respectively:

$$r = \frac{1-m}{1+m}, \quad r' = \frac{m'-1}{1+m'}. \quad (5.35)$$

At normal incidence, the components of the magnetoelectric tensor do not appear in the reflectivity, compare supplement of [60]. For a free-standing slab, both interfaces are the same ($m = m' = 1/Z$) with $Z = \sqrt{\mu_0\mu/\epsilon_0\epsilon}$ as the wave impedance what yields $r = r'$. This gives

$$t_{++} = \frac{(1+r)^2Q_+}{1 - r^2Q_+Q_-} \quad (5.36)$$

$$t_{--} = \frac{(1+r)^2Q_-}{1 - r^2Q_+Q_-} \quad (5.37)$$

with $r = \frac{Z-1}{Z+1}$. For $N_+ = N_-$ one finds $Q_+ = Q_-$ and thus the same transmittance coefficient $t_{++} = t_{--}$. If n is real (no absorption), in a chiral medium with a finite difference between n_+ and n_- , the ratio

$$\frac{t_{++}}{t_{--}} = \frac{Q_+}{Q_-} = e^{i(n_+-n_-)\omega d/c} \quad (5.38)$$

reveals a phase difference which corresponds to a finite optical path length difference $(n_+ - n_-)d = \Delta nd$ between light with opposite helicities. Measuring the

phase for opposite helicities is the most direct way to access this quantity. Usually the chirality parameter γ given by

$$(n_+ - n_-)d = 2\gamma d \tag{5.39}$$

is used to describe this asymmetry. The rotation of the polarization plane by the angle θ for linearly polarized light caused by natural activity can be described as $\Theta = \frac{\omega d}{c}\gamma = \frac{\omega d}{c}\frac{\Delta n}{2}$. Usually this is a rather small effect of the order of 10^{-3} or less. Very important to point out is that, for linearly polarized light, multiple reflections in the sample have no effect on the rotation θ . The phase of the RCP and LCP part of linearly polarized light changes equally for each further passing through the sample. Upon reflection at the surfaces RCP and LCP light change helicities and both travel the path $(n_+ + n_-)d$ upon passing through the sample again. The intensity of the transmitted light changes for multiple reflections since the absorption on each passage adds up. But for one single helicity, multiple reflections affect the phase.

6 Material properties of Ni_3TeO_6

The material properties of Ni_3TeO_6 are presented in this chapter. A summary of the crystallographic properties of this compound based on literature will be presented, as well as the current understanding of the magnetic structure and results of recent spectroscopic measurements.

6.1 Crystal structure

First reports on the crystal structure were given by Zupan, Kolar, and Urbanc in 1971 [66], as well as Blasse and Hordjik in 1972 [67]. It was reinvestigated by Becker *et al.* in 2006 [68]. Ni_3TeO_6 crystallizes in $R\bar{3}$ space group. The structure, see Fig. 6.1 a), is based on the corundum structure (Al_2O_3) with Ni and Te at the Al positions in an ordered fashion. The valence of the three Ni ions on all three Ni sites is +2. Electron configuration is $3d^8$ with $S=1$. The oxygen octahedra surrounding the Ni and Te ions are distorted, leading to three inequivalent Ni sites: $\text{Ni}_{(i)}$, $\text{Ni}_{(ii)}$, and $\text{Ni}_{(iii)}$. Edge-sharing $\text{Ni}_{(iii)}\text{O}_6$ - TeO_6 octahedra form one layer, whereas edge-sharing $\text{Ni}_{(i)}\text{O}_6$ - $\text{Ni}_{(ii)}\text{O}_6$ octahedra form a second layer, see Fig. 6.1

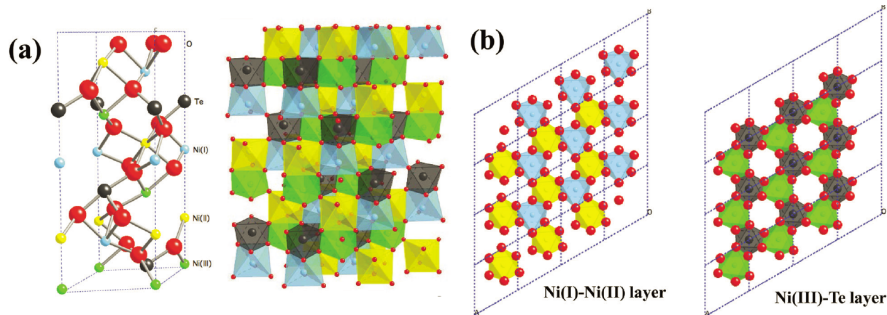


Figure 6.1: (a) Crystal structure of Ni_3TeO_6 in ball-and-stick and polyhedra views showing stacked NiO_6 octahedra with $\text{Ni}_{(i)}$ in blue, $\text{Ni}_{(ii)}$ in yellow, $\text{Ni}_{(iii)}$ in green, and Te in black, (b) $\text{Ni}_{(i)}\text{O}_6$ - $\text{Ni}_{(ii)}\text{O}_6$ and $\text{Ni}_{(iii)}\text{O}_6$ - TeO_6 honeycomb layers are stacked following $R\bar{3}$ symmetry. The red balls correspond to O ions, the honeycomb layer is built from the Ni ions at the center of the drawn octahedra. Figure and caption from Sankar *et al.* [69].

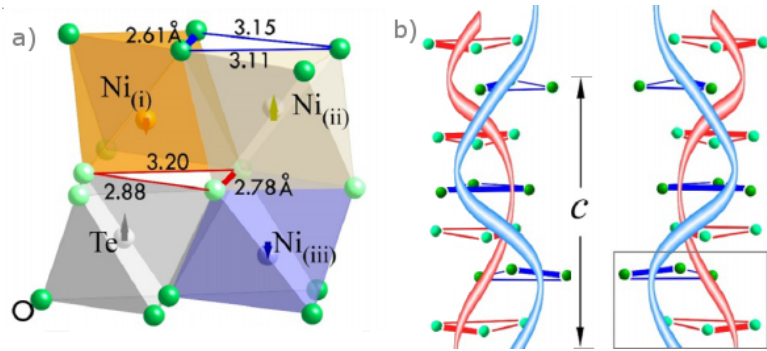


Figure 6.2: A basic building block of Ni_3TeO_6 is shown in (a) which corresponds to $1/3$ of the unit cell. The red triangle is associated with unequal bond lengths which can be considered as part of the first $\text{Ni}_{(iii)}\text{O}_6$ - TeO_6 honeycomb layer. Then, the neighboring $\text{Ni}_{(i)}\text{O}_6$ - $\text{Ni}_{(ii)}\text{O}_6$ layer is associated with the blue triangle with unequal bond lengths. The shortest bonds are marked as bold lines. (b) shows two different ferri-chiral states: left panel with net left-handed chirality and right panel with net right-handed chirality. Red and blue helices, shown by the rotation of the bold red and blue bonds, respectively, rotate in an opposite fashion, and a net chirality exists due to the asymmetry of the red and blue triangles (helices). Figure and caption modified from [3].

a). Each layer individually can be viewed as a honeycomb plane of Ni ions, see Fig. 6.1 b). The two layers are connected via face-sharing $\text{Ni}_{(iii)}\text{O}_6$ - $\text{Ni}_{(ii)}\text{O}_6$ octahedra. One unit consisting of the three different NiO_6 octahedra and a TeO_6 octahedra are the basic building block of the crystal, see Fig. 6.2 [3]. Three building blocks form the unit cell, see left plot in Fig. 6.2 a). They are linked through stacking of TeO_6 and $\text{Ni}_{(i)}\text{O}_6$ octahedra via face-sharing, resulting in a unique 120° rotation of neighboring building blocks (see also supplemental material of [3]).

Due to the distortion of the octahedra, the metal-oxygen bond lengths are unequal for each octahedron, indicated by the red and blue triangles, where the shortest bond is marked bold, see Fig. 6.2 a). Stacking of the building blocks leads to a rotation of the triangles (or shortest bonds) either clockwise (blue bonds) or counterclockwise (red bonds) along the crystallographic c direction, Fig. 6.2 b). This leads to the formation of a left-handed helical structure (red) and a right-handed helical structure (blue), which do not cancel each other due to the different amplitudes of the distortions. Left side of Fig. 6.2 b) shows an overall left-handed chiral state, whereas a net right-handed chiral state is shown on the right side. The colored triangles have opposite sense of rotation with respect to the left side, the two plots thus correspond to the two different domains.

Due to the displacement of the Te and $\text{Ni}_{(ii)}$ ions from the center of the octahedra, a finite polarization exists [3]. This polarization cannot be flipped at room temperature, indicating pyroelectricity. (A possible ferroelectric T_c of 1000 K is reported in [70].) According to the previous considerations of the building blocks,

it was found that the chiral domains and a certain polarization direction are interlocked. The possible domains are either R-,L+ or R+,L-, while only one of the two possible combinations is realized. This makes Ni_3TeO_6 one of the unique materials that exhibits both chirality and polarization at room temperature. The domains can be observed using a polarization microscope. A large optical specific rotation of $\alpha=1355 \text{ deg dm}^{-1} \text{ cm}^3 \text{ g}^{-1}$ in the visible range has been found [3].

6.2 Magnetic structure

First investigations on magnetic properties of Ni_3TeO_6 were performed by Zupan *et al.* [66] using ESR. The g factor was found to be 2.26 on a powder sample.

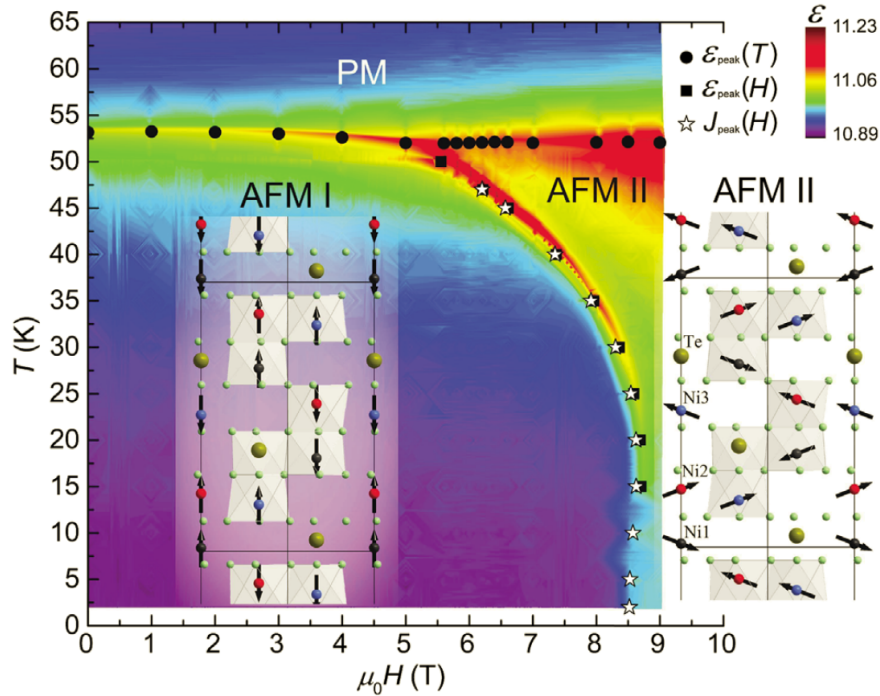


Figure 6.3: Phase diagram of Ni_3TeO_6 determined by variations in the dielectric constant ϵ (color scale at upper right) and magnetoelectric current. Closed circles, closed squares, and open asterisks indicate peak-center positions for $\epsilon(T)$, $\epsilon(H)$, and magnetoelectric current $J(H)$, respectively. These peaks map the boundaries between the paramagnetic (PM) phase and antiferromagnetic phases (AFM I, AFM II). The structure of Ni_3TeO_6 is of the corundum type with a polar $R3$ space group, three inequivalent $S=1$ Ni sites, and significant distortions of oxygen octahedra surrounding Ni ions. The spin configurations in the AFMI and AFMII phases are shown schematically in the insets. Figure and caption modified from [71].

A negative Curie temperature was obtained, indicating that the system is antiferromagnetic. Živković *et al.* [72] investigated magnetization, specific heat, and neutron powder diffraction. A single magnetic transition at $T_N = 52$ K was found, below which the system becomes a collinear antiferromagnet with ferromagnetically ordered ab honeycomb planes. The transition temperature was later found to be 53 K by Yokosuk *et al.* [71] and 55 K by Oh *et al.* [4]. Oh *et al.* observed a spin flop transition for magnetic fields along the c direction at 5 K for 8.83 T (47 K for 6.2 T) [4]. The orientation of the spins mostly lies in the ab plane instead of pointing along the c direction as below the spin-flop transition. Additionally they found that the polarization changes at this transition. A possible explanation is given by the changing $\text{Ni}_{(i)}^{2+} - \text{Ni}_{(ii)}^{2+}$ bond length across the spin flop transition since it depends on the scalar product of the spins. While they are in inequivalent environments, their charges can be slightly different, inducing a dipole moment, which finally results in a change in the polarization when the magnetic state changes in an applied magnetic field [4]. Surprisingly, the magnetoelectric effect (ME) is non-hysteretic, meaning that driving the system over the phase transition by changing the magnetic field is lossless, in contrast to many other materials [4]. The magnetoelectric coupling across the spin-flop transition was also investigated by Yokosuk *et al.* [71] using optical spectroscopy, compare Fig. 6.3. High magnetic field measurements were performed in [63], revealing a first order transition at 52 T for $H \parallel c$, which is second order for $H \perp c$ at 70 T. They point out that Ni_3TeO_6 is not a type-II multiferroic in a sense that magnetic order induces ferroelectricity, but that the magnetic order modifies the already existing electric polarization associated with the polar space group, see chapter 6.1. Furthermore, far infrared, Raman, and time domain THz spectroscopy were performed on Ni_3TeO_6 by Skiadopoulou *et al.* [73] to identify magnons and electromagnons. The lowest phonon mode was found at 185 cm^{-1} in the IR data. The zero-field Raman data show three excitations at 13 cm^{-1} , 35 cm^{-1} , and 206 cm^{-1} at 4 K. The two lower excitations can be seen in Fig. 6.4 bottom panel. The excitation at 13 cm^{-1} broadens towards higher temperatures and the position shifts to roughly 9 cm^{-1} at 40 K. It is not observed at 45 K. The second excitation at 35 cm^{-1} is not observable above 25 K. The THz measurements were performed on Ni_3TeO_6 ceramics because the available single crystals with a maximum diameter of 2 mm were too small for reliable measurements in TD THz spectroscopy. For $H^{DC} \parallel E_{THz}$ and $H^{DC} \perp E_{THz}$, similar features could be observed. Below 48 K a relatively small feature at 16 cm^{-1} and a broad feature at $\approx 32 \text{ cm}^{-1}$ were observed. The lower feature sharpens at 10 K (the other one does not change noticeably) and increases in strength for an applied magnetic field. Only one field direction is shown and the position of the excitation shifts towards 12 cm^{-1} for 7 T both at 25 K and 10 K. The three excitations at 13 cm^{-1} , 35 cm^{-1} , and 206 cm^{-1} at 4 K are stated to be electromagnons [74]. The claim is, that from the knowledge of the E symmetry of the electromagnons due to the Raman results, they must be IR active for $E \perp c$. Since

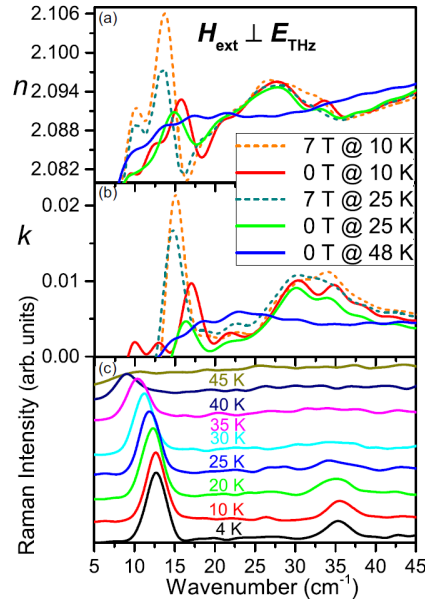


Figure 6.4: Temperature dependence of (a) real and (b) imaginary part of index of refraction, as obtained by THz measurements at $H^{DC} \perp E_{\text{THz}}$ for the Ni_3TeO_6 ceramics. Two excitations appear below 48 K, close to $T_N \approx 53$ K. Upon application of H^{DC} up to 7 T, softening of the lowest frequency mode is observed. For comparison with our results on a single crystal, see Fig. 8.14 and Fig. 8.15. (c) Temperature evolution of the $z(xy)\bar{z}$ Raman spectra of the Ni_3TeO_6 single crystal below 45 K. Figure and caption partly from [73].

the spontaneous polarization, as already discussed in Sec. 6.1, points along the c direction, the spins become electrically active due to dynamic fluctuations out of the c direction, which can be induced due to the same exchange striction mechanism as the static polarization [73]. Unfortunately there is no statement whether a single type of domains was used to produce the ceramics and it obviously does not allow to disentangle contributions along the crystallographic c direction and perpendicular to it. A measurement configuration with $E_{\text{THz}} \perp c$ ($\mathbf{k} \parallel c$) might give information about natural optical activity which can lead to quadrochroism based on magneto chiral dichroism with applying an external field parallel or antiparallel to c direction [58, 75, 76]. On the other hand, a configuration with $\mathbf{k} \perp c$, $E_{\text{THz}} \parallel c$, applying an external magnetic field parallel or antiparallel to the direction of light propagation can lead to an effect based on the toroidal moment [60, 77].

Retuerto *et al.* measured a ceramic of the closely related $\text{Ni}_2\text{MnTeO}_6$ [78] which has a higher antiferromagnetic transition temperature of $T_N=67$ K (see also Mathieu *et al.* [79]). They found a magnetic field tunable spin excitation at ≈ 8 cm⁻¹ in their THz spectra.

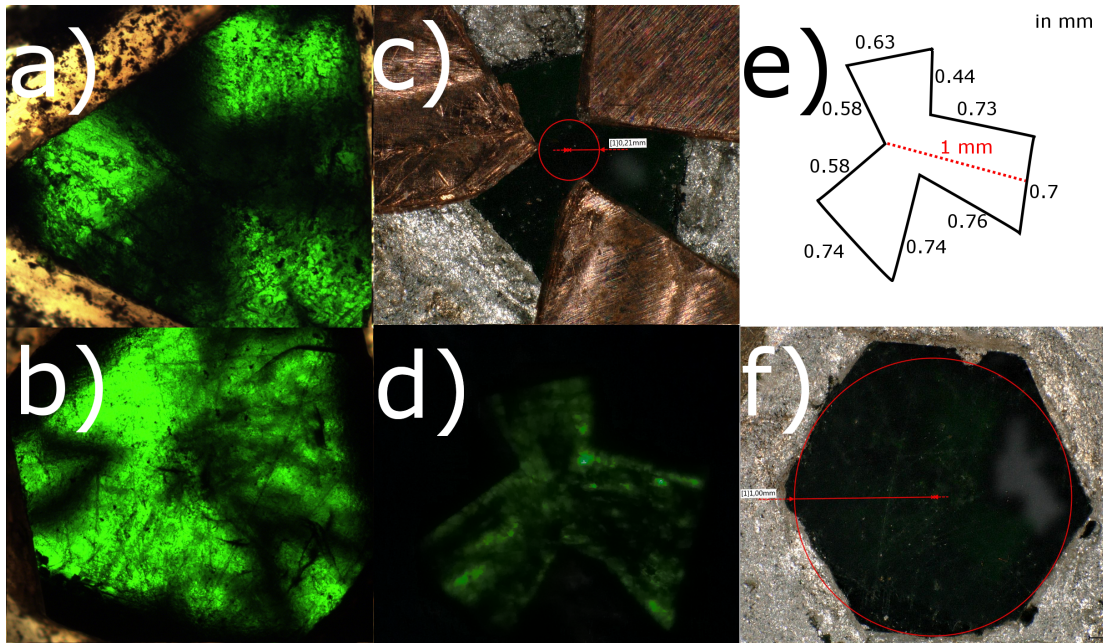


Figure 6.5: Pictures of Ni_3TeO_6 sample from a Leitz Ortholux-Pol microscope (a,b), a modified Leitz microscope (c,d,f), and a Keyence VHX 6000 microscope (e,h). a) shows the radiation-sign-like domain structure from the top side while b) shows the best possible extinction of the other domains from the bottom side. c) The experimental coverage of one domain type and a red circle with 0.21 mm radius in the center (top side). d) The remaining visible crystal with the polarization microscope (top side). Illumination from above was switched off for better contrast. f) Uncovered bottom side with a red circle with 1 mm radius. Note that, due to different microscopes and different amplifications, the size is not exactly the same through the different series. For size reference, use c), d), and f) only.

6.3 Sample

The sample measured in this study has a difficult geometry¹. One side has the shape of a hexagon with an approximate radius of 1 mm, set as bottom side, whereas the other side is shaped more like a triangle with side length of roughly 1.8 mm to 2.1 mm, set as top side. The thickness of the sample was determined to $1.06 \text{ mm} \pm 0.01 \text{ mm}$. The crystal consists of several domains, polarization microscope images were made to investigate the domain distribution.

Figure 6.5 a) shows the radiation sign like pattern found with the same sample

¹The Ni_3TeO_6 sample was grown in the group of S.-W. Cheong, Rutgers Center for Emergent Materials and Department of Physics and Astronomy in Piscataway, USA. The group of I. Kézsmárki in Augsburg, Germany, had the sample for first measurements with time-domain THz spectroscopy, performed by D. Szaller.

reported by Wang *et al.* [3]. The two different domains are clearly distinguishable as brighter and darker areas².

By changing the analyzer angle compared to a), the dark arrows in the corners in the sample while the center gets almost homogeneously brighter. A picture of the orientation of the analyzer for minimal transmission in the other domain type can be seen in b). Further rotation leads to three bright triangles in the corners and the extinction in only a small part at the edges of the sample. This already reveals that the brighter domains from a) are not completely homogeneous. The assumption is that in these areas, there are both domains slightly wedge-shaped on top of each other. The crystal surfaces are plane parallel and do not explain such a behavior for a single domain. A focus point chosen halfway through the sample reveals that inside the crystal cracks and disruptions especially in the center and lower right corner exist. Except of some very small scratches and wells, the surfaces polished flat.

c) shows the covering of the brighter domains with copper plates, the edging was renewed after polishing, using silver paint. The visible sample area is approximately 0.91 mm^2 .

Figure d) was taken with a different contrast and exposure time due to the different setup compared to a). The brighter domains are mostly covered by the copper plates, but some inhomogeneities remain in the other parts. The correspondence of the remaining brighter areas could be crystal defects, indicating that these are parts of the same domain just with another thickness wherefore the extinction would occur for other angles than for the rest of the domains³.

An idea of the dimensions of the visible part of the covered crystal is given in e), whereas f) shows the uncovered backside of the crystal. The sample as it can be seen in a) is referred to as multi-domain sample, whereas the sample partially covered with copper (c) is referred to as single-domain sample. Both have the same backside, see f).

²Pictures 6.5 a) and b) were made using a Leitz Ortholux-Pol microscope in the *Institut für Geologie und Mineralogie* in Cologne. Picture d) was taken using a modified Leitz polarization microscope from the *Institute of physics II.* and an external camera, pictures e) and h) stem from a Keyence VHX 6000, also located in the *Institute of physics II. in Cologne*

³Compare also left side in picture b).

7 How to measure very small samples with irregular shape?

If the sample size is of the order of the wavelength of the light, diffraction effects are not negligible. The commercially available Lake Shore 8500 Series THz System indicates the appropriate sample size with 10 mm by 10 mm [80] for a frequency range starting from 200 GHz.

The domains to be investigated cover approximately 0.91 mm^2 . This particular sample has a very irregular shape due to the arrangement of the domains. Using a circular aperture on the sample would reduce the measurable area to 0.13 mm^2 as can be seen in Fig. 6.5 e).

The first idea was to rebuild an aperture of the exact shape of the sample and use this as a reference. The amount of light which goes through the sample and the reference should be kept the same, such that the signal measured at the detector could lead to a relatively accurate transmission spectrum. This method was used for the measurements on the, with 2.25 mm^2 comparably larger, multidomain sample¹. But still this was difficult to achieve due to the difficult placement and orientation of those tiny apertures at the exact same position in a beam waist which has a diameter of roughly 2 mm or larger over the whole frequency range [16]. Moreover this approach is invalidated by the different diffraction of the beam caused by an empty aperture compared to an aperture filled with a medium. We rather have chosen a large reference aperture ($d=1 \text{ cm}$). The absolute value of $T(\omega)$ is invalidated by diffraction anyway. We will therefore define a transmittance $\tilde{T}(\omega)$ in our case as the transmittance under the influence of diffraction. Still, $\tilde{T}(\omega)$ can be used to identify narrow absorption features. Our quantitative analysis is based on the phase or $\Delta L(\omega)$. The light reaching the detector has the right $\Delta L(\omega)$, even if the intensity is low, since the relative positions of transmitter and receiver do not change.

7.1 Diffraction effects

To describe the relative effect of diffraction on the intensity, a simple model for calculating diffraction for different sizes of empty circular apertures can be used.

¹Note that this number refers to the area of the top side, see Fig. 6.5.

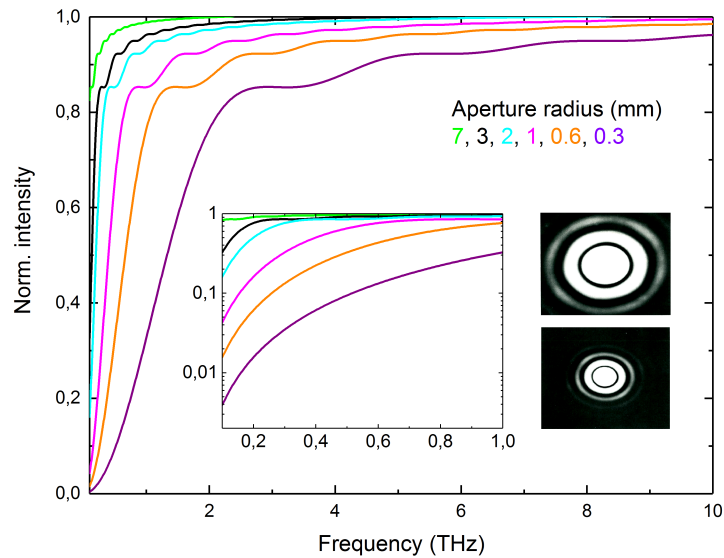


Figure 7.1: Normalized intensity vs. frequency for different aperture sizes integrated on a virtual screen 5 cm behind the aperture in an area with radius of $r=10$ cm. Pictures are from [81], showing Airy rings for an 1 mm and an 0.5 mm aperture.

The phenomenon is for example explained in detail in Optics, Ch. 10 [81]. The angular distribution of the intensity is

$$I_{\Theta} = I_0 \frac{2J_1(ka \sin(\Theta))}{ka \sin(\Theta)} \quad (7.1)$$

where I_0 is the incident intensity, J_1 is the first kind Bessel function of order one, k is the wavenumber and a is the radius of the aperture. For one hole size and one fixed frequency, that results in a angular intensity distribution known as Airy disc pattern, exemplary shown in the upper picture in Fig. 7.1. Increasing the hole size or the frequency of the light leads to less diffraction (lower picture). In a simple approximation we assume a screen 5 cm behind the aperture and integrate over an area A_S with radius 10 cm on the screen. The frequency dependent result, normalized to I_0 , can be seen in Fig. 7.1. For a large reference aperture with a radius of 7 mm, there is a small but negligible effect on the intensity at low frequencies. Upon decreasing the aperture size, oscillations in the power spectrum occur which correspond to the frequency dependent change in the Airy disc pattern in the area A_S . The overall intensity in A_S does change when a white ring (corresponding to a ring with high intensity) leaves the area, but it does not change significantly when a black ring (ring with low intensity) leaves the area.

Inset shows the frequency range between 100 GHz and 1 THz on a logarithmic scale. For apertures with a size below 1 mm, no frequency dependent oscillation

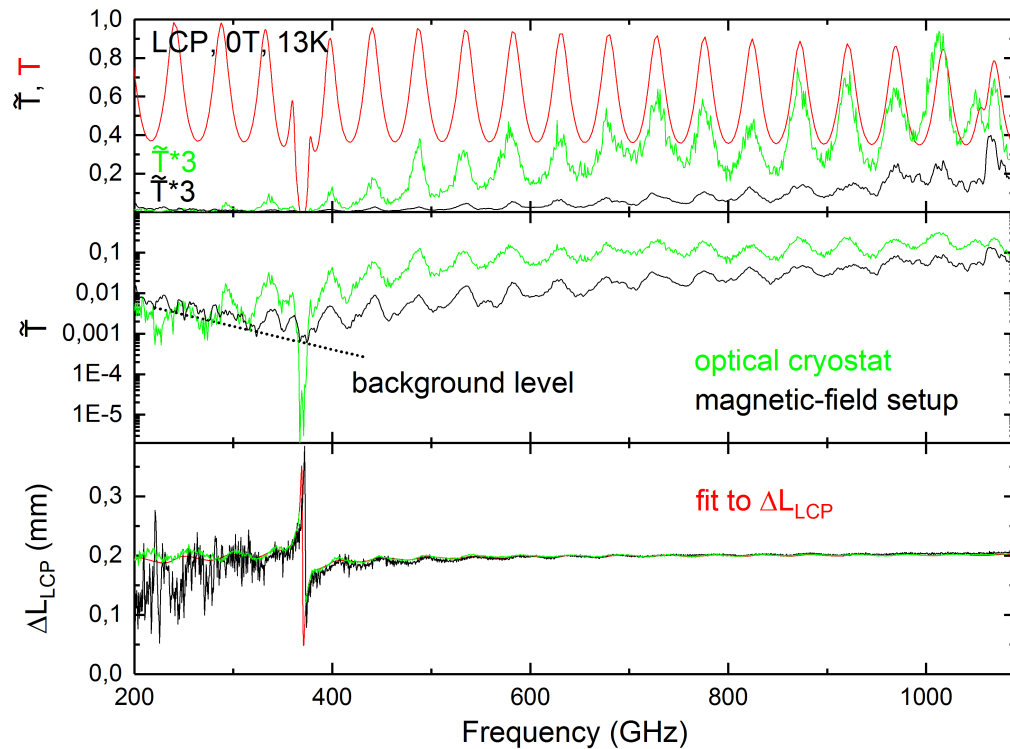


Figure 7.2: Data measured at 13K in an optical cryostat (green) and the magnetic field setup (black). Transmittance $\tilde{T}(\omega)$ multiplied by a factor of 3 on a linear scale (top panel), and a log scale (middle panel) without multiplication factor and the corresponding $\Delta L(\omega)$ (bottom panel). Fit to $\Delta L(\omega)$ and the corresponding Kramers-Kronig consistent transmittance $T(\omega)$ without diffraction (red).

can be seen in the power spectrum below 1 THz. This corresponds to the fact that the bright center maximum of the airy disc covers the whole area A_S over that frequency range. This way, it is not possible to reproduce any effect quantitatively since not only the apertures but also the transmitter and receiver photomixer and in certain circumstances different optics in the beam path have to be considered. But it shows that, below a certain limit, no strong frequency dependencies have to be considered. Between 0.6 mm and 0.3 mm, the decrease at low frequencies is basically a factor corresponding to a dimming of the center maximum.

Figure 7.2 shows $\tilde{T}(\omega)$ multiplied with a factor 3 on a linear scale (upper panel), and log scale as measured (middle panel) and phase data (lower panel) from a measurement in an optical cryostat (green) and in the magnetic field setup (black) at 13 K. The measurements were performed using the same sample and the same reference aperture with radius $r=5$ mm. The large difference in the $\tilde{T}(\omega)$ between the two setups is caused by the focusing lenses used in the setup with the optical

cryostat. The lens directly behind the sample collects a part of the refracted light, leading to a higher signal on the receiver.

In the log-scale plot, the data clearly show the fringes due to multiple reflections within the sample over the whole frequency range from 200 GHz to 1100 GHz. An absorption at 370 GHz decreases $\tilde{T}(\omega)$ to the noise level at $\approx 10^{-5}$. Details about the absorption will be discussed in the next chapter. $\tilde{T}(\omega)$ in the magnetic-field setup is about one order of magnitude lower than in the optical cryostat. Above 300 GHz, both data sets show a similar trend, whereas below 300 GHz, $\tilde{T}(\omega)$ in the magnetic field setup starts to increase again. The reason is that, at low frequencies, the major part of the radiation from the transmitter hits the aperture close to the sample, while only a small amount passes through the sample. Therefore most of the light gets reflected from the aperture. In the closed magnetic field setup, the long wavelengths are reflected within the surrounding vacuum shields and a small part, less than 1% at 200 GHz, reaches the detector. For a larger sample, this is not the case since most of the radiation passes through the sample and only a significantly smaller part gets back-reflected. For this sample, the frequency dependent level of this background signal is indicated by the dotted line. At 370 GHz, the amount of the bypassing light is still 0.05%, leading to the difference in the appearance of the absorption feature which reaches the background level almost immediately.

The strength of the setup is the possibility to measure the phase data at each frequency independent of the amplitude data. In the lower panel, $\Delta L(\omega)$ is compared for both measurements. Despite the very different appearance of the transmittance, $\Delta L(\omega)$ shows almost no difference between the two measurements except of a larger error due to the overall lower intensity at the receiver in case of the magnetic field setup. The shape and size of the excitation at 370 GHz is well reproduced. The black curve has less points close to the excitation because in both curves, the phase data was cut out where the transmittance reaches the background level in the magneto cryostat or the noise level in the optical cryostat. Below 320 GHz, the measured phase in the magnetic-field setup is dominated by the part of the radiation which bypasses the sample, therefore $\Delta L(\omega)$ measured in the magnetic-field setup deviates strongly from $\Delta L(\omega)$ measured in the optical cryostat. A fit to $\Delta L(\omega)$ (red) is used to calculate the Kramers-Kronig consistent transmittance $T(\omega)$ (top panel). For details about the fit, see Sec. 8.1.4. The strong difference between the appearance of $T(\omega)$ from the fit $\Delta L(\omega)$ and the data $\tilde{T}(\omega)$ is obvious.

7.2 Discussion

Optical spectroscopy with wavelengths of the same order of the sample size is difficult. The absolute value of the transmittance can not be determined properly

due to the finite size of the detector. Having a large detector or focusing optics behind the sample helps to increase the relative signal, but it will not accurately reproduce the frequency dependent absolute value over a broad range. The simulation shows that, for low diffraction, a frequency depending modulation of the measured intensity can not be excluded what will affect the transmittance if the reference measurement can not reproduce the exact same frequency dependence. Measuring the phase on the other hand gives us a great tool for investigations on small samples. The phase is determined by the active areas in the photomixers, see Sec. 3.5. Those do not change for sample and reference since the same photomixers are used. Furthermore, the relative position of both photomixers is stays the same. Therefore, the optical path length difference ΔL is accurately determined, even so absolute value of the measured \tilde{T}_ω depends on the diffraction specific to the setup that is used.

8 Measurements on Ni_3TeO_6

In this chapter, we discuss results of measurements on Ni_3TeO_6 . We present data measured with circularly polarized light as well as with linearly polarized light and compare the results at the lowest measured temperature of 3 K. Additionally, the temperature dependence of the data is discussed. The influence of an external magnetic field is investigated with LCP light using the magnetic field setup, see Sec. 8.2. Measurements are made on the single-domain sample and additionally on the multidomain sample, see Sec. 8.4. The findings will be used in combination with a model for a description based on the mathematical description presented in Sec. 5.3 and the description of the refractive index, see Sec. 5.2 to extract optical properties and later to explain phenomena as for example the difference in absorption for unpolarized light upon passing through the sample in opposite directions.

In the following, we will define the transmittance \tilde{T} as the measured transmittance including the effect of diffraction and different shape and size of the reference aperture, while T is the Kramers-Kronig consistent transmittance calculated from the phase data. We will imply the ω dependence and not explicitly write $\tilde{T}(\omega)$ or $\Delta L(\omega)$. The optical path-length difference is

$$\Delta L = \Delta L_{sample} - \Delta L_{reference}, \quad (8.1)$$

where $\Delta L_{reference}$ is described by Eq. 3.1 and ΔL_{sample} additionally has the sample included in L_{THz} . When ΔL is measured with circularly polarized light, we will write ΔL_{RCP} and ΔL_{LCP} in the following. We can write $\Delta L = (\tilde{n} - 1) \cdot d$, where \tilde{n} is the effective n still including multiple reflections within the sample, and d is the thickness of the sample. In the case of circularly polarized light, we write $\Delta L_{RCP} = (\tilde{n}_{RCP} - 1) \cdot d$ and $\Delta L_{LCP} = (\tilde{n}_{LCP} - 1) \cdot d$ where RCP and LCP correspond to the polarization of light used for the investigation. Using a fit, we can extract n_+ and n_- , the real part of the refractive index for positive and negative helicity without multiple reflections. Due to the fact that a circularly polarized wave which is reflected at the surface changes helicity, $\tilde{n}_{RCP}(n_+, n_-)$ and $\tilde{n}_{LCP}(n_+, n_-)$ are functions of both n_+ and n_- .

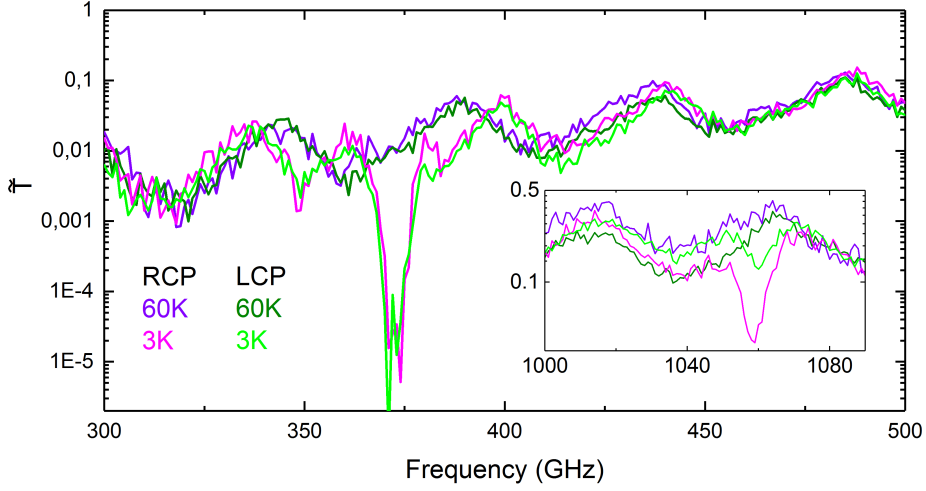


Figure 8.1: The transmittance \tilde{T} with RCP (LCP) light at 60 K, purple (dark green), and 3 K, magenta (light green). At 3 K, strong features appear at 372.4 GHz and 1058.8 GHz when measuring with RCP and LCP light. Frequency step size equals 1 GHz for RCP and 0.5 GHz for LCP light. The periodic oscillations correspond to Fabry-Perot interference fringes.

8.1 Results at 3 K

The naturally measured quantity of our setup is the response to LCP light. Using the method described in chapter 2, the response to RCP light can be recorded as well. With an optical cryostat, zero-field measurements were recorded from 300 K to 3 K for the single-domain sample (see Sec. 6.3). Since the absolute value of the transmittance (\tilde{T}) is affected by diffraction, the main focus lies on finding relative changes in the transmission of LCP and RCP light, and upon varying external parameters such as magnetic field or temperature, for example by driving the system through the phase transition at 53 K.

8.1.1 Transmittance and ΔL

In Figure 8.1, the transmittance \tilde{T}_{RCP} (purple) and \tilde{T}_{LCP} (dark green) at 60 K is compared to \tilde{T}_{LCP} (light green) and \tilde{T}_{RCP} (magenta) at 3 K. The frequency step-size is 1 GHz for \tilde{T}_{RCP} and 0.5 GHz for \tilde{T}_{LCP} . Two absorption features can be seen in both spectra at 3 K. The frequency positions at 372.4 GHz ($\approx 12.42 \text{ cm}^{-1}$) and 1058.8 GHz ($\approx 35.32 \text{ cm}^{-1}$) agree very well with the positions of the two Raman active modes at 12.7 cm^{-1} and 35.3 cm^{-1} reported by Skiadopoulou *et al.* [73]. The

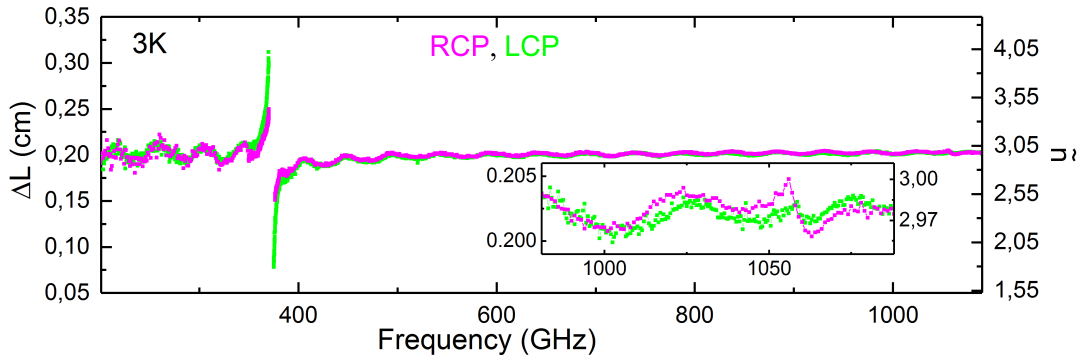


Figure 8.2: Path-length difference $\Delta L_{RCP} = (\tilde{n}_{RCP} - 1)d$ (magenta) and $\Delta L_{LCP} = (\tilde{n}_{LCP} - 1)d$ (light green) at 3K. Data show a large difference between the two polarizations (and therefore n_+ and n_-) around 372.4 GHz. Inset shows a smaller difference around 1058.8 GHz. Frequency step size equals 1 GHz for RCP and 0.5 GHz for LCP light.

lowest phonon mode was found at far higher frequency of 185 cm^{-1} at 3 K [73]. The absorption at 372.4 GHz, observed for both helicities of light, suppresses the transmittance by more than two orders of magnitude. Together with the already suppressed signal due to diffraction, a difference between the response to RCP and LCP light can not be observed on this scale due to the limiting dynamic range. At 1058.8 GHz, a large difference in \tilde{T}_{LCP} and \tilde{T}_{RCP} of more than one order of magnitude can be seen.

In the next part, we present a detailed comparison on the single-domain sample for light with positive and negative helicity at 3 K and the rotation of linear polarization with respect to the incoming polarization plane.

The capability of the setup of measuring the phase data additionally to the amplitude information gives direct insight in the behavior of the refractive index n_{\pm} for the two helicities of light, respectively. In a first approximation, including multiple reflections within the sample, we can write $\Delta L_{RCP} = (\tilde{n}_{RCP} - 1)d$ and $\Delta L_{LCP} = (\tilde{n}_{LCP} - 1)d$. The sample thickness is 1.05 mm. ΔL for LCP (green) and RCP (magenta) light at 3K is plotted in Fig. 8.2. Left scale refers to ΔL in cm while right scale refers to \tilde{n} . A large difference of ΔL is visible around 372.4 GHz between both helicities. While the extrema of ΔL_{RCP} are 0.152 cm and 0.25 cm, the extrema of ΔL_{LCP} are 0.044 cm and 0.310 cm. This leads directly to a difference in \tilde{n}_{RCP} and \tilde{n}_{LCP} . The second excitation at 1058.8 GHz is stronger in ΔL_{RCP} than in ΔL_{LCP} (see inset of Fig. 8.2). The change of about $40 \mu\text{m}$ in ΔL_{RCP} at 1058.8 GHz is only about 1.4% of the change in ΔL_{LCP} at 372.4 GHz. An advantage of a frequency-domain spectrometer is that additional measurements with a smaller frequency step size can further resolve the frequency range around 372.4 GHz at 3 K. Therefore, measurements from 350 GHz to 390 GHz with a fre-

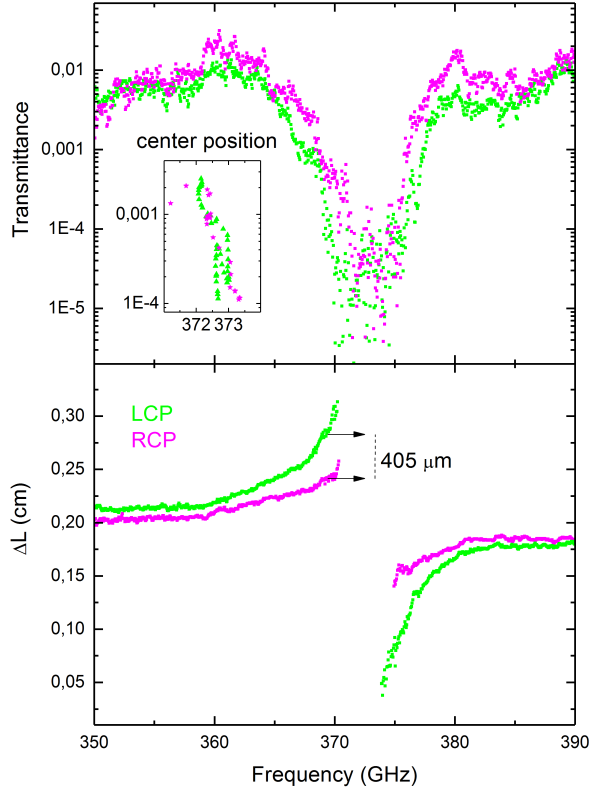


Figure 8.3: Transmittance (upper panel) and ΔL (lower panel) at 3K measured with LCP (light green) and RCP (magenta) light. Frequency range is from 350 GHz to 390 GHz with a frequency step-size of 50 MHz. Transmittance shows a clear difference in the absorption between RCP and LCP light before reaching the noise level between 10^{-4} and 10^{-5} . Center position is estimated from the average position wherefore spectra were smoothed over 250 MHz. ΔL shows a much stronger response in LCP light than in RCP light.

frequency step-size of 50 MHz were made, see Fig. 8.3. Both data sets consist of 4 averaged frequency sweeps. On this scale, the transmittance around 370 GHz is observably different for LCP and RCP light. As a first approximation of the frequency position, the average at several transmittance levels was determined, see inset. Both for RCP and LCP light, the absorption is centered around $372.4 \text{ GHz} \pm 0.7 \text{ GHz}$. ΔL is presented in the lower panel of Fig. 8.3. The data from ΔL was cut out in the frequency range where the transmittance reaches the noise level, which is slightly different for ΔL_{RCP} and ΔL_{LCP} . The difference between ΔL_{RCP} and ΔL_{LCP} is $\approx 100 \mu\text{m}$ at 350 GHz and increases at 370 GHz to $405 \mu\text{m}$ for a 1.05 mm thick sample. This corresponds to half a vacuum wavelength at 370.45 GHz. The retardation of one helicity of light by half a wavelength compared to the other one is remarkable because the optical thickness of the material at this frequency is only ≈ 4.2 wavelengths for RCP light and ≈ 4.7 wavelengths for LCP light. Above 375.5 GHz ΔL_{RCP} and ΔL_{LCP} rapidly rise together until they almost meet at 1.82 mm at 390 GHz. As discussed in Sec. 5.2, this difference can only be explained by the presence of χ_{xx}^{me} and χ_{xy}^{me} , therefore both features

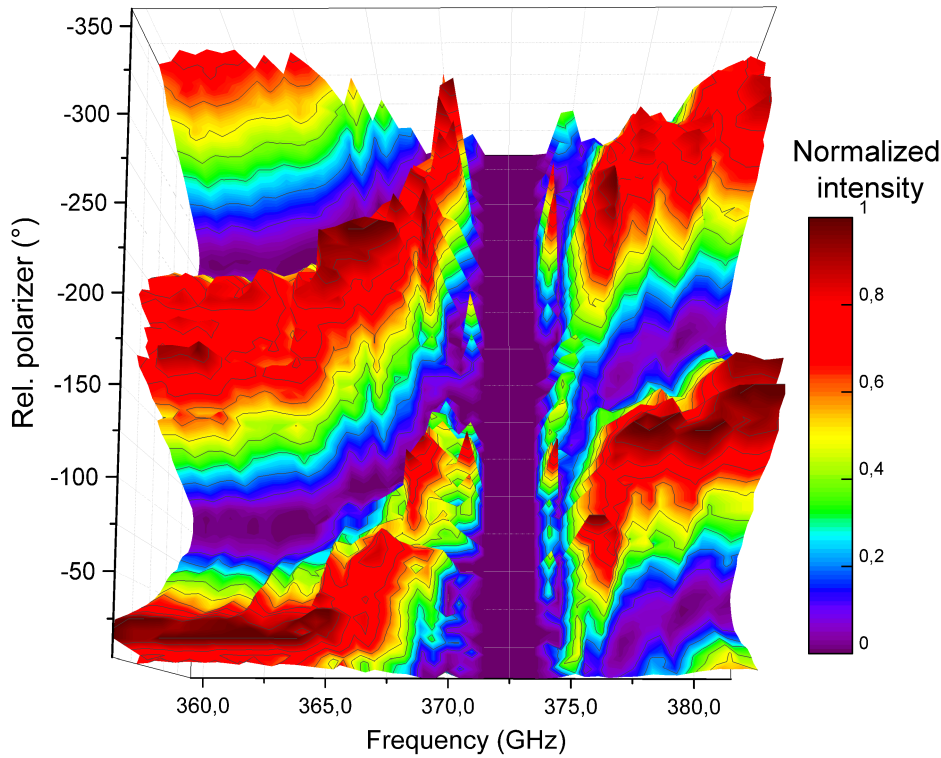


Figure 8.4: 3D plot at $T= 3K$ showing the normalized intensity distribution in the frequency range between 359 GHz and 382 GHz upon rotating the analyzer with respect to the polarizer. The plane of polarization of the incoming linearly polarized light is rotated by the sample by more than $\approx 100^\circ$ close to the absorption center at 372.4 GHz. Frequency step width is 0.5 GHz and relative rotation of the analyzer is 5° between two spectra. In the frequency range between 371 GHz and 374.5 GHz, the angle is set to zero.

have to be electromagnons.

8.1.2 Rotation of the plane of polarization for linearly polarized light

The finite difference between \tilde{n}_{RCP} and \tilde{n}_{LCP} implies that, for linearly polarized light, the plane of polarization will rotate. Using two linear polarizers in the setup, the first behind the transmitter as a polarizer, the second in front of the receiver as an analyzer, this can directly be measured. 72 spectra with a frequency step size of 0.5 GHz were taken while the polarizer was kept fixed and the analyzer was rotated by 5° in between successive spectra. The normalized intensity at each frequency between 359 GHz and 382 GHz is plotted in Fig. 8.4 as a function of the relative

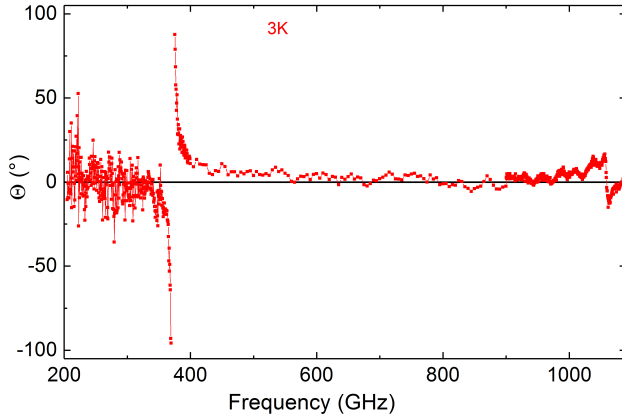


Figure 8.5: Rotation angle Θ of the plane of polarization for linearly polarized light in the frequency range from 200 GHz to 1090 GHz at $T = 3\text{ K}$. Close to the two excitations, $|\Theta|$ increases up to 100° around 372.4 GHz and 16° around 1058.8 GHz. Features at $\approx 850\text{ GHz}$ are visible at all temperatures up to room temperature and are assigned to geometrical problems due to the sample shape, see Fig. 6.5 c).

rotation between polarizer and analyzer. For frequencies between 371 GHz and 374.5 GHz, the values were set to zero since the intensity is too small in this range. At 360 GHz, position of maximum intensity is already shifted by almost -20° from parallel polarizers while it is $\approx 30^\circ$ at 380 GHz. Upon approaching the frequency of the excitation at 372.4 GHz, the positions of maximum intensity (red) start to shift. Already by only looking at the data it is clear that the plane of polarization rotates by more than 100° on each frequency side.

In order to investigate the rotation Θ of the plane of polarization in the whole frequency range, 36 spectra with a frequency step-size of 5 GHz from 200 GHz to 1100 GHz were measured with a rotation of the analyzer angle of 10° in between successive spectra. Additionally, the frequency ranges from 200 GHz to 400 GHz and 900 GHz to 1100 GHz were covered with a frequency step-size of 0.5 GHz and for the lower range, 72 spectra each 5° were measured. Furthermore, a few selected frequencies close to 372.4 GHz were measured independently. A \cos^2 function was fitted to the intensity at every frequency to obtain Θ . Data was not considered when the result of the fit was not conclusive. The resulting rotation of the plane of polarization for linearly polarized light is plotted as a function of frequency in Fig. 8.5. To exclude any polarization prioritization due to the setup, the rotation for the reference was determined as well and subtracted from the data. At low frequencies, the reference shows no polarization prioritization, while at higher frequencies, a small contribution due to the orientation of the finger structure in the receiver antenna can be seen, which is less than 6° at 1 THz.

For frequencies below 330 GHz, Θ looks rather scattered. No clear trend can be observed and the deviation is up to 50° within a few GHz. The strong diffraction at these frequencies suppresses the intensity and thus makes it difficult to capture relative changes in the amplitude due to the rotation of the polarizers and additionally it is overlaid by the changing standing waves when one polarizer is

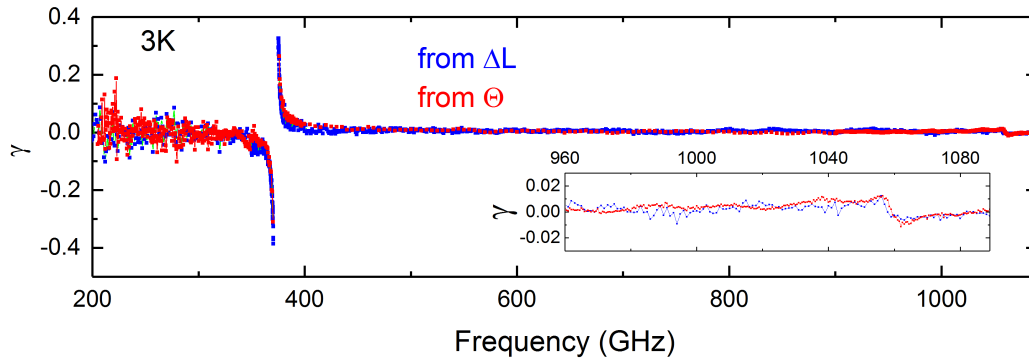


Figure 8.6: Chirality factor γ at $T=3K$ as a function of frequency calculated from ΔL (blue) and Θ (red), respectively. Both data sets show a very similar frequency dependence around 372.4 GHz and 1058.8 GHz (inset).

rotated¹. Close to the first excitation at 372.4 GHz, the rotation angle deviates strongly from zero. The maximum measured deviation is $\approx 100^\circ$ at 370 GHz.

Close to the second excitation at 1058.8 GHz, the rotation of the polarization plane of the incoming light reaches a maximum value of 16° . At around 1080 GHz it is again close to zero. For the frequency range in between the two excitations, the relative rotation is mostly around 5° .

8.1.3 Comparison of the results for ΔL and Θ

The data presented above for 3 K show two excitations at 372.4 GHz and 1058.8 GHz which show a huge difference in absorption as well as refractive index when measured with the two opposite helicities of light. The difference between ΔL_{RCP} and ΔL_{LCP} as well as the rotation of the polarization plane independently show signs of a large chirality close to the electromagnons. In order to compare those measurements quantitatively, the chirality factor can be calculated as a function of frequency from both data sets independently, compare Eq. 5.39.39. ΔL_{RCP} and ΔL_{LCP} show fringes, but they are basically the same and the difference $\Delta L_{RCP} - \Delta L_{LCP}$ hardly shows any fringes, therefore the approximation $\Delta L_{RCP} - \Delta L_{LCP} \approx 2\gamma d$ leads to

$$\gamma \approx \frac{\Delta L_{RCP} - \Delta L_{LCP}}{2d}. \quad (8.2)$$

¹Rotation of the polarizer in this setup is done by hand.

This is an approximation because $(\Delta L_{RCP} - \Delta L_{LCP}) = (\tilde{n}_{RCP} - \tilde{n}_{LCP})/d \approx (n_+ - n_-)/d$. Using $\Theta = \frac{\omega d}{c}\gamma$, compare Sec. 5.3, leads to

$$\gamma = \Theta \frac{c}{\omega d}. \quad (8.3)$$

The results obtained from the polarization rotation (red) and ΔL (blue) are compared in Fig. 8.6. The overall agreement between the two data sets is very good. γ reaches maximum values of -0.4 and 0.35 and might still increase closer to the excitation but the very large absorption limits the accessible frequency range. It would be desirable to decrease the sample thickness, but due to the cracks inside the sample this is not possible with this particular piece (see Sec. 6.3).

8.1.4 Fits of the data

The experimental result ΔL_{LCP} yields only a fast approximation of the refractive indices since it also shows fringes, i.e. effects of multiple reflections. To extract the real and imaginary part of the refractive index, from the data, a model has to be fitted to the data. For calculating the transmittance through a chiral slab, as discussed in Sec. 5.3 is used. The refractive index is given by Eq. 5.2.7:

$$N_{\pm} = \sqrt{\epsilon'_{xx}\mu'_{xx} - (\chi''_{xy})^2} \pm i\chi''_{xx} \quad (8.4)$$

with

$$\epsilon'_{xx} = \epsilon_{xx}^{\infty} + \frac{\omega_p^2}{\omega_0^2 - \omega^2 - i\gamma\omega} \quad (8.5)$$

$$\mu'_{xx} = \mu_{xx}^{\infty} + \frac{\omega_m^2}{\omega_0^2 - \omega^2 - i\gamma\omega} \quad (8.6)$$

$$\chi''_{xx} = i \frac{\omega\omega_{xx}}{\omega_0^2 - \omega^2 - i\gamma\omega} \quad (8.7)$$

$$\chi''_{xy} = i \frac{\omega\omega_{xy}}{\omega_0^2 - \omega^2 - i\gamma\omega}. \quad (8.8)$$

Instead of fitting the transmittance it was chosen to fit ΔL , which can be calculated from the phase of the complex transmittance, since the large error in the absolute value of the transmittance would have a significant impact on the fit. A small phase offset $\varphi_0 = -0.2$ has to be added to the data to describe the overall shape from 200 GHz to 1600 GHz simultaneously. This phase offset is the same for all measurements and it does not change upon changing temperature with this setup. It also does not change anything according to the physical interpretation of the data. The fitting program `DeltaLFit_v58qt2` simultaneously fits ΔL_{LCP} and

²The technical realization of this program is the sole work of David Maluski.

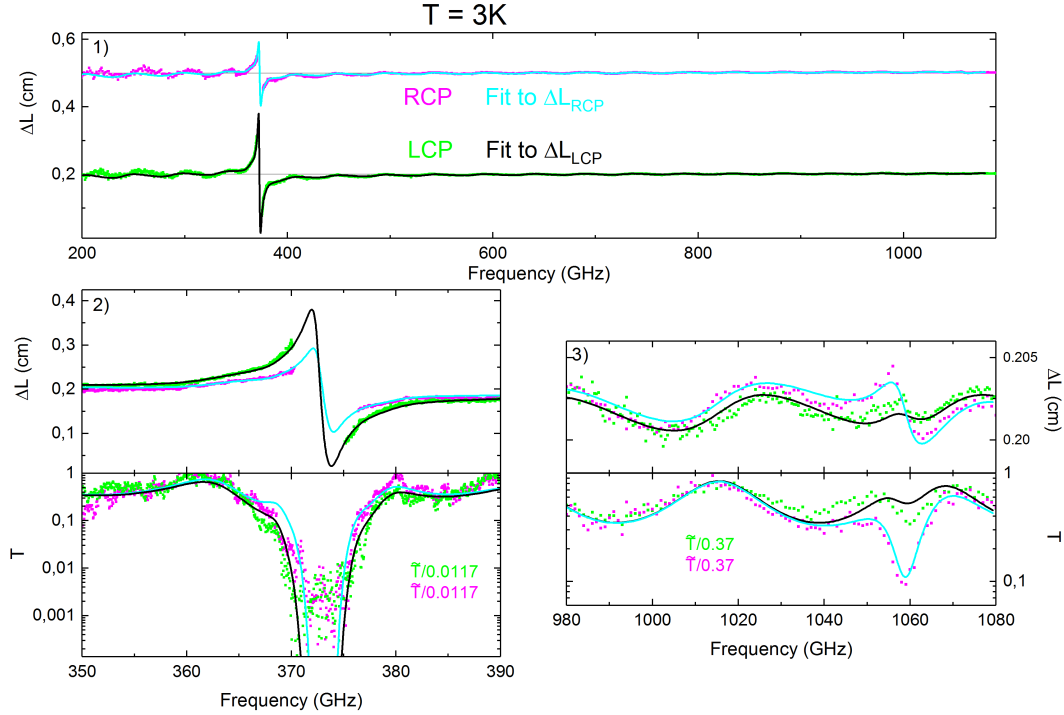


Figure 8.7: Panel 1: Overall spectrum of ΔL_{RCP} (magenta) and ΔL_{LCP} (light green), offset for better visibility, with fit (black for LCP and cyan for RCP). Panel 2 shows frequency range between 350 GHz and 390 GHz for ΔL in the upper part and T in the lower part. The measured \tilde{T} is rescaled by a frequency independent factor of $1/0.0117$ to show the qualitative agreement with T . Panel 3 shows the same graphs in the frequency range between 980 GHz and 1080 GHz, using a rescaling factor of $1/0.37$ for \tilde{T} .

ΔL_{RCP} . Distinguishing the 4 independent parameters ω_p , ω_m , ω_{xy} , and ω_{xx} from two data sets is complicated. Due to the similar appearance of ϵ_{xx} and μ_{xx} , their influence on the shape of ΔL is similar. The resulting values for ω_p and ω_m strongly depend on the value chosen for the initialization of the fit. The constraint given by Eq. 5.2.1 helps finding a solution. Therefore, ω_m was set to different values by hand. After the fit it was checked how precise the constraint is fulfilled and the best agreement is presented here. From the fit, real and imaginary parts of the complex refractive index N_{\pm} can be extracted and all optical properties depending on the refractive index can be calculated.

Furthermore, the transmittance T_{RCP} and T_{LCP} without the effect of diffraction can be calculated from the fit. This can be compared qualitatively to the measured data. Multiplying the measured \tilde{T} with a frequency independent constant can bring calculated and measured transmittance data together within small frequency ranges. The result for a fit to the data discussed above for 3K is shown in

Fig. 8.7. Parameters of the fit are presented in Tab. 8.1.

The overall agreement of fit and data is shown in panel 1). The black curve represents the fit to ΔL_{LCP} (light green) while the cyan curve corresponds to the fit to ΔL_{RCP} (magenta). Overall, the Fabry-Perot pattern is well reproduced. To reproduce the slight increase of ΔL for higher frequencies, an oscillator at the lowest phonon frequency 180 cm^{-1} was assumed [73]. This is far outside the measurement range and only has a small influence on the overall shape. The two electromagnons at 372.4 GHz and 1058.8 GHz can be described using one oscillator each. Figure 8.7 2) shows ΔL (upper panel) and transmittance (lower panel) in the range between 350 GHz and 390 GHz . The fit to ΔL describes both helicities accurately not only for ΔL_{LCP} and ΔL_{RCP} but also for the rescaled \tilde{T}_{RCP} and \tilde{T}_{LCP} using $\omega_{xx} = 0.043 \text{ cm}^{-1}$ and $\omega_{xy} = 0.13 \text{ cm}^{-1}$. ω_{xy} has no clear representation in the phase, therefore it is difficult to extract this value. Fitting the transmittance simultaneously would help getting more precise values there. Figure 8.7 panel 3) shows the frequency range between 980 GHz and 1080 GHz around the second electromagnon. The relatively weak representation in LCP light is close to the limit that can be fitted, leading to a small difference between the two simultaneously fitted curves and the data. This is especially visible in the comparison of the rescaled \tilde{T} for LCP light in comparison to T . There, already at 1040 GHz , the measured data differ from the fit. This wave-like difference positionally reminds on the features that can arise from diffraction in that range, compare Fig. 7.1. But overall the fit describes the data sufficiently accurate to analyze the data in more detail.

Table 8.1: Fit parameters for 3 K . All parameters which are fixed during the fit are marked as *fixed*. Thickness is 0.1050 cm , ϵ_∞ is 8.51 and a phase offset φ_0 is fixed at -0.2 . EM1 and EM2 denote to the electromagnons at 372.4 GHz and 1058.8 GHz .

		EM1	EM2	phonon
ω_0	(cm^{-1})	12.42	35.32	180 <i>fixed</i>
γ	(cm^{-1})	0.050	0.30	60 <i>fixed</i>
ω_p	(cm^{-1})	2.31	0.53	80 <i>fixed</i>
ω_m	(cm^{-1})	0.77	0.18	0
ω_{xx}	(cm^{-1})	0.043	-0.0045	0
$\omega_0 \cdot \omega_{xx}$	(cm^{-2})	0.53	-0.16	0
ω_{xy}	(cm^{-1})	0.13	0.001	0
$\omega_0 \cdot \omega_{xx}$	(cm^{-2})	1.6	0.035	0

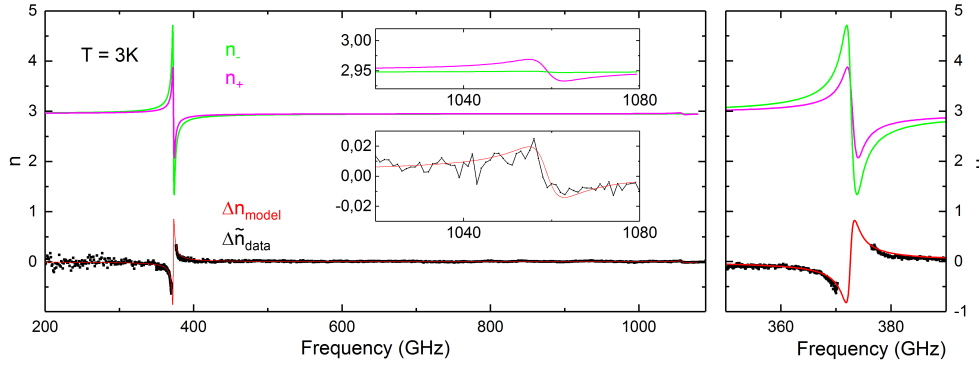


Figure 8.8: Real part n_+ (magenta) and n_- (light green) of the refractive index extracted from the fit in the frequency range between 200 GHz and 1090 GHz. Insets show range between 1020 GHz and 1080 GHz. The model shows a finite difference $\Delta n_{model} = n_+ - n_-$ (red) which is in good agreement with the measured difference $\Delta \tilde{n}_{data} = (\Delta L_{RCP} - \Delta L_{LCP})/d$ (black).

8.1.4.1 Real and imaginary part of the refractive index at 3 K

The real parts of the refractive index, n_+ (magenta) and n_- (light green), are shown in Fig. 8.8. The large difference between n_+ and n_- due to the χ_{xx} term is represented in the large $\Delta n_{model} = n_+ - n_-$ which reaches values of ± 0.81 close to 372.4 GHz. Close to the second electromagnon at 1058.8 GHz, Δn_{model} is almost two orders of magnitude smaller with 0.021 and -0.014. Directly from the data, $\Delta \tilde{n}_{data} = (\Delta L_{RCP} - \Delta L_{LCP})/d$ (black) can be compared with the result of the fit. The oscillations caused by multiple reflections within the sample cancel almost completely except close to the excitations where the relative difference in n causes a difference in the multiple reflections for LCP and RCP, respectively. Nevertheless, the measured and the calculated result from the fit are in good agreement in the frequency range close to both electromagnons. Similarly, the imaginary part of the refractive index, κ_+ (magenta) and κ_- (light green), can be compared, see Fig. 8.9 left panel. κ_- reaches a value above 3, whereas the maximum of κ_+ is with 1.6 approximately only half this value, therefore the difference $\Delta \kappa_{model} = \kappa_+ - \kappa_-$ (red) on the right side is approximately $1/2 \kappa_-$. For the electromagnon at 1058.8 GHz, κ_+ is larger than κ_- (see insert of left panel), and the difference $\Delta \kappa_{model}$ is almost as large as κ_+ . This means that the absorption for one polarization of light is considerably larger than for the other one. If the difference is large enough, only one polarization passes through the sample while the other one is absorbed. To quantify this effect, the thickness parameter in the model can be used and the transmittance for various thicknesses can be compared directly.

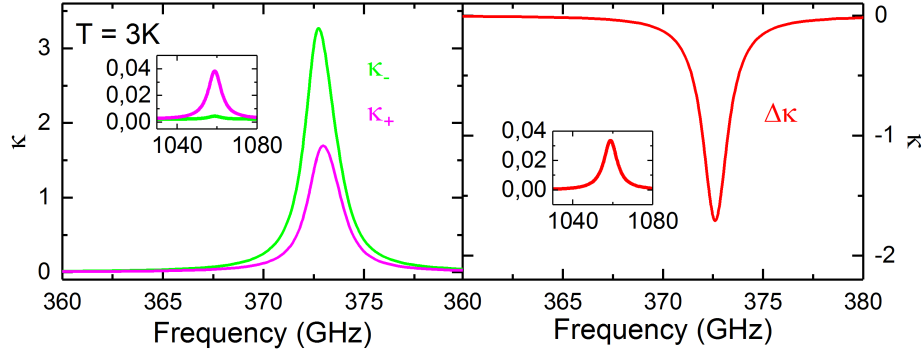


Figure 8.9: Imaginary part κ_+ (magenta) and κ_- (light green) of the refractive index extracted from the fit in the frequency range between 360 GHz and 380 GHz on the left hand side. Difference $\Delta\kappa_{model} = \kappa_+ - \kappa_-$ (red) on the right hand side. Insets show range from 1030 GHz and 1080 GHz

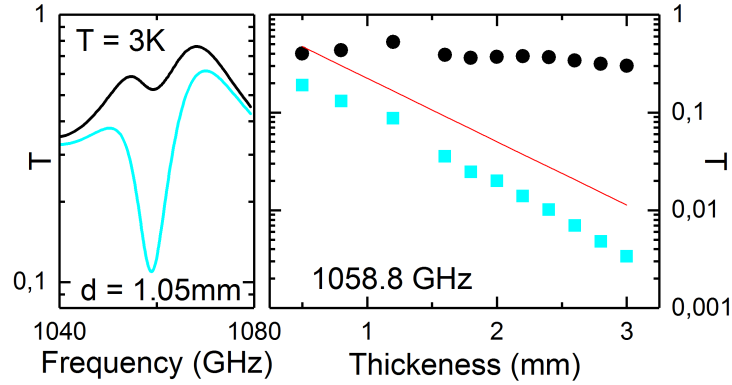


Figure 8.10: Left: T calculated from fit to ΔL for LCP (black) and RCP (cyan) for a 1.05 mm thick sample. Right: T at 1058.8 GHz as a function of thickness in the model. Minimum transmission read out for LCP (black) and RCP (cyan). Ratio T_{RCP}/T_{LCP} in red.

8.1.4.2 Modeled thickness dependence of the transmittance at 1058.8 GHz

Figure 8.10 shows the resulting transmittance from the fit to ΔL at 3 K for LCP (black) and RCP (cyan) light. On the right side, the sample thickness in the model is varied between 0.5 mm and 3 mm. The resulting value at 1058.8 GHz is plotted for T_{RCP} and T_{LCP} as a function of the thickness. The modulation in the values between 0.5 mm and 2 mm depends on the position of the excitation with respect to the Fabry-Perot fringes. The red line represents the ratio T_{RCP}/T_{LCP} which shows that for 3 mm thickness, where T_{LCP} is still $\approx 30\%$, T_{RCP} is only $\approx 0.3\%$ which is equivalent to 1% of T_{LCP} , so the sample acts as a circular polarizer at

that frequency already in zero magnetic field.

8.1.4.3 Fit result and Θ

The rotation of the plane of polarization of linearly polarized light can be calculated from the difference Δn_{\pm} of the model according to $\Delta n_{\pm} = \Theta \frac{c}{\omega d}$. This can directly be compared to the measured Θ presented in Fig. 8.5. The result is shown in Fig. 8.11. The agreement between the measured data and the result from the fit to ΔL is excellent.

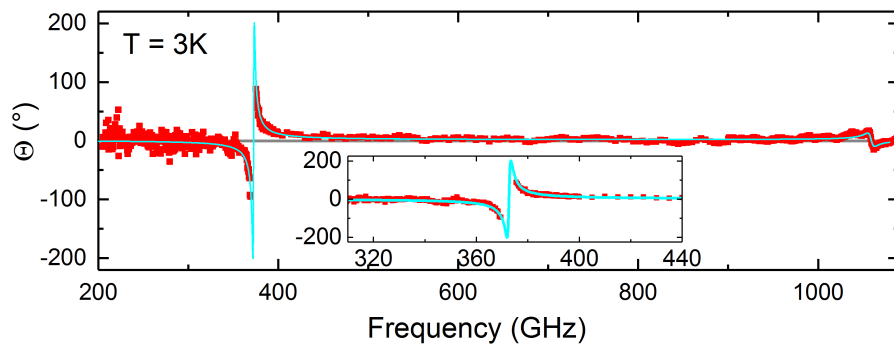


Figure 8.11: Measured (red) and calculated (cyan) rotation angle of the plane of polarization for linearly polarized light. The calculated data result from the fit of ΔL_{LCP} and ΔL_{RCP} , see Fig. 8.7. Inset shows range between 320 GHz and 480 GHz. Data is measured with different frequency step sizes in between 400 GHz and 900 GHz, compare Fig. 8.5.

8.2 Temperature dependence

To investigate the temperature dependence, several spectra were measured between 300 K and 3 K. All measurements within the paramagnetic phase show only a small thermal-expansion-induced length change of the sample and a temperature-dependent broadening of the lowest phonon mode at $\approx 180 \text{ cm}^{-1}$. In the following, the focus lies on the temperature dependence of the modes below the phase transition at 53 K.

8.2.1 Temperature dependence of ΔL

The optical path-length difference ΔL measured with LCP (upper panel) and RCP (lower panel) light is shown in Fig. 8.12. For temperatures above 60 K, just above the phase transition at 53 K, see Sec. 6.2, data agree with each other. After entering the antiferromagnetic phase, the data taken at 40 K (cyan) show a slight increase at around 290 GHz corresponding to the emergence of a relatively broad mode in both polarizations. Below 40 K, the difference between the LCP and RCP data becomes more pronounced. The upper insets show the frequency range between 280 GHz and 390 GHz on enlarged scale. The second inset in the lower panel shows the emergence of the second electromagnon at 1058.8 GHz below 26 K, which is not strong enough in ΔL_{LCP} to be resolved above 3 K. The overall behavior can

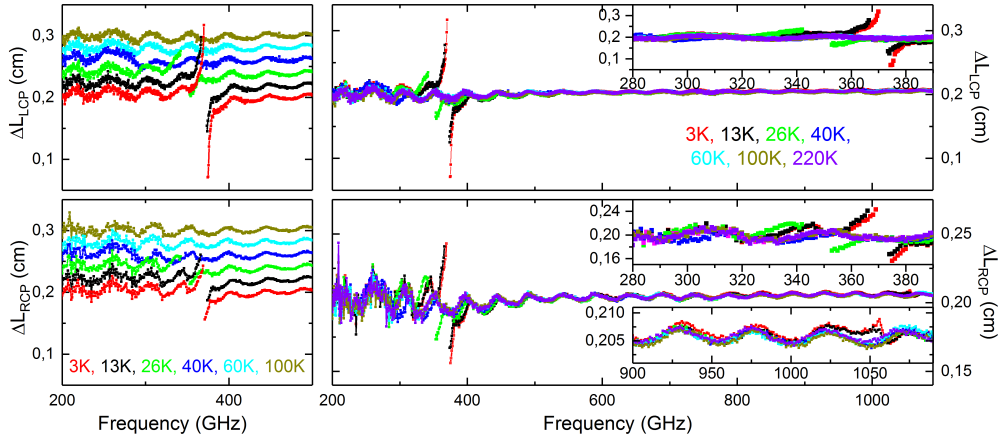


Figure 8.12: Top panel: Temperature dependence of ΔL_{LCP} measured with frequency step size of 0.5 GHz. Bottom panel: ΔL_{RCP} measured with frequency step size of 1 GHz. Insets show frequency ranges from 280 GHz to 390 GHz and 900 GHz to 1080 GHz, respectively.

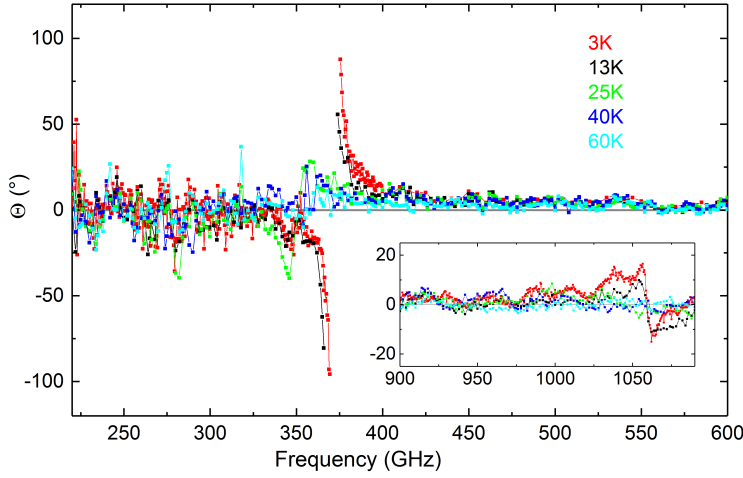


Figure 8.13: Rotation angle Θ for different temperatures between 220 GHz and 600 GHz. The maximum value of Θ decreases for increasing temperature. Inset shows data between 900 GHz and 1090 GHz.

be described by a softening and broadening of the modes with increasing temperature. For a quantitative analysis, see Sec. 8.2.4.

8.2.2 Temperature dependence of Θ

The rotation angle Θ is shown for different temperatures in Fig. 8.13. The frequency step-width was 2 GHz except at 3 K, which is the same curve already discussed in Fig. 8.5. The behavior of Θ follows the temperature dependence of the two electromagnons. With increasing temperature, the maximum value of Θ is decreasing. This means that ω_{xx} decreases or the width γ increases. The origin of the fringes in Θ around 1058.8 GHz at 3 K and 13 K could not be clarified. They could be artifacts of this particular sample due to its geometry or the aperture which only appear in the presence of a finite rotation induced by the second electromagnon, but they are relatively reproducible upon remeasuring. Measuring another sample will be necessary to clarify the origin.

8.2.3 Temperature dependence of real and imaginary parts of the refractive index

Fitting ΔL_{LCP} and ΔL_{RCP} gives the opportunity to study the temperature dependence of n_{\pm} and κ_{\pm} . The data and corresponding fits are shown in the Appendix, see 10, together with the measured Θ and the calculated Θ based on the result of the fits to ΔL_{LCP} and ΔL_{RCP} . The temperature dependence of n_{\pm} is depicted in

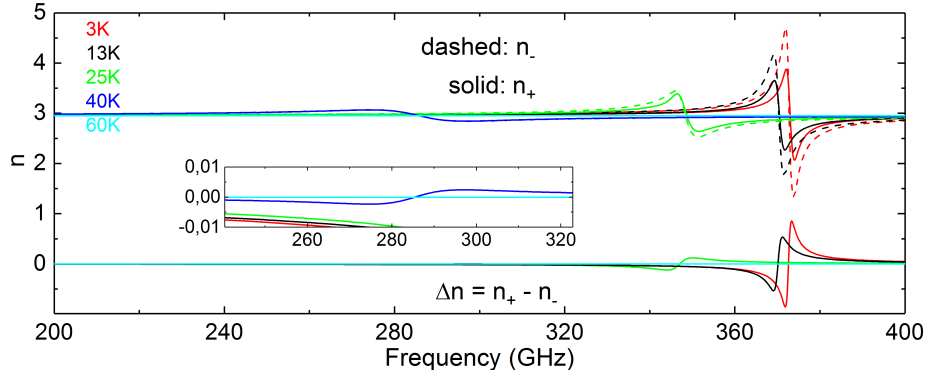


Figure 8.14: Real part n_+ (solid) and n_- (dashed) of the refractive index extracted from the fit in the frequency range between 200 GHz and 400 GHz. The model shows the difference $\Delta n_{model} = n_+ - n_-$. Inset shows the frequency range between 240 GHz and 330 GHz.

Fig. 8.14 in the frequency range between 280 GHz and 380 GHz. With increasing T , the feature in n_+ and n_- softens and broadens. The same applies to $\Delta n = n_+ - n_-$. At 40 K, the error of the fit is larger than for the lower temperatures since the frequency position below 300 GHz together with the decreasing Δn does make the fit more difficult, compare also Fig. 8.16. For κ , a similar temperature dependence in the frequency range between 280 GHz and 380 GHz can be read off, see left hand side of Fig. 8.15. κ_+ (solid) and κ_- (dashed) show a large difference at low temperatures. The maximum difference $\Delta\kappa = \kappa_+ - \kappa_-$, see Fig. 8.15 right hand side, decreases with increasing temperatures similarly to the maximum difference Δn_{model} . The insets show κ and $\Delta\kappa$ in the frequency range between 1020 GHz and

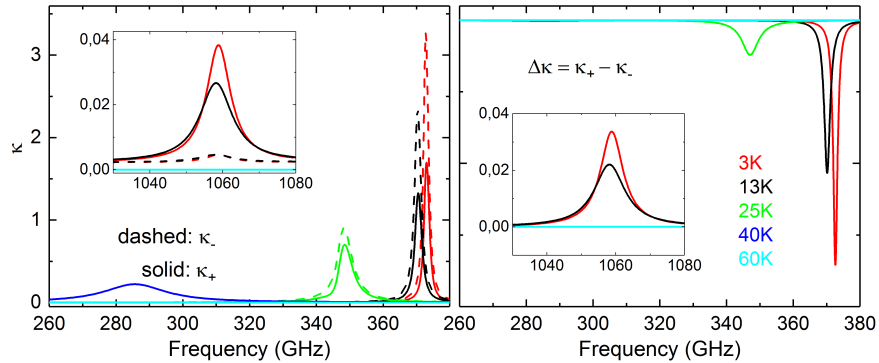


Figure 8.15: Imaginary part κ_+ (solid) and κ_- (dashed) of the refractive index extracted from the fit in the frequency range between 260 GHz and 380 GHz for different temperatures on the left hand side. Difference $\Delta\kappa_{model} = \kappa_+ - \kappa_-$ on the right hand side. Insets show range from 1030 GHz and 1080 GHz.

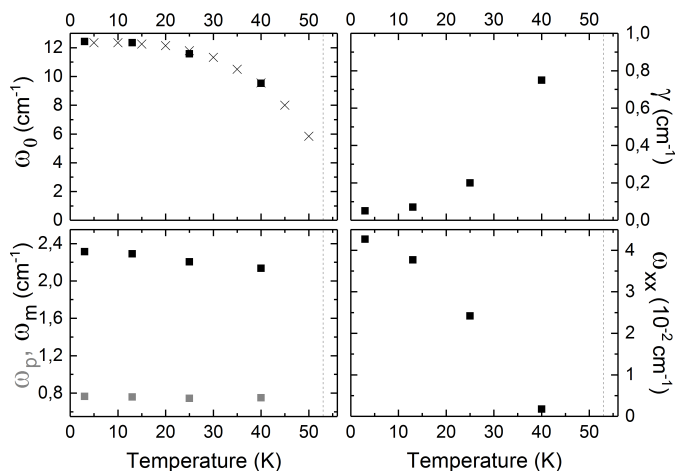


Figure 8.16: Eigenfrequency ω_0 (top left), width γ (top right), ω_p and ω_m (bottom left), and ω_{xx} (bottom right) as function of temperature. For definition of parameters, see Eqns. 8.5-8.8. The dots represent frequency positions from measurements within this thesis, whereas the crosses represent data measured from David Szaller at Vienna University of Technology on the same sample using unpolarized and linearly polarized light.

1080 GHz, respectively.

8.2.4 Temperature dependence of fit parameters

For a quantitative discussion of the electromagnon at 372.4 GHz, the temperature dependence of the parameters used for the fit is depicted in Fig. 8.16. For details about the fitting method including the constraint, see Sec. 8.1.4. ω_0 significantly softens with increasing temperature. A temperature-dependent increase in the width γ corresponds to a broadening of the mode (top right). ω_m and ω_p stay relatively constant over the temperature range whereas ω_{xx} clearly decreases. For a better picture, the temperature dependence of the transmittance would have to be fitted as well. To summarize, we find a strong softening of the mode with increasing temperature. Roughly, ω_0 extrapolates to 0 at the Néel temperature $T_N = 53$ K. The strong increase of the width γ can be attributed to an increase of magnon-magnon scattering due to an increasing magnon density. Note that $k_B T_N / (\hbar \omega_0(3K)) \approx 3$. Furthermore, the magneto-electric coupling significantly decreases with increasing temperature. It also extrapolates to zero at $T_N = 53$ K.

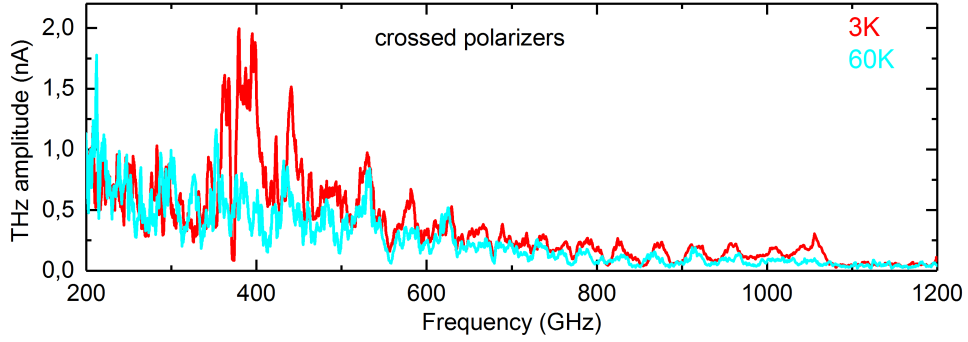


Figure 8.17: THz amplitude with crossed polarizers for 3 K (red) and 60 K (cyan). Data are averaged over 4 frequency sweeps with a step size of 0.5 GHz and smoothed over 2.5 GHz.

8.3 Parallel and crossed linear polarizers

Another possible analysis is based on measurements with parallel (pp) and crossed (cp) linear polarizers. A finite THz amplitude with crossed polarizers is a prove that the sample rotates polarization direction with respect to the incoming light. In our setup, the overall THz amplitude decreases due to the usage of linear polarizers and due to low transmittance caused by the diffraction for a small sample. Especially measurements with crossed linear polarizers are problematic. As discussed in Sec. 7, the absolute values of $\tilde{T}(\omega)$ can not be used for the analysis, but relative changes in the THz amplitude and therefore $\tilde{T}(\omega)$ due to a temperature change can be determined. Figure 8.17 shows the THz amplitude with crossed polarizers for 60 K (cyan) and 3 K (red). Data measured with a frequency step size of 0.5 GHz are averaged over four spectra and smoothed by 2.5 GHz. The 3 K data show a significant increase in the THz amplitude around the two electromagnon excitations at 372.4 GHz and 1058.8 GHz but also a small increase in the frequency range in between. Above 1070 GHz, the cp signal is not detectable.

The measured \tilde{T} in Fig. 8.18 (top left) shows a comparable suppression due to diffraction as the already discussed data for RCP and LCP light at 3 K, see Sec. 8.1. The simultaneously measured ΔL_{pp} has a quality comparable to ΔL_{RCP} and ΔL_{LCP} . For \tilde{T}_{cp} , four frequency sweeps were measured and averaged. \tilde{T}_{cp} is more than two orders of magnitude smaller than \tilde{T}_{pp} except close to the electromagnons where the huge optical rotation leads to an increased \tilde{T}_{cp} .

The top right panel shows the expected T_{pp} (cyan) and T_{cp} (orange) calculated from the fit to ΔL_{RCP} and ΔL_{LCP} at 3 K. The absolute values compared to \tilde{T}_{pp} , \tilde{T}_{cp} are strongly different due to diffraction on the small sample. For ΔL , the agreement between the measured and calculated spectra is much better. The measured ΔL_{pp}

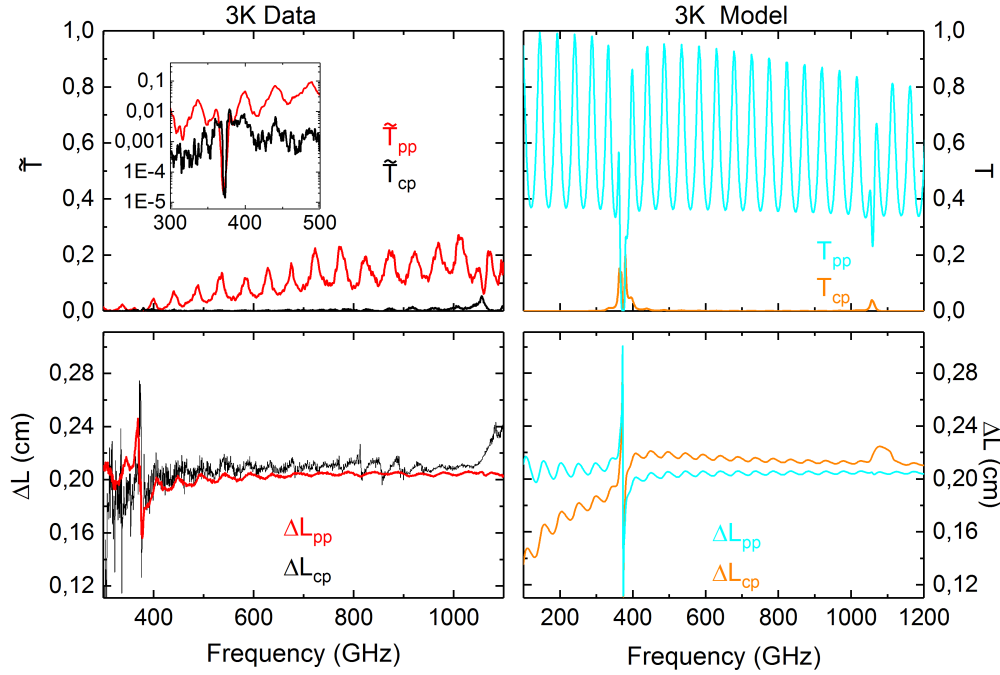


Figure 8.18: \tilde{T} (top left) and ΔL (bottom left) measured with parallel (red) and crossed polarizers (black) at 3K. T (top right) and ΔL (bottom right) calculated from the result of the fit of ΔL_{LCP} and ΔL_{RCP} at 3K, compare Fig. 8.7.

is in good agreement with the calculation and also the frequency dependent shape of ΔL_{cp} shows the same increase above 1058.8 GHz due to the presence of χ_{xx}^{me} . The effect corresponds to the frequency range with negative Δn . Below 350 GHz, the decrease in the calculated ΔL_{cp} similarly depends on the finite difference between ΔL_{RCP} and ΔL_{LCP} . For the measured data, even though the measurement time is doubled with around 80 min instead of 40 min as for the measurement with parallel polarizers, the measured signal is too scattered for fitting. It shows a similar frequency dependence at frequencies below 370 GHz but determining an accurate difference between ΔL_{pp} and ΔL_{cp} is not possible. For even lower frequency, the simulation increases back to the value of ΔL_{pp} (not shown). Additionally the features in ΔL_{cp} between 800 GHz and 900 GHz are not explained by the model. They exist similarly at all temperatures and are assigned to artifacts due to the low signal. The low signal with the crossed polarizer already in the optical cryostat prevents the usage of this method in the magnetic field setup. The THz amplitude there makes it almost impossible to determine a signal except in close proximity of the electromagnons. The quality of the data with parallel polarizers on the other hand would be sufficient for an analysis.

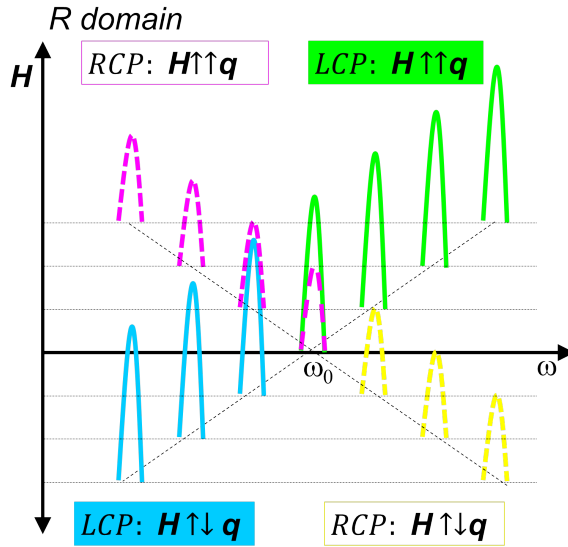


Figure 8.19: Sketch of the frequency dependence of the absorption when applying magnetic field, compare Fig. 5.4. This figure contains the simplification that the absorption features strengths does not change in magnetic field.

8.4 Data in magnetic field

With the magnetic field setup (see Sec. 1.2) we can measure the magnetic field dependence up to 8 T. So far, this setup is restricted to LCP light due to constructional reasons. Investigating the other domain with LCP light would give additional insight, as discussed in Sec. 5.1.1. Unfortunately the other domain covers three separate areas of less than 0.4 mm^2 each, so that a relative investigation there is not possible due to the drastically increasing influence of diffraction. An investigation of the uncovered sample on both domains simultaneously might give some additional hints if it is possible to disentangle the contributions of the two domains. The results of those measurements are presented in the second part, see Sec. 8.4.2.

8.4.1 Single-domain sample

Before looking at the spectra, it is necessary to think of what to expect based on the finding that there are two magnon modes with different strength as a function of light polarization already in zero field. In Figure 8.19, the absorption for LCP (green) and RCP (magenta) are at frequency ω_0 in zero field. When applying a magnetic field \mathbf{H} in the direction of \mathbf{q} and measuring with LCP light, the mode shifts to higher frequency (green) due to Zeeman splitting. This is the primary signal that is measured. For the same case of $\mathbf{H}\uparrow\uparrow\mathbf{q}$ measured with RCP light, the Zeeman effect would lead to a shift to lower frequency (magenta). But since the LCP wave which is reflected at the second surface travels backwards against

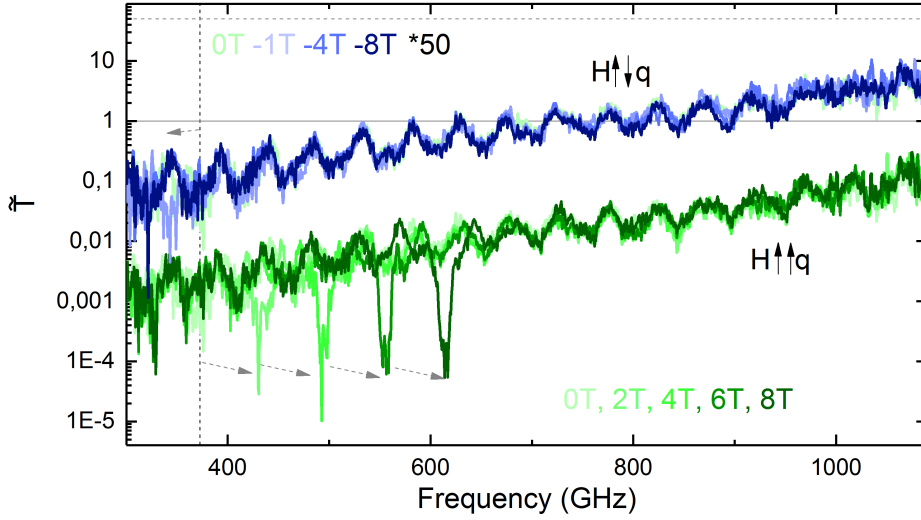


Figure 8.20: $\tilde{T}''(\omega)$ for different magnetic field strengths and $\mathbf{H}\uparrow\uparrow\mathbf{q}$ (green) or $\mathbf{H}\downarrow\uparrow\mathbf{q}$ (blue) at 13.5 K. The latter data are shifted for better visibility. Grey arrows indicate the direction of the field-dependent frequency shift of the lower electromagnon at 372.4 GHz (dashed vertical line).

the field direction, it sees the mode which is also shifted to higher frequency for $\mathbf{H}\uparrow\downarrow\mathbf{q}$ (yellow). That means we will catch a fingerprint of the yellow response at the same frequency as the green response when the RCP and the LCP part have the same field dependence. Reversing the field direction and measuring with $\mathbf{H}\downarrow\uparrow\mathbf{q}$ for LCP light leads to a shift to lower frequency for increasing field (blue).

The difference between the data measured in the magnetic-field setup and the optical cryostat was already discussed in Sec. 7. For such small samples, $\tilde{T}(\omega)$ is very different for the two setups whereas $\Delta L_{LCP}(\omega)$ is very similar but shows more noise due to lower signal in the magnet. The magnetic field dependence of $\tilde{T}(\omega)$ at 13.5 K for magnetic field along the c direction for $\mathbf{H}\downarrow\uparrow\mathbf{q}$ (blue) or $\mathbf{H}\uparrow\uparrow\mathbf{q}$ (green) is presented in Fig. 8.20. At zero field, the mode is almost not visible in the transmittance due to the higher noise level at frequencies below 400 GHz. For increasing magnetic field, the absorption shows a linear shift towards higher frequencies (green). Inverting the field direction (blue) shows no absorption at the same frequency for $|\mathbf{H}_{\mathbf{H}\uparrow\uparrow\mathbf{q}}| = |\mathbf{H}_{\mathbf{H}\downarrow\uparrow\mathbf{q}}|$ (shifted for better visibility). The absorption caused by the electromagnon at 1058.8 GHz in zero field is only observed at -1 T .

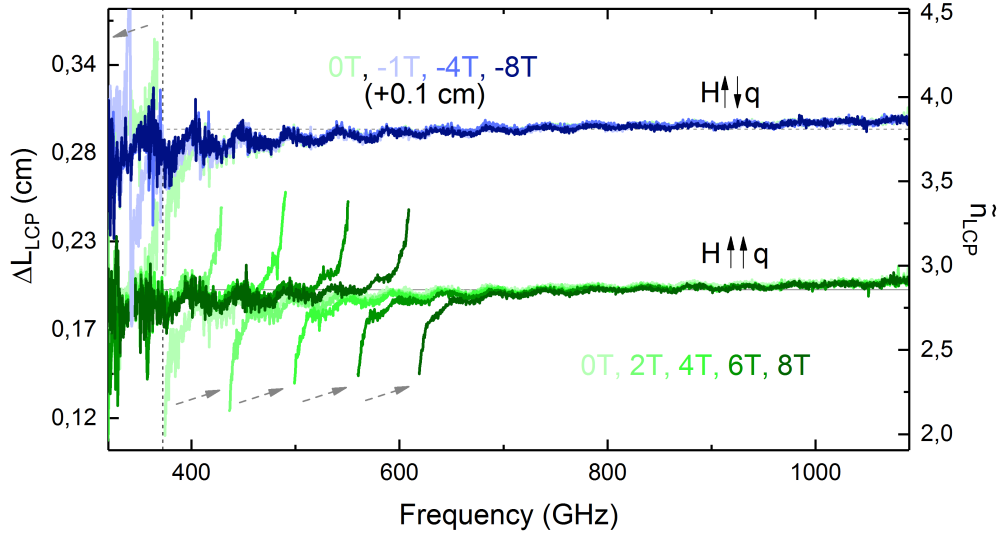


Figure 8.21: Magnetic field dependence of $\Delta L_{LCP}(\omega)$ for fields $\mathbf{H}\downarrow\uparrow\mathbf{q}$ (blue) or $\mathbf{H}\uparrow\uparrow\mathbf{q}$ (green) in the frequency range between 300 GHz and 1100 GHz at 13.5 K. The blue data is shifted by 0.1 cm for better visibility. Grey arrows indicate the direction of the field dependent frequency shift of the electromagnon at 372.4 GHz in zero magnetic field.

8.4.1.1 $\Delta L(\mathbf{H})$ and fit

Data of $\Delta L(H)$ are presented in Fig. 8.21. Since we have not measured ΔL_{RCP} in magnetic field, a fit as explained in Sec. 8.1.4 is more difficult. Switching on magnetic field breaks time reversal symmetry. The result of the discussion in Sec. 5.2 is not longer valid. A full analysis would have to take several effects as for example the possible presence of magnetic circular dichroism or magneto chiral dichroism into account, but at this point, due to the limited amount of data in magnetic field, this is not yet possible. We still want to fit the data with our model, but rather to make qualitative changes visible than for a real quantitative analysis.

For this approach, ω_{xx} , the width γ and the magnetic field dependent frequency position are used as fit parameters, whereas the other parameters are kept constant for all fields. This way, any change in the strength of the mode has to be compensated by ω_{xx} . The results for some magnetic fields are presented in Figure 8.22. The field dependence of ω_0 is described by the Zeeman effect, $\omega_0 + \omega(B)$ with $\omega_B = g \cdot |\mathbf{B}| \cdot \mu_B / \hbar$ with μ_B as Bohr magneton, \hbar as Planck constant. The corresponding g factor is 2.2. A g factor of 2.26 was found in Ref. [66] on a powder sample. In Figure 8.23, ω_0 is shown in the top left panel. The filled symbols

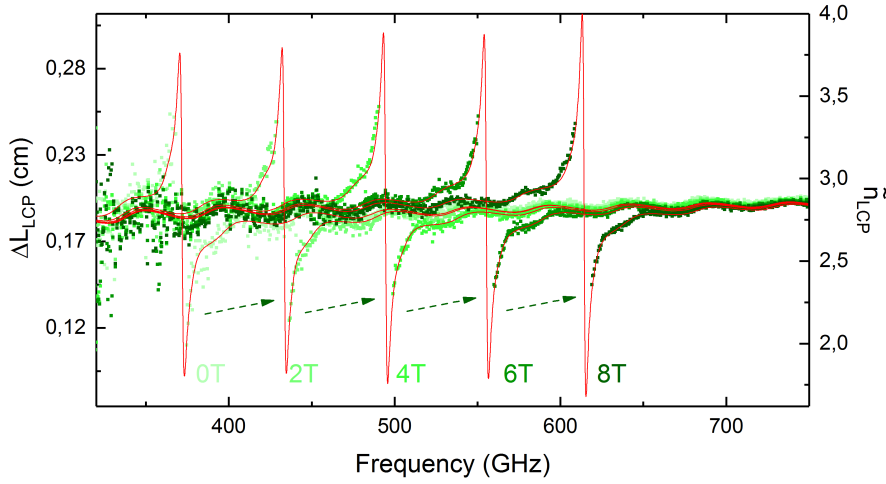


Figure 8.22: Fit (red) of $\Delta L_{LCP}(\omega)$ (green) for different magnetic fields between 0 T and 8 T. ω_p , ω_m , and ω_{xy} are set as constant whereas ω_{xx} , γ , and ω_0 are used as fit parameters at 13.5 K.

correspond to the LCP measurement, the open symbols show the expected field dependent position for the RCP measurements. The shift is described by the Zeeman effect. The damping γ is relatively constant in the measured field range. With ω_m and ω_p set constant for the fit while ω_{xx} is variable (bottom right), ω_{xx} increases for increasing field. Still, with the constant width γ and the relative

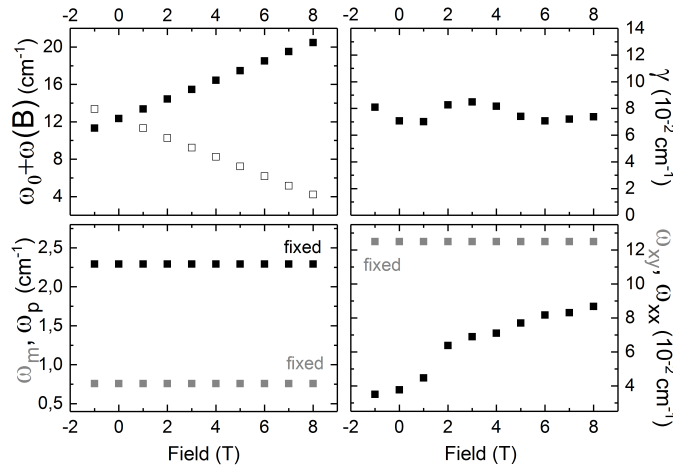


Figure 8.23: Frequency position $\omega_0 + \omega(B)$ measured with LCP light (filled symbols) and the corresponding position expected for RCP (open symbols) (top left), width γ (top right), ω_p and ω_m (bottom left), and ω_{xx} as well as ω_{xy} (bottom right) as function of magnetic field at 13.5 K.

small change in ω_{xx} for magnetic fields smaller than 1 T, in first approximation we say that Zeeman splitting is the mayor effect for small fields. Additionally it has to be pointed out that the constraint which was valid in zero field, see Eq. 5.2, no longer applies in finite magnetic field.

Measurements with LCP light confirm the splitting of the modes. The splitting of two modes that are different already in zero magnetic field for the two opposite circular polarizations, see Sec. 8.1, is the prove for the existence of quadrochromism in Ni_3TeO_6 . For magnetic fields of a few Tesla and larger, that does not catch the full complexity of the problem. Several higher order terms might become important and only a detailed analysis might be able to disentangle the contributions. But for small fields, the change in the strength of the modes is so small that the relative difference between the RCP and LCP response is in approximation the same as in zero field, only at different frequencies due to the Zeeman splitting.

8.4.1.2 Simulation of optical parameters for small magnetic fields at 3 K

In a first approximation for small magnetic fields below 0.5 T, all parameters can be treated as constant. In this case, a simulation based on the parameters found at 3 K, compare Tab. 8.1, can show the effect of a small field on Δn , $\Delta\kappa$, and Θ ,

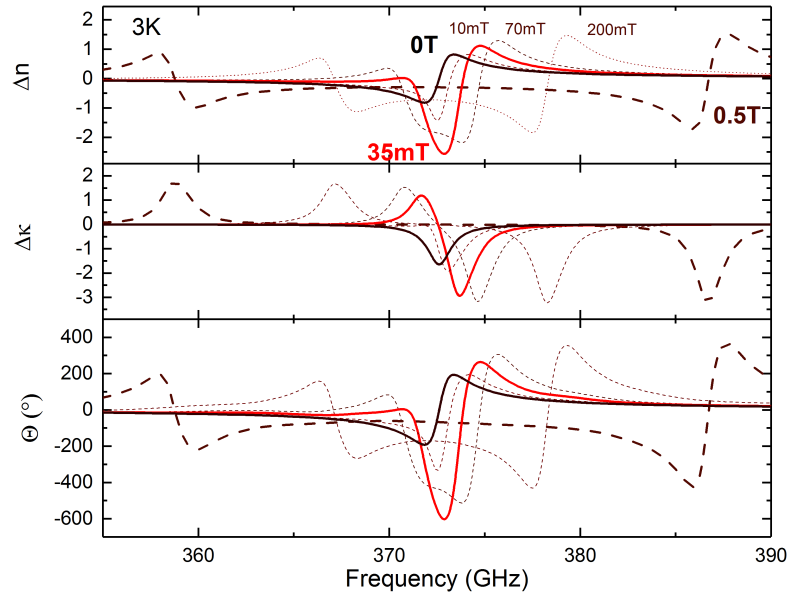


Figure 8.24: Magnetic field dependence of $\Delta n = n_+ - n_-$ (top panel) and $\Delta\kappa = \kappa_+ - \kappa_-$ (middle panel) for small magnetic fields below 0.5 T at 3 K. Resulting Θ in the bottom panel.

see Fig. 8.24.

The Δn (top panel) for zero field (black) is known from Fig. 8.8 and $\Delta\kappa$ (middle panel) from Fig. 8.9. Upon increasing the magnetic field, Δn reaches a maximum value for 35 mT because it shifts the maximum in n_- and the minimum in n_+ to the same frequency. Further increasing the field increases the energy splitting and for fields larger than 0.2 T the two modes for RCP and LCP light are well separated. Upon further increasing the magnetic field, they separate more but the shape does not change. Since Θ is directly proportional to Δn , the maximum rotation in the angle Θ is $\approx 600^\circ$ for a magnetic field of 35 mT (bottom panel). Measuring the magnetic field dependence of Θ is similarly a way of determining Δn , but it does not directly lead to an accurate description for n_+ and n_- separately. For all methods, the high absorption close to the frequency of the electromagnon makes an accurate experimental determination difficult.

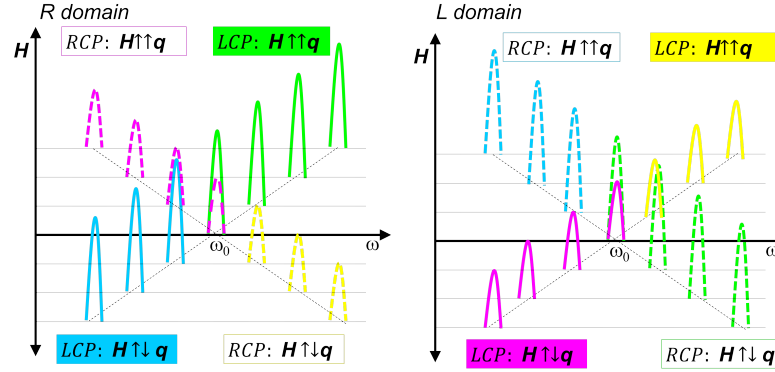


Figure 8.25: Sketch of the frequency dependence of the absorption features when applying magnetic field, compare Fig. 5.2. Left side corresponds to the domain discussed in Fig. 8.19. Right side corresponds to the second domain. This figure contains the simplification that the absorption strength does not change in magnetic field.

8.4.2 Multidomain sample

For the measurement on both domains an empty reference aperture was built with the same dimensions as the sample. The initial idea was that the area of 2.09 mm^2 is large enough to be able to get a better absolute value of the transmittance. Usually the argumentation when measuring a multidomain sample would be that some photons go through the first domain and others go through the second domain. The ratio between them would be the ratio of the domain coverage in the sample. In this case it is more complicated because the wavelength is partially larger than the size of some domains. In the domains, the THz electric field will be changed corresponding to the properties of the two domains, respectively. Upon detection, only the interfered THz electric fields can be detected. The overall interference pattern is dominated by the wedge shaped domains in the corners, see also Sec. 6.3 and Fig. 6.5 in particular. This is also the reason why only partially a Fabry-Perot pattern in \tilde{T} is visible, compare Fig. 8.26 and Fig. 8.27. Similar as before, we will search for relative changes in \tilde{T} . Due to the larger sample, \tilde{T} is measurable down to 200 GHz also in the magnetic field cryostat. Spectra are averaged over 5 GHz and normalized to the value of the highest transmittance. What is clearly visible is the absorption feature at around 372.4 GHz at 0 T, see Fig. 8.26 (red curve). Increasing the magnetic field with $\mathbf{H}\uparrow\uparrow\mathbf{q}$ (positive fields) shifts the absorption towards higher frequency. No change in the absolute value on the lower frequency side is observed. This agrees with our expectation because for LCP light and $\mathbf{H}\uparrow\uparrow\mathbf{q}$ both features marked in green and yellow in Fig. 8.25 shift towards higher frequency. The inset shows that for inverting the magnetic field, $\mathbf{H}\downarrow\downarrow\mathbf{q}$, the higher frequency side remains unchanged whereas the absorption shifts towards lower frequency. The partially wavelike appearance of the absorption in \tilde{T}

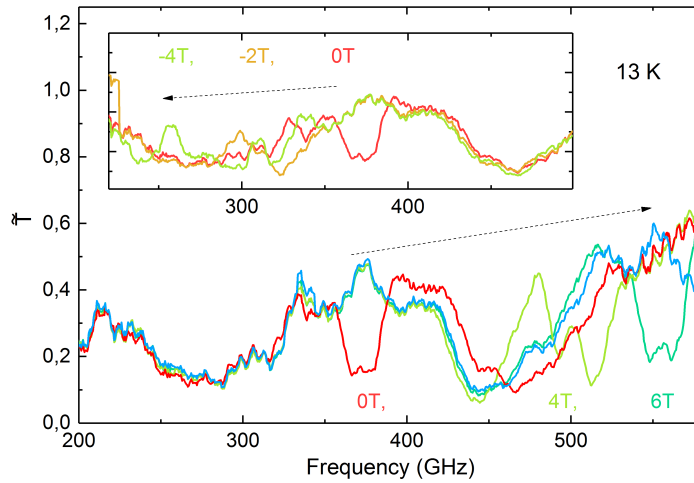


Figure 8.26: Data for $\mathbf{H}\uparrow\mathbf{q}$ of \tilde{T} for the multidomain sample measured with LCP light showing the field dependent shift in frequency of the lower electromagnon. Data for $\mathbf{H}\downarrow\mathbf{q}$ is presented in the inset.

can be explained because the presence of the electromagnons at certain frequencies changes the refractive index in both domains and therefore the optical thickness. In a frequency range where, without the excitations, the relative optical thickness led to a dominantly destructive interference around 280 GHz or 420 GHz, a change in the relative optical thickness due to presence of the excitations, e.g. for 4 T (green), can lead to constructive interference and therefore a higher transmittance. The second electromagnon at 1058.8 GHz, which was not observable in the magnetic cryostat while measuring the single-domain sample, can also be seen in \tilde{T} for the multidomain sample, see Fig. 8.27. Here, again for LCP light the absorption shifts towards higher frequency. Inverting the field direction leads to a shift towards lower frequencies for increasing magnetic field. This was expected since the second excitation in zero magnetic field was much stronger measured with RCP light in the R domain, which is same as measuring the L domain with LCP light, see Sec. 5.1.1. For the single-domain sample, the data of ΔL gave a bigger insight into the field dependence of the excitation. In this particular case it is a problem because the phase of the light passing through both domains is changed individually but measured simultaneously. Therefore no clear excitations as in the single-domain measurements can be seen. In the following the field dependent frequency for the two electromagnon modes can be collected combining the information of phase and transmission data. In Fig. 8.28, the positions gained using the multidomain sample are blue and black. The points in cyan are the field dependent positions measured only on the L domain, see Sec. 8.4.1, included here for comparison. Points around 3 T or -2 T are difficult to obtain due to the increasing

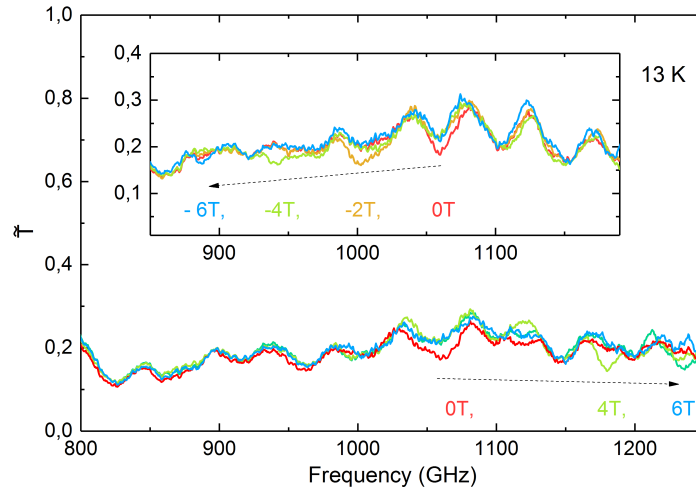


Figure 8.27: Data for $\mathbf{H}\uparrow\uparrow\mathbf{q}$ of \tilde{T} for the multidomain sample measured with LCP light showing the field dependent shift in frequency of the upper electromagnon. Data for $\mathbf{H}\downarrow\downarrow\mathbf{q}$ is presented in the inset.

transmittance caused by interference around 460 GHz and 280 GHz and therefore left out. The single-domain does not have that problem wherefore the cyan data fits in the gap. Linear fits yield slopes of 30.58 GHz/T on the single-domain sample and 30.96 GHz/T for the multidomain sample in case of the lower mode. This gives a g factor between 2.19 and 2.21. For the upper mode, 29.24 GHz/T yields a g factor of 2.09, what is significantly lower.

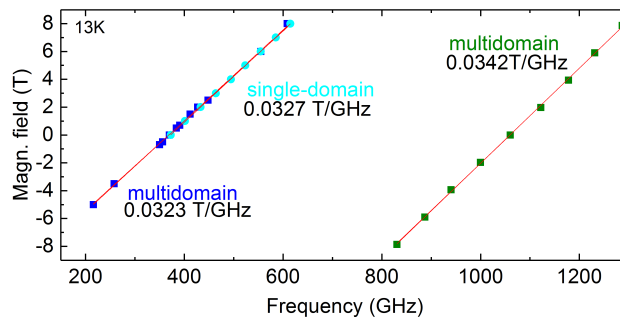


Figure 8.28: Magnetic field dependence of the frequency of the electromagnons measured with LCP light.

8.4.3 Unpolarized light

Knowing that both electromagnons experience a frequency shift in magnetic fields while measured with circularly polarized light and show a different strength in the response to both helicities in zero field as well as in finite field leads to the conclusion that unpolarized light shows a difference in the absorption in finite magnetic fields has to be expected depending on whether the propagation direction and the magnetic field direction are parallel or antiparallel. In the most easiest picture this can be understood by looking at Fig. 8.19 and summing magenta and green curves for $\mathbf{H}\uparrow\uparrow\mathbf{q}$ and compare that to the sum of blue and yellow curves for $\mathbf{H}\downarrow\uparrow\mathbf{q}$. To quantify this effect, similar to Sec. 8.4.1.2, we assume that the parameters found at zero magnetic field do not change for small magnetic fields. Since unpolarized light consists of equally LCP and RCP light with all possible phases, we can simply add the contribution of κ_+ and κ_- for $\mathbf{H}\uparrow\uparrow\mathbf{q}$ (red) and $\mathbf{H}\downarrow\uparrow\mathbf{q}$ (black). The curves show that a large difference has to be expected. For the other domain, colors red and black have to be exchanged. In our setup, we do not have the possibility to measure with unpolarized light. Fortunately, Istvan Kézsmárki and David Szaller, measured data on the same sample with unpolarized light. This data, presented in Fig. 8.30, was measured with a THz time domain spectrometer on the multidomain sample. Data shows the relative absorption with respect to 60 K in the paramagnetic phase for magnetic fields parallel (red) and antiparallel (black) to \mathbf{q} . The only reason why a difference between the red and the black data can be seen in the multidomain sample is because the size of the domains is different. For a crystal consisting of the same proportion of the first and the second domain, all four colors mix for $\mathbf{H}\uparrow\uparrow\mathbf{q}$ and $\mathbf{H}\downarrow\uparrow\mathbf{q}$, respectively, compare Fig. 8.25. The effect of the two domains would compensate each other. Since one domain is

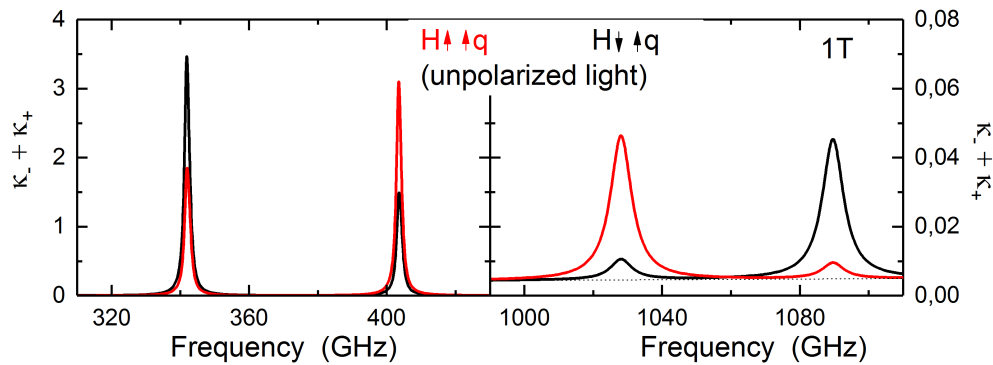


Figure 8.29: Difference in the transmission for unpolarized light upon inverting the magnetic field direction \mathbf{H} for a fixed propagation direction, or the propagation direction for an fixed magnetic field direction \mathbf{H} , for the single-domain sample and a magnetic field strength of 1 T.

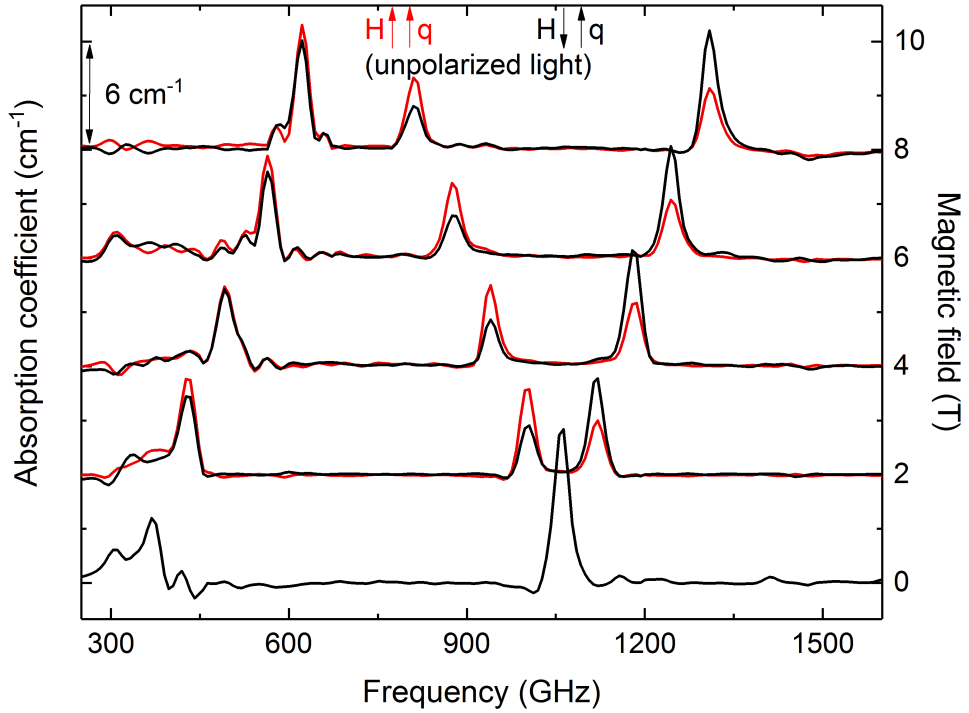


Figure 8.30: Measurement with unpolarized light on the multidomain sample performed by David Szaller. Absorption normalized with data measured at 60 K, shifted with respect to applied magnetic field (right axis). Data measured for two different configurations $\mathbf{H}\downarrow\uparrow\mathbf{q}$ (black) and $\mathbf{H}\uparrow\uparrow\mathbf{q}$ (red).

smaller, the absorption of one domain compared to the other domain is reduced, leading to a finite difference when measuring both domains simultaneously. But the reason that there is a finite difference is caused by the different absorption for unpolarized light in each of the two domains independently, as shown in Fig. 8.29. Since the single-domain measured within this thesis is larger, the effective difference in this domain dominates also the effect in the multidomain sample, Fig. 8.25, therefore the qualitative agreement for the simulation at one domain and the measured data on the multidomain sample can be seen. Additionally the higher frequency resolution of our cw spectrometer helps measuring the difference for the relatively narrow electromagnon at 372.4 GHz in zero magnetic field.

9 Conclusion

The difference in the transmittance for unpolarized light upon passing through the sample in opposite directions is a fascinating phenomenon. But it is not the final answer to the question what actually happens but more the starting point for detailed investigations of the reasons for such an effect.

This work reports on measurements on a relatively small sample of Ni_3TeO_6 . A large influence of diffraction on the transmittance prohibits a sole investigation there, but the phase is almost not affected. A combination of informations about relative changes in the transmittance and accurate absolute values based on analysis of the phase data leads to the best possible results.

In the beginning we focus on the exact determination of the contributions from the setup on the measured phase. We collect contributions coming from the optical fibers, the photomixers and antennae as well as the terahertz path to develop a model description of the measured phase. This model describes the frequency dependence of the phase for a single data set very accurately. In a normal measurement consisting of sample and reference, these contributions will cancel. Still, understanding the proportions in $\Delta\varphi_{mod}$ helps estimating their influence on the error of the phase. The drift ∂L of the optical path-length difference ΔL is found to be the most problematic in our setup.

Therefore a detailed investigation on the phase drift caused by a drift of the path-length is presented for different measurement conditions. This is accompanied with the presentation of a method using a fixed THz frequency as a reference for recording this drift. The recorded drift can be used to correct simultaneously measured THz data. For an optimized setup ($\Delta L \approx 0$, L_{THz} small, ΔT small), the drift is comparably small and an accuracy of $\pm 1 \mu\text{m}$ for ΔL can be achieved. Any deviation from the ideal conditions results in an increasing drift. But still for the most extreme case of a magnetic field sweep measurement in the magnetic field setup, a long term stability of $\pm 5 \mu\text{m}$ can be achieved due to the self-normalization method.

For the investigation of Ni_3TeO_6 , it is highly advantageous to have the possibility of using broadband circularly polarized light. The polarization dependence of the pair of photomixers that is implemented in the setup was investigated. The transmitter emits almost exclusively LCP light and the receiver is similarly almost exclusively sensitive to LCP light. A simple metal plate used as a helicity converter shows that the proportion of light that can be detected with the other polarization

state is less than 2% of the intensity from between 200 GHz and 1200 GHz in the combination of these photomixers. Using a linear polarizer before the sample and a helicity converter behind the sample gives access to the information contained in the part of the linearly polarized light that interacted with the sample as RCP light.

The effect of the diffraction at a sample is shortly discussed. The combination of the above mentioned abilities gives us the experimental opportunity to investigate Ni_3TeO_6 . In zero magnetic field at 3 K, two features were found at 372.4 GHz and 1058.8 GHz, which show a clear difference when excited with LCP or RCP light. This difference is caused by the presence of χ^{me} that leads to a term that describes natural circular dichroism in the sample, see Sec. 5.2. Therefore those excitations are electromagnons. Phenomenologically it is not yet clear why the electromagnons pick up chirality of the crystal, especially because the material has a simple antiferromagnetic collinear spin structure at low temperature.

The natural circular dichroism leads to a rotation in the polarization plane of linearly polarized light which is up to 200° for a ≈ 1 mm thick sample close to 372.4 GHz. However, due to the high absorption close to that frequency, the maximum value that could be observed is $\approx 100^\circ$. The temperature dependence shows a broadening and softening up to $T_N = 53$ K for the lower mode while the upper mode is not observable for temperatures of 25 K or higher. Additionally, an almost linear decrease of χ_{xx}^{me} can be observed when fitting the two modes simultaneously. This is also reflected in the temperature dependence of the real and imaginary part of the refractive index, Δn and $\Delta \kappa$ are largest at the lowest temperature and they almost vanish at 40 K.

Using the magnetic field setup, the magnetic field dependence is investigated with LCP light. Both electromagnons show clear Zeeman splitting. The analysis shows that the strength of the lower mode changes in magnetic field but the dominant factor for small magnetic field is the already in zero field existing difference between the strength of the LCP and the RCP response. Therefore we conclude that directional dichroism occurs in Ni_3TeO_6 . Based on our model, we can quantify the effect for small magnetic fields.

The presence of directional dichroism is also confirmed by a measurement with unpolarized light performed by collaboration partners. But at this point rather than the end, this is more the beginning of a new story. The finding that for larger magnetic fields the change in the mode is comparatively strong implies that there is more at work than pure Zeeman splitting. A detailed analysis with a different sample, if possible the other domain type, might help to disentangle further effects such as magneto chiral dichroism or magnetic circular dichroism if they are present in the material.

Bibliography

- [1] D. Szaller, S. Bordács, V. Kocsis, T. Rőöm, U. Nagel, and I. Kézsmárki. Effect of spin excitations with simultaneous magnetic- and electric-dipole character on the static magnetoelectric properties of multiferroic materials. *Phys. Rev. B*, 89:184419, 2014.
- [2] S.-W. Cheong, D. Talbayev, V. Kiryukhin, and A. Saxena. Broken symmetries, non-reciprocity, and multiferroicity. *npj Quantum Materials*, 3:19, 04 2018. doi: 10.1038/s41535-018-0092-5.
- [3] X. Wang, F.-T. Huang, J. Yang, Y. S. Oh, and S.-W. Cheong. Interlocked chiral/polar domain walls and large optical rotation in Ni_3TeO_3 . *APL Materials*, 3(076105), 2015.
- [4] Y. S. Oh, S. Artyukhin, J. J. Yang, V. Zapf, J. W. Kim, D. Vanderbilt, and S.-W. Cheong. Non-hysteretic colossal magnetoelectricity in a collinear antiferromagnet. *Nature Communications*, 5:3201 EP, 2014.
- [5] A.J. Deninger, T. Göbel, D. Schönherr, T. Kinder, A. Roggenbuck, M. Köberle, F. Lison, T. Müller-Wirts, and P. Meissner. Precisely tunable continuous-wave terahertz source with interferometric frequency control. *Rev. Sci. Instr.*, 79(044702), 2008.
- [6] S. Mickan, J. Xu, J. Munch, X.-C Zhang, and D. Abbott. The limit of spectral resolution in THz time-domain spectroscopy. *Proceedings of SPIE - The International Society for Optical Engineering*, 2004.
- [7] M. Baillergeau, K. Maussang, T. Nirrengarten, J. Palomo, L. H. Li, E. H. Linfield, A. G. Davies, S. Dhillon, J. Tignon, and J. Mangeney. Diffraction-limited ultrabroadband terahertz spectroscopy. *Scientific Reports*, 6:24811 EP, 2016.
- [8] A. J. Deninger, A. Roggenbuck, S. Schindler, and S. Preu. 2.75 THz tuning with a triple-DFB laser system at 1550 nm and InGaAs photomixers. *Journal of Infrared, Millimeter, and Terahertz Waves*, 36(3):269–277, 2015.
- [9] S. Kraft et al. Rubidium spectroscopy at 778-780 nm with a distributed feedback laser diode. *Laser Phys. Lett.*, 10.1002:1–6, 2004.

- [10] *Boosta Semiconductor Laser Amplifier*. Toptica Photonics AG, m-003 version 03 edition.
- [11] I. C. Mayorga. *Photomixers as tunable terahertz local oscillators*. PhD thesis, Universität Bonn, 2008.
- [12] A. Roggenbuck, K. Thirunavukkuarasu, H. Schmitz, J. Marx, A. Deninger, I. C. Mayorga, R. Güsten, J. Hemberger, and M. Grüninger. Using a fiber stretcher as a fast phase modulator in a continuous wave terahertz spectrometer. *J. Opt. Soc. Am. B*, 29(4):614–620, 2012.
- [13] J. Marx. Design and implementation of a liquid helium cryostat for continuous-wave THz spectroscopy. Master thesis, 2011.
- [14] A. Janssen. Implementation of a THz spectrometer into low temperatures and high magnetic fields, 2010.
- [15] M. Langenbach. Analysis of antenna performance for THz spectroscopy at low temperatures and in high magnetic field, 2011. Diploma thesis.
- [16] H. Schmitz. Optimization of a continuous-wave THz spectrometer for coherent broadband solid-state spectroscopy, 2012. PhD thesis.
- [17] Ernesto Vidal. Eliminating phase drift in a continuous wave THz spectrometer using three lasers, 2011.
- [18] A. Schmitz P. van der Wal I. C. Mayorga, E. A. Michael and R. Güsten. Terahertz photomixing in high energy oxygen- and nitrogen-ion-implanted GaAs. *Appl. Phys. Lett.*, 91:031107:1–3, 2007.
- [19] M. McFadden. Analysis of the equiangular spiral antenna, 2009.
- [20] Y. Hirota, R. Hattori, M. Tani, and M. Hangyo. Polarization modulation of terahertz electromagnetic radiation by four-contact photoconductive antenna. *Opt. Express*, 14(10):4486–4493, 2006.
- [21] N. Yogesh, T. Fu, F. Lan, and Z. Ouyang. Far-infrared circular polarization and polarization filtering based on fermat’s spiral chiral metamaterial. *IEEE Photonics Journal*, 7(3):1–12, 2015. ISSN 1943-0655.
- [22] H. Wang, N. Li, Y. Bai, P. Liu, Z. Wang, and C. Liu. Generation of largely elliptically polarized terahertz radiation from laser-induced plasma. *Opt. Express*, 25(25):30987–30995, Dec 2017.
- [23] J. Shan, J. I. Dadap, and T. F. Heinz. Circularly polarized light in the single-cycle limit: the nature of highly polychromatic radiation of defined polarization. *Opt. Express*, 17(9):7431–7439, 2009.

-
- [24] I. S. Gregory, C. Baker, W. R. Tribe, I. V. Bradley, M. J. Evans, E. H. Linfield, A. G. Davies, and M. Missous. Optimization of photomixers and antennas for continuous-wave terahertz emission. *IEEE Journal of Quantum Electronics*, 41(5):717–728, 2005.
- [25] S. Tsuzuki, C. Que, T. Furuya, and M. TANI. Circular polarization property of a spiral photoconductive antenna in THz frequency region. 10 2018.
- [26] P. Schumacher. Polarisations-eigenschaften von Photomischern in der Breitband-terahertz-Spektroskopie, 2013. Bachelor Thesis.
- [27] M. Dressel, O. Klein, S. Donovan, and G. Grüner. High frequency resonant techniques for studying the complex electrodynamic response in solids. *Ferroelectrics*, 176(1):285–308, 1996.
- [28] Coherent broadband continuous-wave terahertz spectroscopy on solid-state samples. 2010.
- [29] M. Langenbach, A. Roggenbuck, I. Cámara Mayorga, A. Deninger, K. Thirunavukkuarasu, J. Hemberger, and M. Grüninger. Group delay in THz spectroscopy with ultra-wideband log-spiral antennae. *J Infrared Milli Terahz Waves*, 35:918–931, 2014.
- [30] I.C. Malitson. Interspecimen comparison of the refractive index of fused silica. *J. Opt. Soc. Amer.*, 55:1205, 1965.
- [31] T. K. Nguyen, Thi H. A., H. Haewook, and I. Park. Numerical study of self-complementary antenna characteristics on substrate lenses at terahertz frequency. *Journal of infrared, millimeter and terahertz waves*, 33, 2012.
- [32] W. Wiesbeck, G. Adamiuk, and C. Sturm. Basic properties and design principles of UWB antennas. *Proceedings of the IEEE*, 97(372), 2009.
- [33] M. McFadden and Jr W.R. Scott. Analysis of the equiangular spiral antenna on a dielectric substrate. *IEEE Trans. Antennas Propag.*, 55(3163), 2007.
- [34] M. McFadden and Jr W.R. Scott. The equiangular spiral antenna at low frequencies. *Microwave Opt. Techn. Lett.*, 51(536), 2009.
- [35] T.W. Hertel and G.S. Smith. On the dispersive properties of the conical spiral antenna and its use for pulsed radiation. *IEEE Trans. Antennas Propag.*, 51(1426), 2004.
- [36] Artem V. Boriskin, Alexander I. Nosich, Svetlana V. Boriskina, Trevor M. Benson, Phillip Sewell, and Ayhan Altintas. Lens or resonator? Electromagnetic behavior of an extended hemielliptical lens for a receiver. *Microwave Opt. Techn. Lett.*, 43(515), 2004.

- [37] T. Göbel. *Systeme, Verfahren und Komponenten zur hochauflösenden Dauerstrich Terahertz-Spektroskopie*. PhD thesis, TU Darmstadt, 2010.
- [38] H.M. Pickett, R.L. Poynter, E.A. Cohen, M.L. Delitsky, J.C. Pearson, and H.S.P. Müller. Submillimeter, millimeter, and microwave spectral line catalog. *Journal of Quantitative Spectroscopy and Radiative Transfer*, 60(5):883 – 890, 1998.
- [39] D. Grischkowsky, Y. Yang, and M. Mandehgar. Zero-frequency refractivity of water vapor, comparison of debye and van-vleck weisskopf theory. *Opt. Express*, 21(16):18899–18908, 2013.
- [40] J.A. Kaiser. The archimedian two wire spiral antenna. *IRE Trans. Antennas Propag.*, 8(312), 1960.
- [41] P. Piksa and M. Mazanek. Active region and higher-order modes of spiral antennas. In *2012 6th European Conference on Antennas and Propagation (EUCAP)*, pages 1960–1962, 2012.
- [42] M. Scheller and M. Koch. Terahertz quasi time domain spectroscopy. *Opt. Express*, 17(17723), 2009.
- [43] A. Roggenbuck, M. Langenbach, K. Thirunavukkuarasu, H. Schmitz, A. Deninger, I. C. Mayorga, R. Güsten, J. Hemberger, and M. Grüninger. Enhancing the stability of a continuous-wave terahertz system by photocurrent normalization. *J. Opt. Soc. Am. B*, 30(1397), 2013.
- [44] K. Thirunavukkuarasu, M. Langenbach, A. Roggenbuck, E. Vidal, H. Schmitz, J. Hemberger, and M. Grüninger. Self-normalizing phase measurement in multimode terahertz spectroscopy based on photomixing of three lasers. *Appl. Phys. Lett.*, 106(031111), 2015.
- [45] M. Medhat, S. Y. El-Zaiat, A. Radi, and M F Omar. Application of fringes of equal chromatic order for investigation of the effect on optical parameters of a GRIN optical fiber. *J. Opt. A: Pure Appl. Opt.*, 4:174–179, 2002.
- [46] J. Komma, C. Schwarz, G. Hofmann, D. Hinert, and R. Nawrodt. Thermo-optic coefficient of silicon at 1550 nm and in cryogenic temperatures. *Appl. Phys. Lett.*, 101(041905), 2012.
- [47] B. Douglas, B. Leviton, and J. Frey. Temperature-dependent absolute refractive index measurements of fused silica. *e-print arXiv:0805.0091v1.*, 2008.
- [48] S.A. Crooker et al. Fiber-coupled antennas for ultrafast coherent terahertz spectroscopy in low temperatures and high magnetic fields. *Rev. of Sci. Instr.*, 73:3258–3264, 2002.
- [49] J. B. Pendry. A chiral route to negative refraction. *Science*, 306(1353), 2004.

-
- [50] S. Tredjakov, I. Nefedov, A. Sihvola, S. Maslovski, and C. Simovski. Waves and energy in chiral nihility. *J. Electromagn. Waves, Appl.* 17(695), 2003.
- [51] C. Monzon. Negative refraction and focusing of circularly polarized waves in optically active media. *Phys. Rev. Lett.*, 95(123904), 2005.
- [52] S.S. Oh and O. Hess. Chiral metamaterials: enhancement and control of optical activity and circular dichroism. *Nano Convergence*, 2(24), 2015.
- [53] S. Zhang, Y.-S. Park, J. Li, X. Lu, W. Zhang, and X. Zhang. Negative refractive index in chiral metamaterials. *Phys. Rev. Lett.*, 102(023901), 2009.
- [54] A. Pimenov and A. Loidl. Negative refraction in ferromagnet-superconductor superlattices. *Phys. Rev. Lett.*, 98(197401), 2005.
- [55] A. Pimenov, A. Loidl, K. Gehrke, V. Moshnyaga, and X. Zhang. Negative refraction observed in a metallic ferromagnet in the gigahertz frequency range. *Phys. Rev. Lett.*, 98(197401), 2007.
- [56] Y. Tokura and N. Nagaosa. Nonreciprocal responses from non-centrosymmetric quantum materials. *Nature Communications*, 9(1):3740, 2018. ISSN 2041-1723.
- [57] D. Szaller, S. Bordács, and I. Kézsmárki. Symmetry conditions for nonreciprocal light propagation in magnetic crystals. *Phys. Rev. B*, 87:014421, 2013.
- [58] G. L. J. A. Rikken and E. Raupach. Observation of magneto-chiral dichroism. *Nature*, 390:493 EP, 1997.
- [59] S. Bordács. *Exotic magneto-optical effects in solids*. Phd thesis, 2011.
- [60] I. Kézsmárki, D. Szaller, S. Bordács, V. Kocsis, Y. Tokunaga, Y. Taguchi, H. Murakawa, Y. Tokura, H. Engelkamp, T. Rõm, and U. Nagel. One-way transparency of four-coloured spin-wave excitations in multiferroic materials. *Nature Communications*, 5:3203 EP, 2014.
- [61] A.M. Glazer and K.G. Cox. *International Tables for Crystallography*, volume D. 2006.
- [62] R.E. Newnham and E.P. Meagher. Crystal structure of Ni_2TeO_6 . *Materials Research Bulletin*, 2(5):549 – 554, 1967.
- [63] J. W. Kim, S. Artyukhin, E. D. Mun, M. Jaime, N. Harrison, A. Hansen, J. J. Yang, Y. S. Oh, D. Vanderbilt, V. S. Zapf, and S.-W. Cheong. Successive magnetic-field-induced transitions and colossal magnetoelectric effect in Ni_3TeO_6 . *Phys. Rev. Lett.*, 115:137201, 2015.

- [64] S. Bordács, I. Kézsmárki, D. Szaller, L. Demkó, N. Kida, H. Murakawa, Y. Onose, R. Shimano, T. Rõm, U. Nagel, S. Miyahara, N. Furukawa, and Y. Tokura. Chirality of matter shows up via spin excitations. *Nature Physics*, 8:734 EP, 2012.
- [65] J. Lekner. Optical properties of isotropic chiral media. *Pure and Applied Optics: Journal of the European Optical Society Part A*, 5(4):417, 1996.
- [66] J. Zupan, D. Kolar, and V. Urbanc. Magnetic properties of Ni_3TeO_6 . *Materials Research Bulletin*, 6(12):1353 – 1359, 1971. ISSN 0025-5408.
- [67] G. Blasse and W. Hordijk. The vibrational spectrum of Ni_3TeO_6 and Mg_3TeO_6 . *Journal of Solid State Chemistry*, 5(3):395 – 397, 1972. ISSN 0022-4596.
- [68] R. Becker and H. Berger. Reinvestigation of Ni_3TeO_6 . *Acta Crystallographica Section E*, 62(11):i222–i223, 2006.
- [69] R. Sankar, G. J. Shu, B. Karunakara Moorthy, R. Jayavel, and F. C. Chou. Growing of fixed orientation plane of single crystal using the flux growth technique and ferrimagnetic ordering in Ni_3TeO_6 of stacked 2d honeycomb rings. *Dalton Trans.*, 42:10439–10443, 2013. doi: 10.1039/C3DT50785H.
- [70] S. A. Ivanov, R. Mathieu, P. Nordblad, R. Tellgren, C. Ritter, E. Politova, G. Kaleva, A. Mosunov, S. Stefanovich, and M. Weil. Spin and dipole ordering in $\text{Ni}_2\text{InSbO}_6$ and $\text{Ni}_2\text{ScSbO}_6$ with corundum-related structure. *Chemistry of Materials*, 25(6):935–945, 2013. ISSN 0897-4756.
- [71] M. O. Yokosuk, A. al Wahish, S. Artyukhin, K. R. O’Neal, D. Mazumdar, P. Chen, J. Yang, Y. S. Oh, Stephen A. McGill, K. Haule, S.-W. Cheong, D. Vanderbilt, and J. L. Musfeldt. Magnetoelectric coupling through the spin flop transition in Ni_3TeO_6 . *Phys. Rev. Lett.*, 117:147402, 2016. doi: 10.1103/PhysRevLett.117.147402.
- [72] I. Živković, K. Prša, O. Zaharko, and H. Berger. Ni_3TeO_6 a collinear antiferromagnet with ferromagnetic honeycomb planes. *Journal of Physics: Condensed Matter*, 22(5):056002, 2010.
- [73] S. Skiadopoulou, F. Borodavka, C. Kadlec, F. Kadlec, M. Retuerto, Z. Deng, M. Greenblatt, and S. Kamba. Magnetoelectric excitations in multiferroic Ni_3TeO_6 . *Phys. Rev. B*, 95:184435, 2017.
- [74] Y. S. Chai, S. Kwon, S. H. Chun, I. Kim, B.-G. Jeon, K. H. Kim, and S. Lee. Electrical control of large magnetization reversal in a helimagnet. *Nature Communications*, 5:4208 EP, 2014.

- [75] N. Engheta, D. L. Jaggard, and M. W. Kowarz. Electromagnetic waves in faraday chiral media. *IEEE Transactions on Antennas and Propagation*, 40(4):367–374, 1992. ISSN 0018-926X.
- [76] José Ramón Galán-Mascarós. Bring to light. *Nature Physics*, 11:7 EP, Dec 2014.
- [77] S. Miyahara and N. Furukawa. Theory of magneto-optical effects in helical multiferroic materials via toroidal magnon excitation. *Phys. Rev. B*, 89:195145, 2014.
- [78] M. Retuerto, S. Skiadopoulou, F. Borodavka, C. Kadlec, F. Kadlec, J. Prokleška, Z. Deng, J. A. Alonso, M. T. Fernandez-Diaz, F. O. Saouma, J. I. Jang, D. Legut, S. Kamba, and M. Greenblatt. Structural and spectroscopic properties of the polar antiferromagnet $\text{Ni}_2\text{MnTeO}_6$. *Phys. Rev. B*, 97:144418, 2018.
- [79] Mathieu, R., Ivanov, S. A., Nordblad, P., and Weil, M. Enhancement of antiferromagnetic interaction and transition temperature in M_3TeO_6 systems ($m = \text{mn, co, ni, cu}$). *Eur. Phys. J. B*, 86(8):361, 2013.
- [80] Inc. Lake Shore Cryotronics. *8500 Series THz System for Material Characterization*. 2016.
- [81] E. Hecht and A. Zajac. *Optics*. 1974.

List of Figures

1.1	Main components of the cw THz spectrometer. The superimposed signal of two DFB lasers is amplified and split into two equal parts and guided to the two photomixers used as transmitter and receiver. Two fiber stretcher modulate the path-length to the transmitter (L_{Tx}) and the receiver (L_{Rx}). Sample is placed in the optical path with length (L_{THz}) between the two photomixers.	6
1.2	Magnetic-field setup inside the magneto-cryostat. Optical fibers guide the laser light to the photomixers used as transmitter and receiver inside the cryostat, directly at low temperature and in high magnetic field. Sample and reference aperture can be interchanged at any temperature or field using a piezo-rotator. For details of the compact face-to-face assembly, see Fig. 1.3.	7
1.3	Compact face-to-face assembly in cryo-magnet. Sample is placed at the center on a piezo-rotator that allows interchanging sample and empty reference aperture. The THz signal, created and detected by transmitter (P_A) and receiver (P_B) directly at low T and high B . Two wire grid polarizers (pol.1 and pol.2) can be inserted if necessary.	8
2.1	Left circular polarized light (green) from the source is converted to light with equal amounts of left- and right-handedness (grey) by a linear polarizer. The detector 2 is only sensitive to the left-handed part. Inserting a mirror directs the beam to detector 2'. Upon reflection, light changes chirality. Detector 2' measures again only the LCP light, which interacted with the sample as RCP light	12
2.2	Conversion of left-handed circularly polarized light, split by a linear polarizer into \mathbf{E}_{LCP} (green) and \mathbf{E}_{RCP} (magenta) light, into \mathbf{E}_{RCP}' light and \mathbf{E}_{LCP}' light upon reflection from at metal plate.	13
2.3	Top: THz amplitude of the LCP (green) and RCP (magenta) part of linear polarized light measured using the geometry described in Fig. 2.1. Bottom: Ratio of LCP to RCP THz amplitude (black, points) averaged over 50 GHz (red, solid) to overcome contributions caused by standing waves in two different THz paths.	14

2.4	Top: ΔL of the left-handed (green) and right-handed (magenta) part of linear polarized light measured using the geometry described in Fig. 2.1. Bottom: Difference between left- and right-handed ΔL (red, solid) and difference between two successive measurements of ΔL with right-handed light (black, circle).	15
2.5	Intensity of the non-prioritized polarization direction compared to the total intensity hitting the detector (black, dots) averaged over 50 GHz (red, solid). Spectrum shown from 100 GHz to 1300 GHz. . .	16
3.1	Different data sets of $\Delta\varphi(\nu)$ (blue) measured in face-to-face configuration. L_{THz} (≈ 22 cm) was changed to obtain different values of ΔL . Frequency step width was 1 GHz except for $\Delta L \approx -0.06$ mm where 100 MHz was chosen. Calculated values of $\Delta\varphi_{mod}(\nu)$ (red) fitted using Eq. 3.6 with parameters $\Delta\phi_{an}(\nu_{max}) = 0.27\pi$ and ΔL as can be seen in the plot. The comparison between data and model yields $m \cdot 2\pi = 8\pi$	20
3.2	Nonlinear contributions of measured phase data and model. $\Delta\varphi(\nu) - \Delta L_0 \cdot 2\pi\nu/c$ for the data set with $\Delta L \approx -0.06$ mm (blue) and the modeled $\Delta\varphi_{an}$ (red dashed) and $\Delta\varphi_{RC}$ (red dotted). Both modeled contributions add up to $\Delta\varphi_{mod} - \Delta L_0 \cdot 2\pi\nu/c$ (red solid). Same data on a logarithmic frequency scale is shown in the inset	23
3.3	Effective optical path-length difference ΔL_{eff} for the data set with $\Delta L_0 \approx 0.03$ mm, cf. Eq. 3.7. <i>Inset</i> shows 4.07 GHz and 0.7 GHz modulation on the same data in the range of 650 GHz to 677 GHz. Modulations stem from Si lenses of the photomixers as well as standing waves in the optical path L_{THz} between the two lenses. Data measured with 0.1 MHz step size.	24
3.4	Fourier series $E(t)$ of the data (<i>black</i>) measured up to 1.8 THz for $\Delta L \approx -0.06$ mm (data from Fig. (3.3)) and after correction (<i>red</i>). Data are offset for clarity. Scale changes at 10 cm. Measurement with frequency step width of 100 MHz yields a period of $T \approx 300$ cm. <i>Inset</i> shows corrected data on a different scale. Feature shifted by 7.36 cm with respect to the main peak is caused by standing waves in the Si lenses, the peak at 43.1 cm corresponds to $2 \cdot L_{THz}$ and results from standing waves between the two photomixers.	26
3.5	Top panel: Phase difference $\delta\varphi(\nu)$ for $\Delta L \approx -0.06$ mm as shown in Fig. 3.1 measured with 100 MHz as frequency step size. Middle panel: Group delay difference Δt_{gr} compared to the contributions of the photomixer impedance (green) and the antenna (black). The blue curve gives a rough estimate of the envelope. Bottom panel: same data but multiplied by $(c/\nu)\partial\nu$ with $\partial\nu = 5$ MHz for comparison with a change ∂L of the length.	28

4.1	Three different laser frequencies ν_1 , ν_2 (both fixed), and ν_3 (fixed or tunable) result in three difference frequencies ν_{ref} , ν_{31} , and ν_{32} in the THz range.	32
4.2	Solid lines: Three constant THz frequencies ν_i record the temporal drift $\partial L(t)$ of the optical path-length difference. Symbols: corrected values for $\partial L_{31}(t) - \partial L_{ref}(t)$ (red) and $\partial L_{32}(t) - \partial L_{ref}(t)$ (blue), shifted for better visibility.	33
4.3	Phase drift $\partial\varphi(t)$ recorded for three constant THz frequencies ν_i over three hours. Data taken with bad thermal contact between the two fiberstretchers. Upper panel: corrected values $\nu_i - \nu_{ref}$ $t_0 = 0$ min (symbols). Lower panel: corrected values $t_0 = 60$ min (symbols), shows an offset induced by the correction.	34
4.4	Corrected ΔL_{eff} in μm , averaged over 10 runs from 400 GHz to 600 GHz (top panel). Standard deviation in μm before (black solid points) and after (red open circles) correction (middle panel). Drift ∂L in μm for fixed reference frequency $\nu_{ref} = 327$ GHz over 15 hours (bottom panel).	35
4.5	Corrected ΔL_{eff} in μm , averaged over 11 runs from 500 GHz to 750 GHz (top panel). Standard deviation in μm before (black circles) and after (red circles) correction (middle panel). Drift ∂L in μm for fixed reference frequency $\nu_{ref} = 400$ GHz over 30 minutes (bottom panel).	36
4.6	ΔL_{eff} in μm recorded at three fixed THz frequencies $\nu_{12} = 710$ GHz (black), $\nu_{31} = 511$ GHz (blue) and $\nu_{32} = 199$ GHz (red) for a magnetic field up and down sweep from 8 T and -8 T (top panel). Drift corrected ΔL_{eff} for 199 GHz and 511 GHz (bottom panel).	37
4.7	Corrected ΔL_{eff} in μm recorded for sample (green) and reference (blue) measurement at 511 GHz for a magnetic field up and down sweep from 0 T to 8 T, -8 T, and back to 0 T. 60 mT averaged deviation between corrected sample and reference measurement shifted by $-25 \mu\text{m}$ (black)	38
5.1	Switching on chirality. A non-chiral sample has the same response (grey) independent of direction and polarization. Decomposed into the two chiral enantiomers L and R, a difference in the refractive index for LCP and RCP light can be seen.	43
5.2	Schematic overview on configurations for measuring with RCP and LCP waves traveling along positive (\mathbf{q}) and negative ($-\mathbf{q}$) x direction. A chiral medium (R , L) without external field, see 1). Magneto-optical response such as for instance the Faraday effect for magnetic field \mathbf{H} applied in positive and negative x direction, see 2). Chiral medium in external field, see 3).	44

5.3	Connection between different configurations of helicity of light (RCP or LCP) and propagation direction ($\pm\mathbf{q}$), positive and negative magnetic field direction ($\pm\mathbf{H}$), and both enantiomers R and L via inversion and time-reversal symmetry.	45
5.4	Sketch of the chiral medium in finite magnetic field with two different absorption strengths for RCP and LCP light already at zero magnetic field for L and R enantiomer.	46
6.1	(a) Crystal structure of Ni_3TeO_6 in ball-and-stick and polyhedra views showing stacked NiO_6 octahedra with $\text{Ni}_{(i)}$ in blue, $\text{Ni}_{(ii)}$ in yellow, $\text{Ni}_{(iii)}$ in green, and Ti in black, (b) $\text{Ni}_{(i)}\text{O}_6$ - $\text{Ni}_{(ii)}\text{O}_6$ and $\text{Ni}_{(iii)}\text{O}_6$ - TeO_6 honeycomb layers are stacked following $R3$ symmetry. The red balls correspond to O ions, the honeycomb layer is built from the Ni ions at the center of the drawn octahedra. Figure and caption from Sankar <i>et al.</i> [69].	53
6.2	A basic building block of Ni_3TeO_6 is shown in (a) which corresponds to 1/3 of the unit cell. The red triangle is associated with unequal bond lengths which can be considered as part of the first $\text{Ni}_{(iii)}\text{O}_6$ - TeO_6 honeycomb layer. Then, the neighboring $\text{Ni}_{(i)}\text{O}_6$ - $\text{Ni}_{(ii)}\text{O}_6$ layer is associated with the blue triangle with unequal bond lengths. The shortest bonds are marked as bold lines. (b) shows two different ferri-chiral states: left panel with net left-handed chirality and right panel with net right-handed chirality. Red and blue helices, shown by the rotation of the bold red and blue bonds, respectively, rotate in an opposite fashion, and a net chirality exists due to the asymmetry of the red and blue triangles (helices). Figure and caption modified from [3].	54
6.3	Phase diagram of Ni_3TeO_6 determined by variations in the dielectric constant ϵ (color scale at upper right) and magnetoelectric current. Closed circles, closed squares, and open asterisks indicate peak-center positions for $\epsilon(T)$, $\epsilon(H)$, and magnetoelectric current $J(H)$, respectively. These peaks map the boundaries between the paramagnetic (PM) phase and antiferromagnetic phases (AFM I, AFM II). The structure of Ni_3TeO_6 is of the corundum type with a polar $R3$ space group, three inequivalent $S=1$ Ni sites, and significant distortions of oxygen octahedra surrounding Ni ions. The spin configurations in the AFMI and AFMII phases are shown schematically in the insets. Figure and caption modified from [71].	55

-
- 6.4 Temperature dependence of (a) real and (b) imaginary part of index of refraction, as obtained by THz measurements at $H^{DC} \perp E_{THz}$ for the Ni_3TeO_6 ceramics. Two excitations appear below 48 K, close to $T_N \approx 53$ K. Upon application of H^{DC} up to 7 T, softening of the lowest frequency mode is observed. For comparison with our results on a single crystal, see Fig. 8.14 and Fig. 8.15. (c) Temperature evolution of the $z(xy)\bar{z}$ Raman spectra of the Ni_3TeO_6 single crystal below 45 K. Figure and caption partly from [73]. 57
- 6.5 Pictures of Ni_3TeO_6 sample from a Leitz Ortholux-Pol microscope (a,b), a modified Leitz microscope (c,d,f), and a Keyence VHX 6000 microscope (e,h). a) shows the radiation-sign-like domain structure from the top side while b) shows the best possible extinction of the other domains from the bottom side. c) The experimental coverage of one domain type and a red circle with 0.21 mm radius in the center (top side). d) The remaining visible crystal with the polarization microscope (top side). Illumination from above was switched off for better contrast. f) Uncovered bottom side with a red circle with 1 mm radius. Note that, due to different microscopes and different amplifications, the size is not exactly the same through the different series. For size reference, use c), d), and f) only. 58
- 7.1 Normalized intensity vs. frequency for different aperture sizes integrated on a virtual screen 5 cm behind the aperture in an area with radius of $r=10$ cm. Pictures are from [81], showing Airy rings for an 1 mm and an 0.5 mm aperture. 62
- 7.2 Data measured at 13 K in an optical cryostat (green) and the magnetic field setup (black). Transmittance $\tilde{T}(\omega)$ multiplied by a factor of 3 on a linear scale (top panel), and a log scale (middle panel) without multiplication factor and the corresponding $\Delta L(\omega)$ (bottom panel). Fit to $\Delta L(\omega)$ and the corresponding Kramers-Kronig consistent transmittance $T(\omega)$ without diffraction (red). 63
- 8.1 The transmittance \tilde{T} with RCP (LCP) light at 60 K, purple (dark green), and 3 K, magenta (light green). At 3 K, strong features appear at 372.4 GHz and 1058.8 GHz when measuring with RCP and LCP light. Frequency step size equals 1 GHz for RCP and 0.5 GHz for LCP light. The periodic oscillations correspond to Fabry-Perot interference fringes. 68
- 8.2 Path-length difference $\Delta L_{RCP} = (\tilde{n}_{RCP} - 1)d$ (magenta) and $\Delta L_{LCP} = (\tilde{n}_{LCP} - 1)d$ (light green) at 3 K. Data show a large difference between the two polarizations (and therefore n_+ and n_-) around 372.4 GHz. Inset shows a smaller difference around 1058.8 GHz. Frequency step size equals 1 GHz for RCP and 0.5 GHz for LCP light. 69

8.3	Transmittance (upper panel) and ΔL (lower panel) at 3 K measured with LCP (light green) and RCP (magenta) light. Frequency range is from 350 GHz to 390 GHz with a frequency step-size of 50 MHz. Transmittance shows a clear difference in the absorption between RCP and LCP light before reaching the noise level between 10^{-4} and 10^{-5} . Center position is estimated from the average position at different absorption levels wherefore spectra were smoothed over 250 MHz. ΔL shows a much stronger response in LCP light than in RCP light.	70
8.4	3D plot at T= 3 K showing the normalized intensity distribution in the frequency range between 359 GHz and 382 GHz upon rotating the analyzer with respect to the polarizer. The plane of polarization of the incoming linearly polarized light is rotated by the sample by more than $\approx 100^\circ$ close to the absorption center at 372.4 GHz. Frequency step width is 0.5 GHz and relative rotation of the analyzer is 5° between two spectra. In the frequency range between 371 GHz and 374.5 GHz, the angle is set to zero.	71
8.5	Rotation angle Θ of the plane of polarization for linearly polarized light in the frequency range from 200 GHz to 1090 GHz at T= 3 K. Close to the two excitations, $ \Theta $ increases up to 100° around 372.4 GHz and 16° around 1058.8 GHz. Features at ≈ 850 GHz are visible at all temperatures up to room temperature and are assigned to geometrical problems due to the sample shape, see Fig. 6.5 c).	72
8.6	Chirality factor γ at T= 3 K as a function of frequency calculated from ΔL (blue) and Θ (red), respectively. Both data sets show a very similar frequency dependence around 372.4 GHz and 1058.8 GHz (inset).	73
8.7	Panel 1: Overall spectrum of ΔL_{RCP} (magenta) and ΔL_{LCP} (light green), offset for better visibility, with fit (black for LCP and cyan for RCP). Panel 2 shows frequency range between 350 GHz and 390 GHz for ΔL in the upper part and T in the lower part. The measured \tilde{T} is rescaled by a frequency independent factor of $1/0.0117$ to show the qualitative agreement with T . Panel 3 shows the same graphs in the frequency range between 980 GHz and 1080 GHz, using a rescaling factor of $1/0.37$ for \tilde{T}	75
8.8	Real part n_+ (magenta) and n_- (light green) of the refractive index extracted from the fit in the frequency range between 200 GHz and 1090 GHz. Insets show range between 1020 GHz and 1080 GHz. The model shows a finite difference $\Delta n_{model} = n_+ - n_-$ (red) which is in good agreement with the measured difference $\Delta \tilde{n}_{data} = (\Delta L_{RCP} - \Delta L_{LCP})/d$ (black).	77

8.9	Imaginary part κ_+ (magenta) and κ_- (light green) of the refractive index extracted from the fit in the frequency range between 360 GHz and 380 GHz on the left hand side. Difference $\Delta\kappa_{model} = \kappa_+ - \kappa_-$ (red) on the right hand side. Insets show range from 1030 GHz and 1080 GHz	78
8.10	Left: T calculated from fit to ΔL for LCP (black) and RCP (cyan) for a 1.05 mm thick sample. Right: T at 1058.8 GHz as a function of thickness in the model. Minimum transmission read out for LCP (black) and RCP (cyan). Ratio T_{RCP}/T_{LCP} in red.	78
8.11	Measured (red) and calculated (cyan) rotation angle of the plane of polarization for linearly polarized light. The calculated data result from the fit of ΔL_{LCP} and ΔL_{RCP} , see Fig. 8.7. Inset shows range between 320 GHz and 480 GHz. Data is measured with different frequency step sizes in between 400 GHz and 900 GHz, compare Fig. 8.5.	79
8.12	Top panel: Temperature dependence of ΔL_{LCP} measured with frequency step size of 0.5 GHz. Bottom panel: ΔL_{RCP} measured with frequency step size of 1 GHz. Insets show frequency ranges from 280 GHz to 390 GHz and 900 GHz to 1080 GHz, respectively.	80
8.13	Rotation angle Θ for different temperatures between 220 GHz and 600 GHz. The maximum value of Θ decreases for increasing temperature. Inset shows data between 900 GHz and 1090 GHz.	81
8.14	Real part n_+ (solid) and n_- (dashed) of the refractive index extracted from the fit in the frequency range between 200 GHz and 400 GHz. The model shows the difference $\Delta n_{model} = n_+ - n_-$. Inset shows the frequency range between 240 GHz and 330 GHz.	82
8.15	Imaginary part κ_+ (solid) and κ_- (dashed) of the refractive index extracted from the fit in the frequency range between 260 GHz and 380 GHz for different temperatures on the left hand side. Difference $\Delta\kappa_{model} = \kappa_+ - \kappa_-$ on the right hand side. Insets show range from 1030 GHz and 1080 GHz.	82
8.16	Eigenfrequency ω_0 (top left), width γ (top right), ω_p and ω_m (bottom left), and ω_{xx} (bottom right) as function of temperature. For definition of parameters, see Eqns. 8.5-8.8. The dots represent frequency positions from measurements within this thesis, whereas the crosses represent data measured from David Szaller at Vienna University of Technology on the same sample using unpolarized and linearly polarized light.	83
8.17	THz amplitude with crossed polarizers for 3 K (red) and 60 K (cyan). Data are averaged over 4 frequency sweeps with a step size of 0.5 GHz and smoothed over 2.5 GHz.	84

8.18	\tilde{T} (top left) and ΔL (bottom left) measured with parallel (red) and crossed polarizers (black) at 3 K. T (top right) and ΔL (bottom right) calculated from the result of the fit of ΔL_{LCP} and ΔL_{RCP} at 3 K, compare Fig. 8.7.	85
8.19	Sketch of the frequency dependence of the absorption when applying magnetic field, compare Fig. 5.4. This figure contains the simplification that the absorption features strengths does not change in magnetic field.	86
8.20	$\tilde{T}(\omega)$ for different magnetic field strengths and $\mathbf{H}\uparrow\uparrow\mathbf{q}$ (green) or $\mathbf{H}\downarrow\uparrow\mathbf{q}$ (blue) at 13.5 K. The latter data are shifted for better visibility. Grey arrows indicate the direction of the field-dependent frequency shift of the lower electromagnon at 372.4 GHz (dashed vertical line).	87
8.21	Magnetic field dependence of $\Delta L_{LCP}(\omega)$ for fields $\mathbf{H}\downarrow\uparrow\mathbf{q}$ (blue) or $\mathbf{H}\uparrow\uparrow\mathbf{q}$ (green) in the frequency range between 300 GHz and 1100 GHz at 13.5 K. The blue data is shifted by 0.1 cm for better visibility. Grey arrows indicate the direction of the field dependent frequency shift of the electromagnon at 372.4 GHz in zero magnetic field. . . .	88
8.22	Fit (red) of $\Delta L_{LCP}(\omega)$ (green) for different magnetic fields between 0 T and 8 T. ω_P , ω_m , and ω_{xy} are set as constant whereas ω_{xx} , γ , and ω_0 are used as fit parameters at 13.5 K.	89
8.23	Frequency position $\omega_0 + \omega(B)$ measured with LCP light (filled symbols) and the corresponding position expected for RCP (open symbols) (top left), width γ (top right), ω_p and ω_m (bottom left), and ω_{xx} as well as ω_{xy} (bottom right) as function of magnetic field at 13.5 K.	89
8.24	Magnetic field dependence of $\Delta n = n_+ - n_-$ (top panel) and $\Delta\kappa = \kappa_+ - \kappa_-$ (middle panel) for small magnetic fields below 0.5 T at 3 K. Resulting Θ in the bottom panel.	90
8.25	Sketch of the frequency dependence of the absorption features when applying magnetic field, compare Fig. 5.2. Left side corresponds the domain discussed in Fig. 8.19. Right side corresponds to the second domain. This figure contains the simplification that the absorption strength does not change in magnetic field.	92
8.26	Data for $\mathbf{H}\uparrow\uparrow\mathbf{q}$ of \tilde{T} for the multidomain sample measured with LCP light showing the field dependent shift in frequency of the lower electromagnon. Data for $\mathbf{H}\downarrow\downarrow\mathbf{q}$ is presented in the inset.	93
8.27	Data for $\mathbf{H}\uparrow\uparrow\mathbf{q}$ of \tilde{T} for the multidomain sample measured with LCP light showing the field dependent shift in frequency of the upper electromagnon. Data for $\mathbf{H}\downarrow\downarrow\mathbf{q}$ is presented in the inset.	94
8.28	Magnetic field dependence of the frequency of the electromagnons measured with LCP light.	94

8.29	Difference in the transmission for unpolarized light upon inverting the magnetic field direction \mathbf{H} for a fixed propagation direction, or the propagation direction for an fixed magnetic field direction \mathbf{H} , for the single-domain sample and a magnetic field strength of 1 T.	95
8.30	Measurement with unpolarized light on the multidomain sample performed by David Szaller. Absorption normalized with data measured at 60 K, shifted with respect to applied magnetic field (right axis). Data measured for two different configurations $\mathbf{H}\downarrow\uparrow\mathbf{q}$ (black) and $\mathbf{H}\uparrow\uparrow\mathbf{q}$ (red).	96
10.1	Simultaneous fit to $\Delta L_{LCP}(\omega)$ (top panel) and $\Delta L_{RCP}(\omega)$ (middle panel). From the result of the fit, measured $\Theta(\omega)$ at 13 K can be reproduced.	119
10.2	Simultaneous fit to $\Delta L_{LCP}(\omega)$ (top panel) and $\Delta L_{RCP}(\omega)$ (middle panel) 40 K. From the result of the fit, measured $\Theta(\omega)$ at 25 K can be reproduced.	120
10.3	Simultaneous fit to $\Delta L_{LCP}(\omega)$ (top panel) and $\Delta L_{RCP}(\omega)$ (middle panel). Result shows almost no difference between n_- and n_+ and therefore no increase in $\Theta(\omega)$	120
10.4	Simultaneous fit to $\Delta L_{LCP}(\omega)$ (top panel) and $\Delta L_{RCP}(\omega)$ (middle panel) at 60 K. Result shows almost no difference between n_- and n_+ and therefore no increase in $\Theta(\omega)$	121

List of Tables

5.1	Probing configurations for a chiral material in magnetic field	45
8.1	Fit parameters for 3 K. All parameters which are fixed during the fit are marked as <i>fixed</i> . Thickness is 0.1050 cm, ϵ_∞ is 8.51 and a phase offset φ_0 is fixed at -0.2. EM1 and EM2 denote to the electromagnons at 372.4 GHz and 1058.8 GHz.	76

10 Appendix

10.1 Results for fits to ΔL_{LCP} and ΔL_{RCP} for different temperatures

In the following, the corresponding fits to Sec. 8.2 are presented.

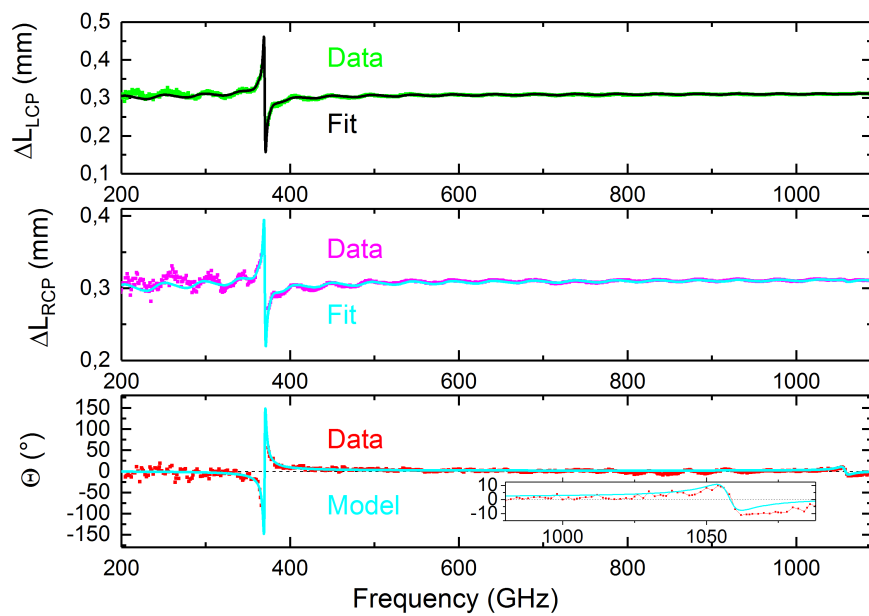


Figure 10.1: Simultaneous fit to $\Delta L_{LCP}(\omega)$ (top panel) and $\Delta L_{RCP}(\omega)$ (middle panel). From the result of the fit, measured $\Theta(\omega)$ at 13 K can be reproduced.

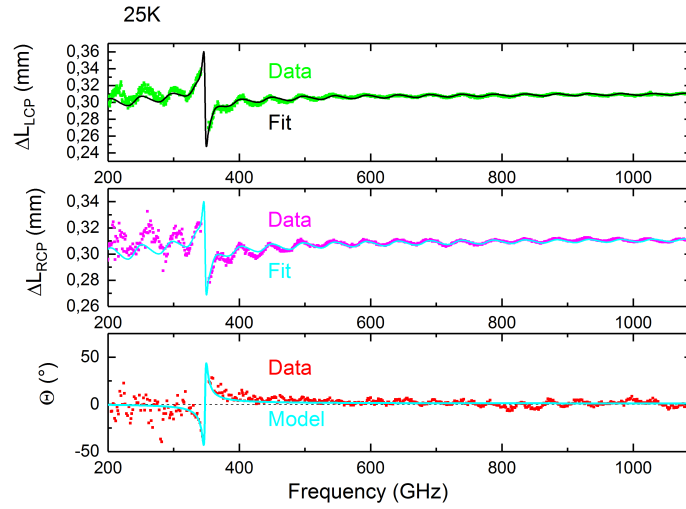


Figure 10.2: Simultaneous fit to $\Delta L_{LCP}(\omega)$ (top panel) and $\Delta L_{RCP}(\omega)$ (middle panel) 40 K. From the result of the fit, measured $\Theta(\omega)$ at 25 K can be reproduced.

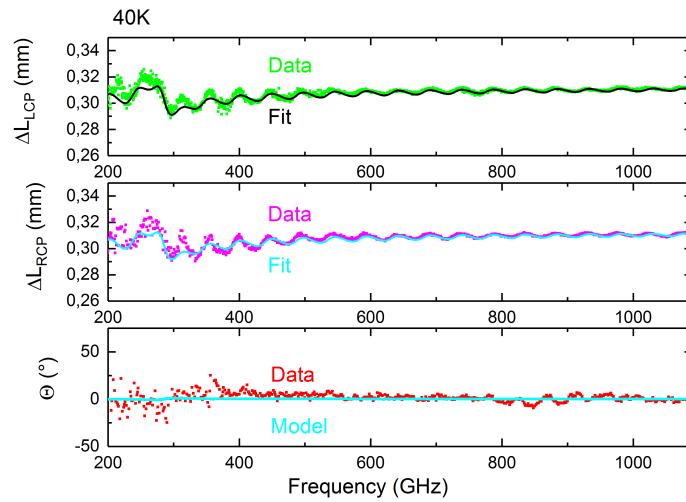


Figure 10.3: Simultaneous fit to $\Delta L_{LCP}(\omega)$ (top panel) and $\Delta L_{RCP}(\omega)$ (middle panel). Result shows almost no difference between n_- and n_+ and therefore no increase in $\Theta(\omega)$.

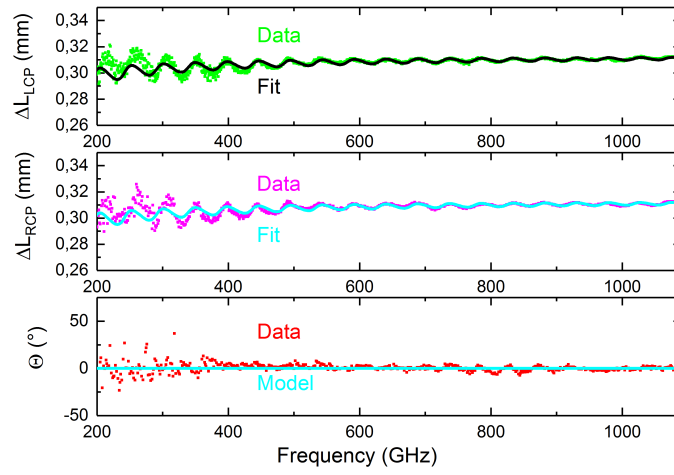


Figure 10.4: Simultaneous fit to $\Delta L_{LCP}(\omega)$ (top panel) and $\Delta L_{RCP}(\omega)$ (middle panel) at 60 K. Result shows almost no difference between n_- and n_+ and therefore no increase in $\Theta(\omega)$.

11 Publications

- **Group Delay in THz Spectroscopy with Ultra-Wideband Log-Spiral Antennae**
M. Langenbach, A. Roggenbuck, I. Cámara Mayorga, K. Thirunavukkuarasu, A. Deninger, J. Hemberger, and M. Grüninger
J Infrared Milli Terahz Waves 35: 918. (2014)
- **Self-normalizing phase measurement in multimode terahertz spectroscopy based on photomixing of three lasers**
K. Thirunavukkuarasu, M. Langenbach, A. Roggenbuck, E. Vidal, H. Schmitz, J. Hemberger, and M. Grüninger
Applied Physics Letters 106:3 031111 (2015)
- **Enhancing the stability of a continuous-wave terahertz system by photocurrent normalization**
A. Roggenbuck, M. Langenbach, K. Thirunavukkuarasu, H. Schmitz, A. Deninger, I. Cámara Mayorga, R. Güsten, J. Hemberger, and M. Grüninger
J. Opt. Soc. Am. B 30, 1397-1401 (2013)
- **A fast cw-THz spectrometer using fiber stretchers**
A. Roggenbuck, A. Deninger, K. Thirunavukkuarasu, H. Schmitz, J. Marx, E. Vidal, M. Langenbach, J. Hemberger, and M. Grüninger
Conference on Infrared, Millimeter, and Terahertz Waves, Houston, TX, pp. 1-3. (2011)
- **Broadband continuous-wave THz spectroscopy at low temperature and high magnetic field**
M. Langenbach, K. Thirunavukkuarasu, I. Cámara Mayorga, A. Roggenbuck, A. Deninger, J. Hemberger, and M. Grüninger
Conference: Infrared, Millimeter, and Terahertz Waves , 38th (2013)

12 Abstract

In this thesis, an early prototype of an existing magnetic field setup for a continuous wave THz spectrometer was improved to successfully operate in any conventional magneto cryostat meeting the space requirements for the setup. During the last years, several successful cooling cycles could prove the reliability of the setup. A comparatively simple approach was found, based on the polarization properties of the logspiral antennas, that allow for an investigation of samples with broadband circularly polarized light. A detailed investigation of contributions from the setup to the measured phase did not only quantitatively describe the group delay effect from the photomixers, but also found the length drift ∂L as the main source for drifts in the measured phase. These drifts were investigated concerning their impact on the data quality especially in combination with the magnetic field setup, and the effectiveness of the existing 3 laser setup for the correction of these drifts could be demonstrated 4.

After a discussion of the general appearance of non-reciprocity and quadrichroism based on symmetry, a mathematical approach results in the an expression of the refractive index for the material Ni_3TeO_6 in the absence of an external magnetic field.

An overview of literature on the material Ni_3TeO_6 is followed by a short summarization of the particular sample measured within this thesis. Due to its limited size, a way to circumvent the diffraction problems which usually prevent measuring small samples in the THz regime had to be found. This was done by concentrating on the phase data which is comparably less affected by diffraction than the amplitude data. With the combination of the possibility of measuring a very small sample with circularly polarized light, two excitations 372.4 GHz and 1058 GHz, which were clearly different for measuring with LCP and RCP light already in zero magnetic field, were found using an optical cryostat for measurements at 3 K. This effect is called natural circular dichroism. Since the mathematical description of the refractive index lead to the conclusion that this difference can only be caused by χ^{me} , those features have to be electromagnetically active. The difference in the real part of the refractive index for LCP and RCP light causes a relative rotation of polarization plane of linearly polarized light upon passing through the sample. This effect could be measured as a relative change in the transmittance upon changing the relative angle between two linear polarizers despite the influence of the diffraction on the THz amplitude.

Using a fit based on a model for the transmittance of circularly polarized light and the calculated complex refractive index N_{\pm} , the temperature dependency of real and imaginary part of N_{\pm} could be illustrated. Furthermore the temperature dependence of the different fitting parameters could be extracted. With the magnetic field setup, the magnetic field dependency was investigated. A combination of measurements with a single domain sample and a multidomain sample reveals that both electromagnons at 372.4 GHz and 1058 GHz show a splitting in finite magnetic field. Fitting the data obtained for the single domain sample gives a preliminary description of the fitting parameters also in magnetic fields. In a first approximation for small fields, only adding Zeeman splitting is sufficient to describe the data. With this assumption, simulations based on the model used for the fit show the drastic increase of the rotation for the plane of polarization of linearly polarized light upon passing through the sample with an relatively small external magnetic field. Furthermore the effect of unpolarized light passing through the sample was simulated, revealing a huge difference for opposite propagation directions in finite magnetic fields. This effect was already discovered in measurements performed by collaborators but the underlying reason for this, the difference of the two excitations for LCP and RCP light respectively, already in zero magnetic field in one domain, was only found due to the work within this thesis.

13 Kurzzusammenfassung

Im Rahmen der vorliegenden Arbeit wurde der Prototyp eines Magnetfeldsetups eines cw-THz-Spektrometers weiterentwickelt, so dass er erfolgreich in jedem konventionellen Magnetkryostaten eingesetzt werden kann. Voraussetzung für die Messung mit variablen Magnetfeldern bei tiefen Temperaturen ist lediglich die Erfüllung des Platzbedarfs. Durch zahlreiche erfolgreiche Messungen im Laufe der letzten Jahre konnte die Zuverlässigkeit des Systems in vielen Kühlzirkeln gezeigt werden. Mittels eines vergleichsweise einfachen Ansatzes wird die Messung von Proben mittels breitbandig zirkular polarisiertem Licht ermöglicht. Der Einfluss des Spektrometers auf die gemessene Phase erklärt quantitative die gemessene Gruppenverzögerung, wobei der Drift der Länge ΔL die größte Fehlerquelle ist. Dieser Drift wird bezüglich seines Einflusses, insbesondere in Kombination mit dem Magnetfeldsetup, analysiert und die Effektivität des vorhandenen 3-Laser-Aufbaus für die Korrektur dieses Drifts demonstriert. Nach einer Diskussion des generellen Auftretens von Nicht-Reziprozität und Quadrochromismus basierend auf Symmetrieargumenten, wird ein mathematischer Ausdruck für den komplexen Brechungsindex des Probenmaterials Ni_3TeO_6 hergeleitet. Das Probenmaterial Ni_3TeO_6 wird allgemein vorgestellt und die vermessene Probe genau beschrieben, welche vor allem aufgrund ihrer geringen Größe besondere Anforderungen an die Messung stellt. So musste eine Möglichkeit gefunden werden um Beugungseffekte zu umgehen, welche üblicherweise das Messen einer solch kleinen Probe im THz-Frequenzbereich verhindern. Dies gelingt mittels einer Analyse, welche sich primär auf die gemessene Phase stützt, welche weniger von den Beugungseffekten beeinflusst wird als die gemessene Amplitude. Bei Messungen bei 3 K werden Anregungen bei 372.4 GHz und 1058.8 GHz nachgewiesen, welche sich klar bei Messungen mittels linkszirkular polarisiertem (LCP) und rechtszirkular polarisiertem (RCP) Licht unterscheiden. Dieser Effekt nennt sich Natürlicher Zirkularer Dichroismus. Die mathematische Beschreibung des Brechungsindex legt nahe, dass dieses Verhalten auf dem Vorhandensein von χ^{me} basiert, so dass die Anregungen elektromagnetisch aktiv sein müssen. Der Unterschied im Realteil des Brechungsindex für LCP und RCP Licht verursacht eine Rotation der Polarisationssebene von linear polarisiertem Licht beim Durchqueren der Probe. Dieser Effekt kann in der relativen Änderung der Transmission mittels der relativen Änderung des Winkels zwischen zweier linearer Polarisatoren trotz des Einflusses der Beugung nachgewiesen werden. Durch einen Fit basierend auf einem Modell für die Transmission von

zirkular polarisiertem Licht und dem berechneten komplexen Brechungsindex N , kann die Temperaturabhängigkeit von Real- und Imaginärteil aufgezeigt werden. Zudem wird die Temperaturabhängigkeit der einzelnen Fitparameter dargestellt und mit dem Magnetfeldsetup zusätzlich deren Magnetfeldabhängigkeit untersucht. Das magnetfeldabhängige Aufspalten beider Anregungen kann durch die Kombination von Messungen an einer einzelnen Domäne und simultan an beiden unterschiedlichen Domänen gezeigt werden. Das Anpassen der Daten der einzelnen Domäne ermöglicht eine vorläufige Beschreibung der Magnetfeldabhängigkeit, wobei in erster Näherung, eine Feldabhängige Aufspaltung analog zum Zeeman Effekt reicht um die Daten zu beschreiben. Auf dieser Annahme beruhende Simulationen zeigen, sowohl ein drastisches Ansteigen des Winkels der Rotation der Polarisationssebene von linear polarisiertem Licht beim durchqueren der Probe für kleine Magnetfelder, als auch eine Differenz der Absorption von unpolarisiertem Licht zwischen zwei entgegengesetzten Ausbreitungsrichtungen in endlichem Magnetfeld. Dieser Effekt wurde bereits bei Messungen mit unpolarisiertem Licht beobachtet, allerdings konnte der zugrundeliegende Effekt des Unterschiedes zwischen der Absorption von LCP und RCP Licht schon in einer einzelnen Domäne und ohne angelegtes magnetisches Feld, erst im Rahmen der vorliegenden Arbeit verdeutlicht werden.

Erklärung

Ich versichere, dass ich die von mir vorgelegte Dissertation selbständig angefertigt, die benutzten Quellen und Hilfsmittel vollständig angegeben und die Stellen der Arbeit - einschließlich Tabellen, Karten und Abbildungen -, die anderen Werken im Wortlaut oder dem Sinn nach entnommen sind, in jedem Einzelfall als Entlehnung kenntlich gemacht habe; dass diese Dissertation noch keiner anderen Fakultät oder Universität zur Prüfung vorgelegen hat; dass sie - abgesehen von unten angegebenen Teilpublikationen - noch nicht veröffentlicht worden ist sowie, dass ich eine solche Veröffentlichung vor Abschluss des Promotionsverfahrens nicht vornehmen werde. Die Bestimmungen der Promotionsordnung sind mir bekannt.

Die von mir vorgelegte Dissertation ist von Prof Dr. M. Grüninger betreut worden.

Köln, Dezember, 2018

Malte Langenbach

